TECHNISCHE UNIVERSITÄT ILMENAU

Design and Analysis Approaches to Compact Directional Antennas for Cognitive Radio

Doctoral thesis for attaining the academic degree of Doctor of Engineering (Dr. Ing.)

presented to the Faculty of Electrical Engineering and Information Technology, Ilmenau University of Technology

by M. Sc. Noman Murtaza
(23.08.1981)

Written at: RF and Microwave Research Laboratory
Institute of Information Technology
Faculty of Electrical Engineering and Information Technology

Submitted on: 23.12.2013

Reviewed by: 1. Prof. Dr. rer. nat. habil. M. A. Hein
Ilmenau University of Technology

2. Prof. Dr.-Ing. habil. Reiner Thomä
Ilmenau University of Technology

3. Prof. Cyril Luxey
University of Nice Sophia-Antipolis, France

Defended on: 17.10.2014

urn:nbn:de:gbv:ilm1-2014000548

ACKNOWLEDGEMENTS

The presented work has been performed during my stay at the Ilmenau University of Technology as a member of the Graduate School on Mobile Communication (MobicoM). I worked as a research fellow in the RF and Microwave Research Laboratory at the Institute of Information Technology, Ilmenau University of Technology.

First of all, I would like to thank Prof. Matthias A. Hein for his guidance and encouragement that shaped up this thesis to its present form. I would also like to thank Michael Grimm, Alexander Krah, Anastasia Lavrenko, Christopher Schirmer, and Dr. Rajesh K. Sharma for their untiring support; Dr. Ralf Stephan and Safwat Irteza, for the fruitful discussions; Christian Schneider and Martin Käske for their help in understanding and implementing the channel models and measurements; Michael Huhn and Matthias Zocher for their technical support.

The colleagues at the department and within MobicoM created a comfortable work environment, for which I am grateful to all. Thanks to all students, whose work in the form of research projects and Master theses, made a contribution to this thesis. I am also grateful for the opportunity to work with state-of-the-art measurement equipment within RF and Microwave Research Lab.

This work was funded by the German Research Foundation, in the framework of the MobiCom Research Training Group (GRK 1487). I would like to thank Prof. Andreas Mitschele Thiel and Dr. Mirko Kirschkowski for their support, as head and administrative manager of MobicoM.

Finally, my very special thanks go to my wife, Sana, for her unfailing support, and for taking care of our children when I was not around.

ABSTRACT

Cognitive radio is an emerging radio technology, promising intelligent and effective use of spectrum resources. State-of-the-art measurement campaigns show that the allocated spectrum is not efficiently used by the licensed users. On the other hand, future radio technologies need more spectrum to meet high capacity and quality of service requirements. Cognitive radio proposes secondary usage of the under-utilised spectrum resources while preserving the access rights of the licensed (primary) users.

Since the introduction of cognitive radio, in 1999, the focus of cognitive radio communications has been on frequency resources. However, frequency resource alone may not be sufficient to fulfil the needs of future communication systems. A combination of frequency, space/direction, and time can ensure a more efficient use of the spectrum, by employing techniques like direction-of-arrival estimation, interference mitigation, etcetera. Approaches to design and analyse compact multi-band directional antennas, required to support directional as well as frequency resources, are proposed in this thesis. Design of such antennas was accomplished with orthogonal arrangement of multi-band antennas, and with compact multi-band antenna arrays. Analysis of directional antennas was carried out with simulations, measurement campaigns, and emulation of channel sounder measurements.

A concentric arrangement of monopole antenna arrays was used as a reference antenna system, where directional patterns were obtained using metallic/absorber walls between antenna elements. This reference antenna system was used to perform proof-of-principle measurement campaigns. With an antenna array of nine elements, nine degrees-of-freedom (frequency-directional resources) were obtained at the antenna ports. These consist of three selectable frequency bands, namely GSM 900 MHz, GSM 1800 MHz, and IEEE 802.11b/g, and three directions per frequency band. The reference antenna system was capable of separating frequency and directions with a signal-to-interference-ratio of 20 dB, inside an anechoic chamber. An outdoor measurement of such an antenna system was carried out for GSM 1800 MHz, at a location surrounded by four base-stations. Power detection was used as the spectrum sensing algorithm. The opportunity to commu-

nicate in a certain direction using the occupied frequency channels was observed for about 50 % of the sensing time for various GSM channels.
This concentric arrangement was made compact by reducing the inter-element spacing. The reduction of inter-element spacing results in mutual coupling between the antenna elements, which disturbs the current distribution and hence the beam patterns of the antenna arrays. To reduce this negative effect, a multi-band decoupling and matching network was designed to mitigate the element coupling and to match the elements with mode-specific loads. Reconfigurable networks were designed with the help of the capacitive tuning of varactor diodes. The multi-band decoupling and matching network, and the reconfigurable network for GSM 900 MHz were manufactured on a printed circuit board, and tested in terms of decoupling, matching, and resulting port beam patterns. The 10 dB bandwidth for matching and decoupling by the fixed network, for compact antenna arrangement with an inter-element spacing of $\lambda/6$, was about 30 MHz. Reconfigurable network provided a bandwidth above 100 MHz, achievable with five reconfigurable states. The patterns were orthogonal in different directions with correlation coefficients less than 30 % and self-similar at different frequency bands with a correlation better than 70 %.
Finally, the behaviour of directional antennas under heterogeneous propagation scenarios was studied using simulation and emulation. This involved channel models for statistical simulation of static scenarios, and existing channel sounder measurements for emulation of mobility scenarios. Various measured and analytical beam patterns were used to study the availability of directional communications resources for cognitive radio. Simulations with analytical patterns of uniform circular arrays indicated that the received signal strength is directly proportional to the side-lobe level of the directional patterns. A side-lobe level of 20 dB, achievable with an array of 6 elements, was found to be optimum. The opportunity to communicate in certain directions using the occupied frequency channels (directional opportunity) was obtained for 50% of the total snapshots for a threshold level lower than -120 dBm, in mobility scenarios.
It is concluded that well-designed directional antennas can identify the existence of directional resources for cognitive radio communications. Exploitation of unexplored antenna strategies for cognitive radio empowers a cognitive node with significant additional degrees-of-freedom. However, angular distribution of multipath, mobility of primary or secondary user, and speed of detection influence the usability of directional resources for cognitive radio. Decoupling and matching networks for compact arrays can be fabricated with off-the-shelf lumped elements with tight tolerances. Such networks can be made reconfigurable using varactor diodes. The work presented in the thesis is expected to facilitate the design of future directional antennas for cognitive radios resulting in more efficient utilisation of the spectrum.

ZUSAMMENFASSUNG

Cognitive radio (CR) ist eine neuartige Technologie, die es erlaubt die spektralen Funkressourcen intelligent und effektiv zu nutzen. Jüngste Messkampagnen beweisen, dass die zugewiesenen Frequenzbänder der lizenzierenden Benutzer nicht effizient genutzt werden. Außerdem benötigen moderne Funktechnologien mehr Spektrum, um wachsenden Datenübertragungsrate- und Quality-of-Service-Anforderungen gerecht zu werden. Cognitive radio erlaubt die Sekundärnutzung von nicht vollständig genutzten Frequenzbereichen, wobei die Primärnutzung durch Lizenzinhaber nicht gestört werden darf.
Seit der ersten Erwähnung von Cognitive radio im Jahr 1999 lag der Fokus auf Frequenz- bzw. spektralen Ressourcen. Allerdings ist dies für die Anforderungen von zukunftsweisenden Funktechnologien nicht ausreichend. Eine Kombination aus der Betrachtung von Frequenz, Raum/Richtung und Zeit ermöglicht eine noch effizientere Nutzung des Funkspektrums. Dabei kommen Technologien wie beispielsweise die Schätzung der Empfangsrichtung und die Interferenzunterdrückung zum Einsatz. In dieser Arbeit werden Methoden des Entwurfs und der Analyse von direktiven Multibandantennen zur Bereitstellung richtungs- und frequenzabhängiger Funktionalitäten vorgestellt. Dies geschieht mit Hilfe orthogonal angeordneter Multibandantennen und mit kompakten Multibandantennenarrays. Die entworfenen Antennen wurden mit Hilfe von Simulationen, Messungen und durch die Emulation von channel-sounder-Messungen analysiert.
Als Referenzantennensystem dient eine konzentrische Anordnung aus Monopolantennenarrays und Absorberplatten zwischen den Antennenelementen. Dieses Referenzantennensystem wurde für die Durchführung von Machbarkeitsstudien in Messkampagnen eingesetzt. Mit einem aus neun Elementen bestehenden Array können entsprechend neun Freiheitsgrade erzielt werden. Diese setzen sich aus drei wählbaren Frequenzbändern (GSM 900 MHz, GSM 1800 MHz, und IEEE 802.11b/g) und drei Richtungen pro Frequenzband zusammen. Das Referenzantennensystem ist in der Lage, Frequenzbänder und Signaleinfallsrichtungen mit einem Signal-zu-Interferenz-Verhältnis von 20 dB unter den reflexionsarmen Bedingungen in einer Absorberkammer aufzulösen. Für das Band des GSM 1800 wurde eine Feldmessung in der Umgebung von vier Basisstationen durchgeführt. Das spektrale Sensing erfolgte nach dem Prinzip der Leistungsdetektion. Mög-

lichkeiten zur richtungsselektiven Kommunikation konnten in einer Vielzahl von GSM-Kanälen für ca. $50\ \%$ der Beobachtungszeit detektiert werden.
Durch die Reduzierung der Zwischenelementabstände konnte eine kompakte Antenne des konzentrischen Antennenarrays konstruiert werden. Dies führt zu einer gegenseitigen Verkopplung der Antennenelemente und damit zu einer Beeinflussung der Stromverteilung und schließlich der Antennenrichtdiagramme. Um diese Effekte zu minimieren, wurde ein multibandfähiges Anpassungs- und Entkopplungsnetzwerk entworfen, welches die Entkopplung und Anpassung der Antennenelemente mit Modenspezifischen Lasten ermöglicht. Die Rekonfigurierbarkeit in jedem Frequenzband wird durch kapazitive Justierung mit Hilfe von Varaktordioden erreicht. Das multibandfähige Anpassungs- und Entkopplungsnetzwerk und das rekonfigurierbare Netzwerk für GSM 900 wurden auf einer Leiterplatte realisiert und im Hinblick auf Entkopplung, Anpassung, und Strahlungsdiagramme der Ports getestet. Die 10 dB-Bandbreite für Anpassung und Entkopplung der statischen Netzwerke ist ca. 30 MHz. Das rekonfigurierbare Netzwerk stellt eine Bandbreite von mehr als 100 MHz bereit, die mit insgesamt 5 Stufen erreicht wird. Die Richtdiagramme waren in verschiedenen Richtungen mit einem Korrelationskoeffizient kleiner als $30\ \%$ orthogonal, und in verschiedenen Frequenzbereichen mit einer Korrelation besser als $70\ \%$ selbstähnlich.
Schließlich wurde das Verhalten von Richtantennen in heterogenen Ausbreitungsszenarien durch Simulation und Emulation untersucht. Dies beinhalteten Kanalmodelle für Simulation von statischen Szenarien und vorhandenen channel-sounder-Messungen zur Emulation der Mobilitätsszenarien. Verschiedene gemessene und analytisch bestimmte Richtdiagramme wurden verwendet, um die Verfügbarkeit von richtungsabhängigen Kommunikationsressourcen für Cognitive radio zu untersuchen. Simulationen mit analytischen Richtdiagrammen von uniform zirkularer Arrays zeigten, dass die Empfangssignalstärke über die Einfallsrichtungen proportional zum Nebenkeulenpegel der direktiven Richtdiagramme ist. Ein Nebenkeulenpegel von 20 dB eines Antennenarrays mit 6 Elementen wurde als Optimum gefunden. Die richtungsabhängigen Sendemöglichkeiten von ca. $50\ \%$ wurden mit einem Sensing-Schwellwert kleiner -120 dBm für mobile Szenarien ermittelt. Die Verfügbarkeit richtungsabhängiger Ressourcen ist abhängig von dem Schwellwert des gewählten Algorithmus für das spektrale Sensing.
Zusammenfassend lässt sich sagen, dass sorgfältig konstruierte direktive Antennen die Existenz richtungsabhängiger Ressourcen für Cognitive radio aufspüren können. Anpassungs- und Entkopplungsnetzwerke für kompakte Antennenarrays können mittels kommerziell verfügbaren konzentrierten Bauelementen mit engen Toleranzen hergestellt werden. Die Rekonfigurierbarkeit solcher Netzwerke kann mittels Varaktordioden erreicht werden. Richtungsabhängige Kommunikation ist mit den vorgeschlagenen Antennen sowohl in statischen als auch mobilen Szenarien möglich.

CONTENTS

LIST OF FIGURES

LIST OF TABLES

1. INTRODUCTION

Cognitive radio (CR) [15, 16] is an emerging technology addressing an intelligent and effective use of otherwise under-utilised spectrum resources. A conventional CR system is governed by the fact that the licensed frequency spectrum is not in use for notable periods of time. This inefficient spectrum occupancy has been demonstrated with measurement campaigns at different geographical locations [50, 51]. Hence, the allocation of licences for frequency spectrum is giving rise to an unnecessary spectrum scarcity. On the other hand, emerging radio technologies require more resources to meet the demands of increasing data rates and quality of service. CR [17] proposes the unlicensed users, termed as secondary users (SU), to use the licensed frequency spectrum when it is not occupied by the licensed user, termed as primary users (PU), such that the activity of PU is not disturbed. Furthermore, the parameter space for CR is conventionally limited to the frequency resource only. Other resources like space, polarisation, etcetera may be considered to extend this parameter space.

Drawing an analogy with human intelligence, a CR antenna can be considered as an electromagnetic equivalent of human ear, eye, etcetera. Like an ear can help in differentiating between sounds, an eye between object location (left/right, near/far), an antenna for CR should be capable of differentiating between different impinging signals. It should be able to resolve the frequency of the signal, its direction-of-arrival, etcetera. This resolution can be achieved at the port of the antenna or after signal processing behind the antenna. Exploitation of unexplored antenna strategies for CR could further empower a cognitive node with significant additional degrees-of-freedom. For example, making use of multiple antennas in the form of antenna arrays can help in direction sensing, and hence in location awareness of primary users. This can subsequently help in avoiding interference to PU using (digital) beamforming while using occupied licensed channels. Situations like heterogeneous path loss conditions between primary and secondary systems [52], relay-assisted transmission of secondary users [18], etcetera may allow spatial re-use of frequency spectrum.

Multiple receive antennas have been proposed for CR to support primary user detection [18, 52], and/or interference suppression [53]. The novelty of the approach presented in this thesis is the potential use of multi-band directional antennas for

sensing as well as for transmission. The utilisation of directional patterns for transmission and reception can, in addition, increase the link budget of the communication system by increasing directivity in certain directions and reducing interference from others.

1.1 Thesis Objectives

Frequency resources have been extensively studied for cognitive radio. Secondary communications opportunity has also been found for the frequency resource. However, directional resource for cognitive radio has not been widely addressed, especially with respect to antenna design. The goal of this thesis is to propose design and analysis approaches to compact directional antennas for cognitive radio. The following research questions are addressed in this thesis:

- Is direction conceivable as a resource for cognitive radio?
- Are directional communications opportunities available in multi-path scenarios?
- What kind of directional antennas are required to exploit directional resources?
- How does a multi-band directional antenna system define frequency and directional resources?
- What is the flexibility versus complexity trade-off for such antennas?
- What is the situation of directional resources in mobility scenarios, and how well the proposed antenna system deals with it?

The availability of directional resources is addressed by carrying out measurement campaigns using a reference antenna system. The antenna was first tested for its capability to separate frequency and directional resources in an anechoic chamber, through an over-the-air measurement. Compact directional antenna designs are proposed to realise multi-band directional antennas with separate frequency and directional access. Feed networks for the compact antenna arrays were fabricated. Reconfigurable feed network designs are proposed for tuning frequency band, while providing undisturbed self-similar (among frequencies) directional patterns.

The existence of directional communications opportunity in static multi-path scenarios is investigated with a measurement based spatial channel model. Flexibility versus complexity trade-off for antenna array is addressed by using analytical array patterns. These patterns are used to identify an optimum directional antenna

array for cognitive radio. The behaviour of realised antenna systems in mobility scenarios is investigated using channel parameters extended from existing channel sounder measurements.

1.2 Research Contributions

Specific approaches to design and analyse compact directional antennas for CR were explored during the course of doctoral research. A preliminary requirement on antenna design for CR is the ability to resonate at multiple frequency bands. In this context, single-port multi-band [43] and multi-port multi-band antennas were studied. Conformal and planar arrangement of these antennas provide access to spatial and frequency resources. Feed strategy for a conformal dipole arrangement was also developed, and a suitable feed network was fabricated.

A concentric arrangement of monopole antenna arrays is proposed as a multi-band direction-selective cognitive antenna system. This antenna system together with a suitable feed network, provides port-level access to all spectral-spatial degrees-of-freedom for CR communications. Compactness was introduced in this concentric array arrangement by reducing the inter-element spacing to $\lambda/6$. The inherent problem of mutual coupling in compact antenna arrays was addressed with the design of a suitable multi-band decoupling and matching network, while preserving the port-level access to spectral-spatial degrees-of-freedom. Reconfigurability was introduced to the feed networks by making use of the variable capacitance of varactor diodes [44].

A laboratory version of the concentric monopole arrays with $\lambda/2$ inter-element spacing, capable of providing three directional patterns at three frequency bands associated with selectable standards like GSM 900 MHz, GSM 1800 MHz and IEEE 802.11b/g 2450 MHz, was used as a reference multi-band directional antenna system. The capability of this reference antenna system to differentiate between direction-of-arrival and frequency of incoming signals was studied with a proof-of-principle measurement campaign in an over-the-air line-of-sight scenario, inside an anechoic chamber [45, 46]. An outdoor measurement campaign was then performed with the reference antenna system to evaluate the existence of directional communications resource in a static multipath scenario.

The behaviour of directional antennas under heterogeneous propagation scenarios was studied using simulations and emulations. These involved ray tracer based simulations [47], spatial channel models for simulation of static scenarios, and channel measurements for emulation of mobility scenarios. The goal of these analyses was to study the availability of directional communications resources using various measured and analytical directional patterns. Simulations were performed with analytical patterns of uniform circular arrays to study the influence of the

side-lobe level, and the number of array elements on the availability of the directional communications opportunity [48]. These simulations made use of a spatial channel model, extracted from multiple measurement campaigns, to generate the power angular profile of the multipath channel. The measured directional patterns were embedded to channel parameters extracted from channel sounder measurements, in order to emulate the mobility of CR node in a multipath scenario.

The proposed design and analysis approaches are aimed at facilitating future antenna designs for CR. The target is to achieve more efficient spectrum utilisation, catering the future high capacity and quality-of-service requirements. The proposed work is expected to trigger more research into exploring the directional aspects in CR antenna designs.

1.3 Thesis Outline

The thesis starts with the theoretical background in chapter 2. Chapter 3 describes basic considerations followed by proof-of-principle measurement campaigns performed by using a reference antenna system. Design of various multi-band antennas, and antenna arrays are proposed in chapter 4. Measurement results of the realised antenna systems are presented in chapter 5. The performance of the designed antenna systems is evaluated for mobility scenarios in chapter 6. The thesis concludes with a summary at the end.

2. THEORETICAL BACKGROUND

This chapter presents theoretical overview on selected topics in the field of cognitive radio and antenna design. This overview describes the state-of-the-art, and introduces the background necessary to understand the following discussions. The chapter starts with the definition and basic principles of cognitive radio in section 2.1. The commonly used spectrum sensing algorithm, energy detection, is described, and the state-of-the-art antennas for cognitive radio are summarised. The basics of antennas and antenna arrays are presented in section 2.2. The concept of compact antenna arrays and the decoupling and matching network are presented. The chapter concludes with a brief description of the evaluation methodologies that can be considered in order to analyse directional antennas for cognitive radio.

2.1 Cognitive Radio

Cognitive radio (CR) is an emerging radio technology that promises to overcome the problem of spectrum scarcity. Spectrum is a scarce resource in the context that most of the usable spectrum is already allocated to various radio communications services. On the other hand, emerging radio technologies need more spectrum to meet high data rate and quality of service requirements. Since the allocated spectrum is not efficiently consumed [50, 51], there is a possibility to allow secondary usage of this spectrum while preserving the ownership of licensed users. The spectrum can be used when licensed users are inactive, and evacuated as soon as the licensed users appear [15, 16]. In state-of-the-art, this free spectrum is referred to as a *hole* or *white space*, the licensed user as *primary user* (PU), and the CR user as *secondary user* (SU).

Since the idea of CR has been proposed by Mitola in his doctoral thesis [9] in 1999, a lot of scientific contributions have been made in this direction. In the past few years, various communications as well as regulatory aspects for CR have been in focus by various non-profit organisations like WInnForum [1], DySPAN [2], and COST IC 1004 work-group 3 [3]. The goal of all these organisations is to ad-

[1] Wireless Communication Forum (former SDR Forum). http://www.wirelessinnovation.org
[2] IEEE Dynamic spectrum Access Networks. http://dyspan2014.ieeedyspan. org/
[3] COST IC 1004 work group 3. http://www.ic1004.org/index.php?page=wg3

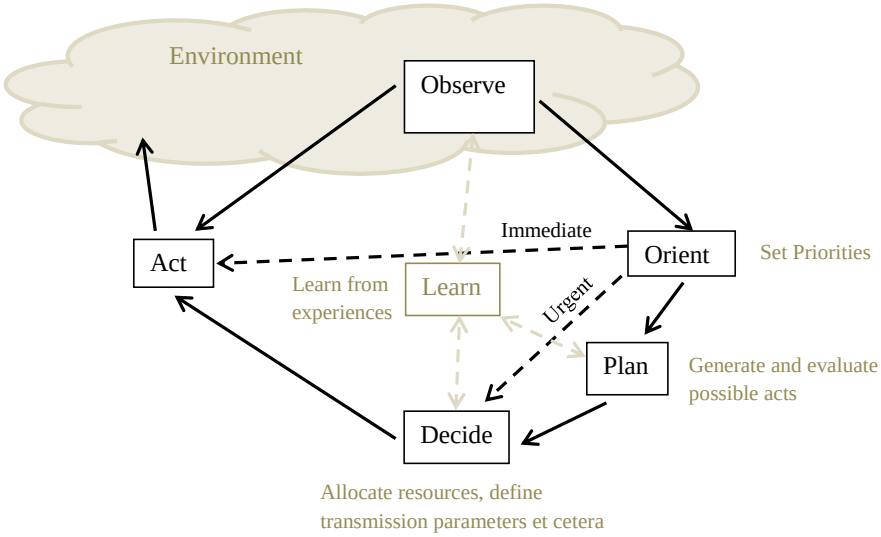

Figure 2.1: Cognitive cycle.

dress the critical aspects of CR technology that are preventing it from commercial acceptance.

The literal meaning of the word *cognitive* is *pertaining to the mental processes of perception, memory, judgement, and reasoning* [4]. CR is perceived to have all these qualities. The operation of CR as proposed by Mitola [9] through the well-known cognitive cycle is shown in Fig. 2.1. SU observes the environment and prioritises the actions in the orient phase (*perception*). Possible acts are generated and evaluated in the plan phase (*reasoning*). A decision is made based on the evaluation results in the decide phase (*judgement*) before an action is taken in the act phase. The radio learns through the process and hence is capable of taking cognitive decisions based on the experiences gathered through past actions and the associated consequences. In special cases, CR can jump directly to *act* or *decide* phase. The lessons learned in the past help CR in taking such immediate or urgent actions. This *memory* also helps in optimising the algorithms, protocols, etcetera in every subsequent iteration [1].

Based on the traffic pattern of the radio spectrum at a certain location, *time*, *frequency*, *space*, and *polarisation* may be shared among the PU and the SU. Time sharing of the frequency spectrum may be possible in packet based primary systems. Frequency sharing may be possible in broadcast systems by virtue of frequency reuse patterns. Space sharing may be possible based on the angular spread

[4] http://www.dictionary.reference.com

of the multipath. Polarisation may be shared among the PU and the SU depending on the propagation scenario, since multipath plays an important role in the change of the polarisation of the signal between the transmitter and the receiver. The possibility of sharing spatial (directional) resource for CR, in the context of directional antenna design, is explored in this thesis.

CR technology is in the development phase and a lot of different aspects are being addressed in the growing literature. The term "cognitive radio" returns over $5,000$ results for a title search on IEEE[5] explorer. This indicates the huge progress made in this area within the last one and a half decade of its origin. This involves research in the field of CR node and network architecture, spectrum sensing, transmission, antenna design, protocol, routing, outdoor/over-the-air measurements, etcetera. The following section briefly introduces the topic of spectrum sensing for CR, as it has been a major focus of the community during the last decade.

2.1.1 Spectrum Sensing

Spectrum sensing is a significant part of CR and an important stage of cognitive cycle. The focus of spectrum sensing has shifted to databases recently [54], where a central entity is assumed to supply information regarding the spectrum usage. Nevertheless, local spectrum sensing at node-level would increase the robustness against the short-term local changes in the environment [55].

The critical requirement for sensing algorithms is to detect weak primary signals close or below the noise floor with a high probability of detection. On the other hand, it may not be important to know the content of the signal which relaxes the requirement on synchronisation with the primary system. There are many sensing algorithms that assure reliable spectrum sensing with good sensitivity, for example, energy detection, matched filter detection, feature detections etcetera [19]. Energy detection is the simplest sensing algorithm which requires no a-priori knowledge about the PU. This technique is generally used in practice since it is easy to implement. However, it cannot detect signals below noise level. Other sensing techniques provide robustness at the cost of complexity. These techniques include *Matched filter detection* which makes use of the deterministic nature of the PU signal and performs coherent processing. This technique is more robust than energy detection and requires less sampling time but it relies on perfect synchronisation with the PU. Another well-known approach *feature detection* makes use of the periodicity in the modulated PU signals to perform sensing. Furthermore, collaboration of various sensing nodes can be utilised to improve the reliability of the sensing process by utilising the de-centralised spatial diversity. This, how-

[5]Institute of Electrical and Electronics Engineers

ever, results in heavy data exchange among the network nodes, thereby requiring a dedicated *common control channel*.

Energy detection is the most basic approach for detecting signals in the presence of noise [2]. It requires minimum information about the signal, namely bandwidth and centre frequency. It is a test of the following hypotheses

$$H_0 : y[n] = w[n] \tag{2.1}$$
$$H_1 : y[n] = x[n] + w[n] \qquad n = 1, ..., N \tag{2.2}$$

where N is the observation interval, $x[n]$ is the transmitted signal and $w[n]$ is the noise. The performance of this scheme is measured by the probability of false alarm (P_f) and the probability of detection (P_d). Decision about the presence of a signal is taken by comparing the received energy

$$E(y) = \sum_{n=1}^{N} y[n]^2 \tag{2.3}$$

with a threshold γ. The threshold is normally chosen to meet a specific probability of false alarm P_f

$$P_f = Q\left(\frac{\frac{\gamma}{{\sigma_w}^2} - N}{\sqrt{N}}\right) \tag{2.4}$$

where σ_w represents the receiver noise variance. The probability of detection can then be calculated as

$$P_d = Q\left(\frac{1}{1+SNR}Q^{-1}(P_f) - \sqrt{\frac{N}{2}}\frac{SNR}{1+SNR}\right) \tag{2.5}$$

where SNR is the signal-to-noise-ratio given by the formula

$$SNR = \frac{{\sigma_y}^2}{{\sigma_w}^2}, \tag{2.6}$$

σ_y and σ_w representing the signal and noise variance respectively. Signal and noise are considered as Gaussian random variables with zero mean. The number of samples required to achieve a certain P_d and P_f can be calculated from eq. (2.5) as

$$N = 2\left[Q^{-1}(P_f) - Q^{-1}(P_d)SNR^{-1} - Q^{-1}(P_d)\right]. \tag{2.7}$$

For very low SNR conditions ($SNR << 1$), number of samples required for a specific P_d and P_f are of the order of $1/SNR^2$.

Energy detection is the spectrum sensing technique that is simple to implement both in analogue and digital domain. Digital implementation involves FFT based spectral estimates and hence supports various bandwidths and detection of multiple signals simultaneously. Furthermore, spectrum sensing may be implemented using fixed FFT resolution [56] or variable FFT resolution [57] to perform coarse and fine sensing successively. This multi-resolution technique eliminates the need for tuning the RF circuitry to focus on interesting bands for fine resolution.

However, this algorithm does not support sensing for very low SNR conditions. The main cause for this limitation is the error in the estimation of receiver noise. The lowest SNR at which the signal can be detected successfully with an estimation error e in the presence of receiver noise can be calculated as [58]

$$SNR_{wall,dB} = 10log_{10}\left[10^{\frac{e}{10}} - 1\right]. \tag{2.8}$$

The interference sources in the neighbouring bands would also influence the detection of weak signals and would add to the sources of error, thereby raising the SNR wall. For the analyses in this thesis, eq. (2.3) is used to compute signal strength and is termed as received signal strength indicator (RSSI) in the rest of the thesis.

2.1.2 Antenna Design for Cognitive Radio

Antenna, being the first component of the reception, and last component of the transmission chain, acts as an interface between reconfigurable CR hardware and the communications environment. Moreover, it is the only component that interacts with the environment, either for sensing or for communications (reception and transmission). The explorable *white-spectrum* for CR is also defined by this constituent part of the radio chain. Thereby, using an antenna at its full capability can remarkably enhance the performance of CR. The focus of today's CR communications, and hence the CR antenna design, is on the frequency resource. Space is considered at times in the context of relaying, and collaborative spectrum sensing. However, equipping CR antenna with spatial dimension can extend the parameter space for CR. For example, an antenna with directional capability can suppress signals impinging/radiating in PU direction and increase link budget in the direction of SU. Moreover an antenna with directional capability can also help in direction of arrival estimation. The feasibility of directional antennas for CR is addressed in this thesis through specific approaches to the design and analysis of compact directional antennas.

A conventional CR node can be implemented as a wideband-narrowband system with two antennas for sensing and communications, i.e., a wideband antenna with two separate front-ends for sensing and communications, and a reconfigurable

narrowband antenna with a reconfigurable front-end [59]. For a long time, this approach was the focus of research in CR community. Ghanem et al. [20] presented a two-port antenna for cognitive radio where communications antenna was made multi-band using defected ground plane. Husseini et al. [60] employed switches along the length of a microstrip monopole to define resonance frequencies for communications antenna. Tawk et al. [61] proposed a rotatable two-port antenna where the resonance frequency of the communications antenna was changed by rotating a subset of the antenna structures. It is important to notice that these antennas provide only a few reconfigurable communications states.

Recently, single-port antenna designs have been proposed that consist of a wideband antenna with reconfigurable filters to provide access to a few narrow frequency bands [21] for overlay CR communications, and to reject narrow frequency bands [62] for underlay CR communications. Such an arrangement of filters on the radiating aperture of the antenna is likely to disturb the aperture field distribution and hence the radiation properties of the antenna. A better approach, follwed in this thesis, is to isolate the radiating aperture from signal processing with the help of a feed network behind the antenna.

However, frequency resource alone may not be sufficient to fulfil the needs of future communications systems. Future spectrum access technologies could imagine cognition beyond mere frequency resource [22]. A combination of frequency, space/direction and time can ensure a more efficient use of spectrum by employing techniques like direction-of-arrival estimation, interference mitigation etcetera. For example, making use of multiple antennas in the form of antenna arrays enables direction sensing and helps in location awareness of primary users. This can subsequently help in avoiding interference to PU while exploiting occupied licensed channels, for example, with (digital) beamforming. The utilisation of directional patterns for transmission and reception can, in addition, increase the link budget of a communications system by increasing directivity in certain directions and reducing interference from others. Situations like heterogeneous path loss conditions between primary and secondary systems [63], relay-assisted transmission of secondary users [23], etcetera may allow directional re-use of frequency spectrum.

Multiple receive antennas have been used for CR for primary user detection [63], [23] and/or interference suppression [64]. Pattern reconfigurable antennas have also been proposed in the literature. For example, [65] suggests an antenna that selects frequency and pattern by choosing one or multiple dipoles, [24] suggests an optoelectronic switch which could be used for frequency selectivity and pattern adaptability, and [66] uses PIN diodes on annular slot antenna for null-steering.

A novel concept is proposed in this thesis that enables frequency- and direction-selective sensing and communications using multi-band compact antenna systems where each degree-of-freedom is *simultaneously and separately* accessible at port-level.

2.2 Antennas and Arrays

The task of an antenna is to support the process of radiation by converting a guided transmission line wave to a free space electromagnetic wave. The most important characteristics of the antenna are, hence, the radiated far-field components of the electromagnetic wave. The power radiated by the antenna P_{rad} can be calculated by integrating the port beam pattern $\vec{f}\,(\Theta, \phi)$ over the radiation sphere (Θ, ϕ) as

$$P_{rad} = P_{in} \frac{1}{4\pi} \int_{\phi=0}^{2\pi} \int_{\Theta=0}^{\pi} \vec{f}^{H}\,(\Theta, \phi)\, \vec{f}\,(\Theta, \phi) \sin\Theta \; d\Theta \; d\phi, \tag{2.9}$$

where Θ and ϕ are the elevation and azimuth angle respectively, and P_{in} is the power fed to the antenna. The radiation power can be used to compute the radiation capability of the antenna using radiation resistance R_{rad} and radiation efficiency η_{rad} of the antenna [3]

$$R_{rad} = 2\frac{P_{rad}}{|\,\hat{i}\,|^2} = \frac{P_{rad}}{|\,i\,|^2}, \tag{2.10}$$

where $\hat{i}$ represents the peak current. The radiation efficiency η_{rad} is defined as the ratio of the power radiated by the antenna to the power accepted by the antenna P_{ant}

$$\eta_{rad} = \frac{P_{rad}}{P_{ant}}. \tag{2.11}$$

The remaining power $P_{diss} = P_{ant} - P_{rad}$ is dissipated. These losses can be reduced using a feed network. A signal incicident at the input of the antenna system with a feed network, shown in Fig. 2.2, first gets reflected from the input of the feed network P_{ref}. A part of accepted power P_{acc} would be dissipated in the feed network and the antenna, and the remaining power P_{rad} is radiated in free space. The amount of dissipated power depends on the material used for the antenna, the construction of feed network, etcetera. Hence the overall efficiency of the antenna is given by

$$\eta_{all} = P_{rad}/P_{in} = \eta_w \eta_{refl} = \eta_{ant}\eta_{net}\eta_{refl} \tag{2.12}$$

here $\eta_w = \eta_{ant}\eta_{net}$ is the efficiency of the antenna system and $\eta_{refl} = P_{acc}/P_{in}$ is the matching efficiency. Hence the total efficiency is composed of the antenna efficiency $\eta_{ant} = P_{rad}/P_{ant}$ and the network efficiency $\eta_{net} = P_{ant}/P_{acc}$.

Another important characteristic of the antenna is the directivity which states the directional properties of the antenna compared to an isotropic antenna. A better representation is the realised gain which considers the matching losses at the input port of the antenna system. Moreover, it is a proper choice for electrically small antenna arrays where matching plays an important role.

2.2.1 Antenna Arrays

The radiation and reception characteristics of an antenna can be controlled by changing the field distribution at the aperture of the antenna. This is easy to achieve for electrically large antennas, for example, aperture antennas [4, p. 1-23]. For small aperture antennas, discrete configurations are used to control the aperture distribution and hence the radiation or reception characteristics of the antenna. This leads to the concept of *antenna arrays*. The radiation characteristics of an antenna array can be controlled by selecting an appropriate arrangement of the array element, and amplitude and phase excited at the individual elements. Consequently, the concepts used for continuous aperture can be applied to this discrete aperture provided the spacing between the array elements is half a free-space wavelength. The resultant far-field of an n-port array depends on the amplitude and phase excitation a_m at the antenna ports. The radiated far-field $\vec{E}_f\left(r, \Theta, \phi\right))$ is the weighted sum of the patterns of the individual elements

$$\vec{E}_f\left(r, \Theta, \phi\right) = \sqrt{Z_F}\,\frac{e^{-jkr}}{r}\sum_m \vec{f}_m\left(\Theta, \phi\right)\, a_m \tag{2.13}$$

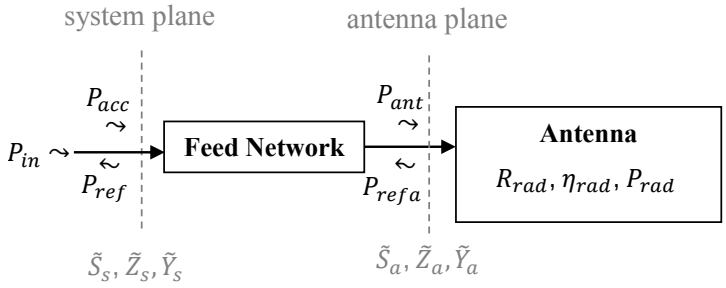

Figure 2.2: An antenna system with a feed network. The power incident on the antenna/feed network port is partly reflected and partly accepted.

where Z_F is the wave impedance, k is the wave number, and r is the distance from the antenna. When the inter-element spacing is less than half a free-space wavelength (for example, for electrically small (compact) arrays), the design becomes difficult due to coupling among the array elements. It is, therefore, difficult to set the amplitudes and phases of the elements independent from one another. The driving point impedance of the elements differ from their self-impedance because of the mutual coupling with other elements [4, p. 1-27]. This necessitates the design of an appropriate feed network for compact arrays that can provide decoupling at the ports. The design of such a feed network is addressed in section 2.2.5.

The excitation at the array elements, termed as array coefficient vector $\vec{e}$, can additionally provide a hint about the amount of power accepted by the antenna array P_{acc} as

$$P_{acc} = \vec{e}\left(\tilde{I} - (\tilde{S}_a)^H \tilde{S}_a\right)\vec{e}^H, \tag{2.14}$$

where $\tilde{S}_a$ is the scattering matrix of the antenna array, $\{\cdot\}^H$ denotes the complex conjugate transpose, and $\tilde{I}$ is the identity matrix.

Moreover, the current $\vec{i}$ and the voltage $\vec{v}$ can be used to compute the impedance and admittance matrices of the antenna array. The scattering, impedance, and admittance matrices are interchangeable since all these matrices originate from the current and voltage vectors. The current and voltage vectors can be used to compute the incident and reflected power waves as

$$\vec{a} = \frac{1}{2}\frac{\left(\vec{v} + Z_0\vec{i}\right)}{\sqrt{|\Re\{Z_0\}|}}, \tag{2.15}$$

$$\vec{b} = \frac{1}{2}\frac{\left(\vec{v} - {Z_0}^*\vec{i}\right)}{\sqrt{|\Re\{Z_0\}|}}, \tag{2.16}$$

where Z_0 is the characteristic impedance of the ports. These power waves are related to the scattering matrix as

$$\vec{b} = \tilde{S}\vec{a}. \tag{2.17}$$

The impedance and admittance matrices, on the other hand, are related to the current and voltage vectors as

$$\vec{v} = \tilde{Z}_a \cdot \vec{i}, \tag{2.18}$$

$$\vec{i} = \tilde{Y}_a \cdot \vec{u}. \tag{2.19}$$

The impedance, admittance, or scattering matrix can be used to compute the power accepted by the antenna array and hence the radiation resistance of the antenna array. For lossless case ($P_{acc} = P_{rad}$), the radiation resistance $R_{rad} = P_{rad}/P_{in}$ for an array may be calculated as

$$R_{rad} = \frac{\Re\left\{\vec{i}^H \tilde{Z}_a \vec{i}\right\}}{\vec{i}^H \vec{i}} = \frac{\vec{i}^H \tilde{R}_a \vec{i}}{\vec{i}^H \vec{i}}, \tag{2.20}$$

$$R_{rad} = \frac{\vec{v}^H \vec{v}}{\Re\left\{\vec{v}^H \tilde{Y}_a \vec{v}\right\}} = \frac{\vec{v}^H \vec{v}}{\vec{v}^H \tilde{G}_a \vec{v}}, \tag{2.21}$$

$$R_{rad} = Z_0 \frac{\vec{e}\left(\tilde{I} - \tilde{S}_a^H \tilde{S}_a\right)\vec{e}}{\vec{e}\left(\tilde{I} - \tilde{S}_a\right)^H \left(\tilde{I} - \tilde{S}_a\right)\vec{e}}. \tag{2.22}$$

Hence, the radiation resistance of an antenna array depends on its excitation. This implies that the radiation power (eq. (2.9)), radiation efficiency (eq. (2.11)), bandwidth, and the radiation quality factor also depend on the array excitation vector [10, p. 10]. Since there are infinite number of excitation vectors that can be utilised for antenna arrays, the characterisation of antenna arrays becomes challenging. This implies that the performance of an antenna array with a given geometry, number of elements, inter-element spacing, etcetera is hard to evaluate independent of the excitation vector. It becomes even more challenging for compact antenna arrays. Eigen-analysis [11] of the radiation matrices of the antenna array provides a good tool to compare various antenna arrays.

2.2.2 Eigen-analysis of Antenna Arrays

Eigen-analysis helps in evaluation of antenna arrays by providing a set of orthogonal basis vectors of the radiation matrix $\tilde{H}$ of the antenna array. The concept of eigen-modes was first introduced by Chaloupka et al in [67]. A detailed analysis, briefly described here, has been presented in [11, 25].

The radiation matrix $\tilde{H}$ can be computed from the scattering matrix of the antenna system $\tilde{S}_a$ for the lossless case, as

$$\tilde{H} = \left(\tilde{I} - \tilde{S}_a^H \tilde{S}_a\right). \tag{2.23}$$

When compared with eq. (2.14), it can be observed that this matrix helps in the calculation of power accepted by the antenna array for specific excitation vectors. For a decoupled array, the non-diagonal elements of the matrix are 0 indicating no transfer of power among neighbouring ports. Non-zero diagonal elements are obtained for complex arrays. The radiation matrix may also be computed from

radiation patterns of the individual elements [11]. This ensures that the losses in the array are considered for the calculation of $\tilde{H}$. In this thesis, however, scattering matrices are used to compute the radiation matrix. This matrix is Hermitian and can be diagonalized using eigen-value decomposition

$$\tilde{H} = \tilde{V}^H \tilde{\Lambda} \tilde{V}, \tag{2.24}$$

where the columns of $\tilde{V}$ contain the eigen-modes, and the diagonal values of ($\tilde{\Lambda} = \{\lambda_1, \lambda_2, ..., \lambda_n\}$) indicate the eigen-efficiencies with which the respective modes radiate. Eigen-modes are orthogonal to each other, i.e., $\vec{a}_i^H \vec{a}_j = 0$, and they do not exchange power, i.e., $\vec{a}_i^H \tilde{H} \vec{a}_j = 0$, where $\vec{a}_i$ and $\vec{a}_j$ are two different eigen-modes. The eigen-efficiencies λ_i are less than or equal to one. The smallest efficiency λ_{min} is the limiting factor for compact antenna arrays as discussed in detail in [25].

Eigen-modes of an antenna array are the basis functions of an antenna array that can be used to characterise the performance of the antenna array. These are the orthonormal vectors that can be superimposed to create any radiation pattern possible with the array. The resultant excitation vectors, columns of the excitation matrix $\vec{T_a}$, must ensure decoupling and matching by satisfying

$$\tilde{T_a}^H \tilde{H} \tilde{T_a} = \tilde{I} \tag{2.25}$$

This condition can be fulfilled by the excitation matrices

$$\tilde{T_a} = \tilde{V} \tilde{\Lambda}^{\frac{-1}{2}} \tilde{\tau}, \tag{2.26}$$

where $\tilde{\tau}$ represents any unitary matrix. Hence, there are infinite number of excitation vectors that ensure decoupling and matching. These excitation vectors $\vec{t_i}$ ensure the excitation of orthogonal port beam patterns, in the sense that they do not exchange power. But they are orthogonal among themselves only when they are equal to the eigen-modes.

2.2.3 Correlation Coefficient

Eigen-analysis of the antenna arrays helps in characterisation of antenna arrays in terms of their beamforming capability, by identifying the lowest eigen-efficiency. The eigen-modes are by definition orthogonal and hence there is no exchange of power. However, for arbitrary modes, correlation coefficient among the beam patterns is an important parameter. The correlation coefficient ρ_{lk} between port l

and port k can be computed as

$$\rho_{lk} = \frac{\int_0^{\pi}\int_0^{2\pi} \vec{f}_l\left(\Theta,\phi\right)\vec{f}_k\left(\Theta,\phi\right)\sin\Theta\, d\Theta\, d\phi}{\sqrt{\int_0^{\pi}\int_0^{2\pi}\left|\vec{f}_l\left(\Theta,\phi\right)\right|^2\sin\Theta\, d\Theta\, d\phi}\sqrt{\int_0^{\pi}\int_0^{2\pi}\left|\vec{f}_k\left(\Theta,\phi\right)\right|^2\sin\Theta\, d\Theta\, d\phi}}. \quad (2.27)$$

It computes the amount of power exchange between port l and port k in the far-field. This power exchange has a direct effect on the antenna ports [26]. When ρ_{lk} is 0, it indicates that there is no power exchange among the port beam patterns, for example for eigen-modes. When the value is close to 1, the patterns are overlapping. This parameter is used for the characterisation of the antenna systems in this thesis. It serves as a metric to compute the orthogonality among directional patterns at one frequency and self-similarity among patterns at multiple frequency bands.

This work assumes that the reciprocity theorem [3] holds for the designed antennas, although the performance of the antennas is only evaluated for the receiving case. Nevertheless, it has to be underlined that there are also systematic differences. For instance, impedance matching towards a low noise amplifier (LNA) is required for transmission, whereas noise matching is necessary for reception. This work deals with impedance matching of $Z_0 = 50\ \Omega$. Noise matching would require an impedance depending on the LNA used. This change, however, does not alter the following design considerations.

2.2.4 Compact Antenna Arrays

An antenna array is called compact or electrically small when the inter-element spacing is less than $\lambda/2$, where λ is the free space wavelength. Less inter-element spacing leads to *mutual coupling* between the array elements. This phenomenon can be illustrated with the help of Fig. 2.3. When an ideal lossless antenna $\#1$ matched to the impedance of transmission line Z_0 is fed with an electromagnetic wave, it radiates all energy to free space without any reflection back to the antenna port ($\Gamma = 0$). However, when such an ideal antenna is placed in the vicinity of another antenna $\#2$, the wave radiated from the other antenna would behave as a reflection at this antenna port $\Gamma \neq 0$. This reflection appears as an impedance mismatch at the port of antenna $\#1$, resulting in antenna impedance [5, p. 339]

$$Z_L = Z_0\frac{1+\Gamma}{1-\Gamma}. \quad (2.28)$$

This dependence leads to the fact that the element impedance changes for any change in the array excitation, since the coupling from the neighbouring elements changes. In consequence, digital beamforming with highly coupled antenna ar-

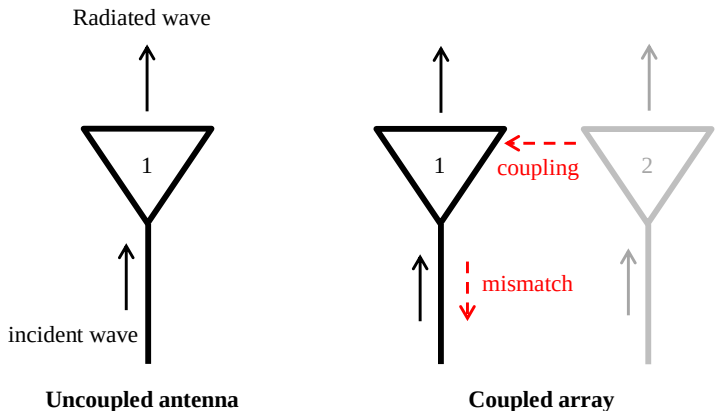

Figure 2.3: Illustration of the mutual coupling phenomenon . An ideal isolated antenna $\#1$ with no reflection to the input port (left) and a coupled array with reflection due to the neighbouring inactive element $\#2$ (right).

rays is complicated, since the port impedances change with changing excitation coefficients.

A solution to this problem is to decouple the antenna ports using a decoupling and matching network such that the scattering matrix at the antenna system ports is zero. This ensures that there is no coupling between the antenna ports and the modes excited at the ports of this analogue network are matched to system impedance. These excited modes can then be used for digital beamforming. When the eigen-modes of the radiation matrix, as explained above, are excited with such a network, all radiation degrees-of-freedom of the antenna array are preserved at the network ports as discussed in detail by C. Volmer in his doctoral thesis [11].

2.2.5 Decoupling and Matching Networks

Decoupling and matching networks (DMN) can be designed using the eigen-mode excitation or arbitrary excitation vectors. In [11, chapter 3], directional couplers are proposed to excite eigen-modes of the coupled array. Various other methods have been proposed in the literature for the excitation of orthogonal modes, e.g., N. Amitay [27] discusses the use of reactive elements to reduce the coupling between antenna elements, J. Andersen et al. [28] proposed the design of DMN using transmission lines, J. Chaloupka [29] suggested the design of a two step DMN, J. Weber [30] presented the design of a single step decoupling and matching network with the liberty to excite any orthogonal vectors at the antenna ports. The technique proposed by J. Weber, in his doctoral thesis [10], is used in this work for the generation of orthogonal directional modes for compact ar-

rays. High quality factor low tolerance off-the-shelf components are used for the realisation of the DMN. Reconfigurable feed network designs are also proposed, where varactor diodes are used as reconfigurable capacitors.

The design approach of DMN, adapted in this thesis, is presented in [10, chapter 4]. The design process starts with the selection of a suitable set of excitation vectors $\tilde{T_a}$. The vectors can be calculated using the eigen-modes of the radiation matrix, $\tilde{T_a} = \tilde{V}\tilde{\Lambda}^{-1/2}$, or any other set of orthogonal vectors as presented in eq. (2.26). $\tilde{T_a}$ can then be used to obtain $\tilde{T_u}$, the voltage amplitudes and phases that should be provided at the array ports to excite the respective radiation modes,

$$\tilde{T_u} = 2\left(\tilde{I} + \tilde{Y_a}Z_o\right)^{-1} \cdot \tilde{T_a} = \tilde{T_{uR}} + \tilde{T_{uI}}, \tag{2.29}$$

where $\tilde{Y_a} = \tilde{G_a} + j\tilde{B_a}$ denotes the admittance matrix of the array, and Z_o is the reference impedance ($Z_o = 50\ \Omega$ in many cases). The network admittance matrix $\tilde{Y_n}$ can then be calculated from [30] as

$$\tilde{Y_n} = j\begin{pmatrix} Z_o{}^{-1}\tilde{T_{uI}}{}^{-1}\tilde{T_{uR}} & -Z_o{}^{-1}\tilde{T_{uI}}{}^{-1} \\ -\tilde{G_a}\left(\tilde{T_{uR}}\tilde{T_{uI}}{}^{-1}\tilde{T_{uR}} + \tilde{T_{uI}}\right) & \tilde{G_a}\tilde{T_{uR}}\tilde{T_{uI}}{}^{-1} - \tilde{B_a}. \end{pmatrix}. \tag{2.30}$$

The admittance matrix $\tilde{Y_n}$ can be used to obtain a layout of the DMN in terms of capacitors and inductors. The negative counterparts of the off-diagonal elements of $\tilde{Y_n}$ represent the required reactance between the respective ports. The sum of the k-th row provides the shunt reactance required at the k-th port ($1 \leq k \leq n$) [30]. Such a feed network has the advantage that it can be designed for any set of orthogonal excitation vectors, consumes less space, can be realised with off-the-shelf lumped elements.

The design equations (2.29) and (2.30) are used to obtain decoupling and matching network for the compact multi-band directional antenna arrays. The reduction in the number of network elements is performed through numerical simulations. Quasi-lumped elements, used for realisation of the feed networks by J. Weber, provide the flexibility that any reactance value can be realised. However, the design of quasi-lumped elements is frequency dependent. Surface mount capacitors and inductors with low tolerance ranged are used in this thesis. The terms decoupling and matching network and feed network are interchangebly used for such networks in the thesis.

2.3 Evaluation Methodologies

Antennas are traditionally characterised inside an anechoic chamber, in a line-of-sight (LOS) environment. In reality, however, there are components in addition to LOS, e.g., reflections from large objects, diffraction from edges, scattering from irregular objects, etcetera. Hence, the waves may travel from the transmit antenna to receive antenna through more than a single LOS path. These multiple paths impinge on the receive antenna from different angles, and with different amplitudes and phases. They may add up constructively or destructively at the receive antenna, depending on the complex magnitude. The wave paths may also change with time depending on the movement of the transmitter, receiver, or the nearby objects (environment). This results in changing the amplitudes and phases of the impinging waves (multipath), and hence the resultant signal at the antenna port. This signal behaviour is referred to as *small-scale fading*. Moreover, shadowing from large objects/building, is referred to as *large-scale fading*.

Multipath and large-scale fading are more important for *directional antennas* as compared to *omnidirectional antennas*. For example, depending on the power angular profile (PAP) of multipath, *white-space* may become available for directional communications in CR. Therefore, the spatial structure of the channel becomes important for the evaluation of directional antennas for CR communications. With this motivation, simulations and measurement campaigns are performed to evaluate directional antennas for CR. A brief description of the evaluation methodologies, and their application in context of CR, is provided in the following sections.

2.3.1 Simulations

Channel simulations are generally performed to observe a communications system's performance (for example, routing protocol, or medium access protocols, etcetera) in multipath scenarios. In these simulations, amplitudes, phases, polarisations, and angle-of-arrivals (AOA) of the signals are mostly simulated as random values. In the absence of line-of-sight (LOS) and mobility (in a less rich scattering environment), the amplitudes are considered as Rayleigh distributed, the phases as normal distributed from 0 to 2π, and AOA as uniformly distributed in space [4, chapter 58]. The assumptions about amplitudes and phases are based on the central limit theorem, and those about AOA on the consideration that the antenna of mobile handset is oriented randomly in space.

The kind of antennas considered in the thesis are not necessarily handset antennas. Hence, the intention for the simulations is to stay as close to reality as possible. A pre-requisite for these simulations is to consider the angular behaviour of mul-

tipath. The conventional random distribution of AOA may not suffice the needs for these simulations.

The simulations in this thesis are based on the channel models extracted from measurement campaigns [68, 69]. The influence of propagation scenarios from rural to highly urban environments, and the influence of antenna patterns on the existence of directional opportunity are discussed in section 6.1.

2.3.2 Measurement campaigns

Measurement campaigns are the optimal option for evaluation of directional opportunity for CR. However, measurements call for proper planning, demand extremely high efforts, and are scenario-specific. They are representative of the scenario: static or mobile, big city or small town, etcetera, in which they are performed.

Various measurement campaigns have been performed for CR. For example, [70] describes the performance of energy detection for various measurements. The probability of detection and false alarm are compared for various primary signals and it is concluded that the performance of energy detection is dependant on the type of the sensing signal. Indoor and outdoor measurement campaigns were performed in Aachen [51] to study the effect of ambient noise on energy detection accuracy. A survey about various spectrum sensing measurement campaigns performed worldwide has been presented in [71]. The results from various measurement campaigns could not be compared directly since they were performed at different geographical locations and time, and employed different evaluation methodologies.

A couple of measurements are also reported in this thesis. These measurement campaigns differ from the state-of-the-art in the sense that directional resources are considered in addition to the frequency resources. After getting encouraging results from these measurement campaigns, further analyses are carried out in simulations.

2.3.3 Over-the-air testing

Over-the-air (OTA) measurements inside an anechoic chamber provide the flexibility to test the performance of the antenna in a controlled environment [31, 46]. Such measurements are different compared to the conventional antenna measurements in the sense that the signals impinging on the antenna under test (AUT) are not LOS. The multipath effect can be emulated in OTA testing lab with the help of a ring or semi-sphere of probe antennas surrounding the antenna/device under test (DUT). This ring of probe antennas helps in the generation of the spatial characteristics of multipath around AUT/DUT. The surrounding probe antennas are fed

with signal generators and fading emulators that altogether generate spatial and temporal distribution of multipath with different path powers.

An OTA test could be helpful for directional CR, since it emulates the PAP of multipath propagation channel. Moreover, such a test is repeatable and controllable. These features help in the evaluation of CR node at various development stages, and different test complexity levels [46]. Moreover, the whole RF chain for CR can be evaluated using such tests.

OTA laboratory is under construction at Ilmenau University of Technology [72]. An initial OTA test performed for the evaluation of a reference multi-band directional antenna for CR is presented in section 3.3.1. Moreover, the measured antenna patterns of the realised antenna systems are embedded on to the channel parameters obtained from channel sounder measurements performed in Ilmenau. This procedure is termed as *emulation* in the thesis. The results of these emulations are presented in detail in section 6.2.

3. FEASIBILITY OF DIRECTIONAL ANTENNAS FOR COGNITIVE RADIO

The design of directional antennas for CR, and the proof-of-principle measurement results are presented in this chapter. Design considerations for directional antenna are presented in section 3.1. A reference multi-band directional antenna system is proposed in section 3.2. This antenna system employs a concentric multi-band array arrangement and achieves the directional patterns through absorber and metal walls in two development stages. The proof-of-principle measurement campaigns were performed using these reference antenna systems. The results of these measurement campaigns are presented in section 3.3.

3.1 Design Considerations

The following subsections introduce the important parameters that need to be considered to design directional antennas for CR.

3.1.1 Spectral and Spatial Bins

Spectral (frequency) resources are a pre-requisite for CR, as they are the most prominent resources that have been frequently studied as a candidate for CR. Addition of spatial (directional) resource to the conventional frequency resource can enhance the capability of CR. However, the antenna for CR may not provide access to infinite frequency resources and yet be highly adaptable in terms of its spatial selectivity. Hence, a choice has to be made on the frequency bands of interest and spatial adaptability.

The focus of this work was on the existing infrastructure, hence GSM 1800 MHz, GSM 900 MHz, and IEEE 802.11 b/g were considered as the frequency resources. For directional antenna design, three directional resources were considered to cover 360^0 in azimuth, at all frequency resources under consideration.

3.1.2 Spectral and Spatial Interface

An ideal antenna for spectral and spatial sensing should be multi-band and able to detect the spectral resources in different directions using multiple beams. The

antenna designs described in the literature so far provide all degrees-of-freedom to be accessible at one port, through a few reconfigurable states. The resources are therefore separable only through analogue or digital signal processing after the antenna port. Moreover, the current designs consider filters to be directly embedded into the antenna which may also deteriorate the radiative properties and efficiency of the antenna. In order to define this interface more carefully, the spatial and spectral interfaces can be disembodied from the actual antenna. This ensures undisturbed radiative properties of the antenna.

Compact multi-band antennas are proposed as a solution to access all spatial and spectral degrees-of-freedom simultaneously yet separably. This is achieved by providing orthogonal radiation patterns at well-separated frequency bands. The radiation patterns at different frequency bands are self-similar. Each of these frequency and directional resources is accessible at a separate port.

The corresponding sensing strategy could be that the antenna searches for all degrees-of-freedom in the sensing mode and then utilises the best available opportunity by connecting to the respective degree-of-freedom in the communication mode. If a separate communication transceiver is available, the antenna can sense and transmit at the same time. With a careful design of the waveform, it may be possible to access multiple degrees-of-freedom at the same time to enhance the capacity of the secondary link.

3.1.3 Flexibility Versus Complexity

A fully adaptive array with highly controllable radiation pattern (beamwidth, sidelobe level etcetera) would require a large number of elements with a tunable phase-shifter and a tunable amplifier behind every element, resulting in a complex antenna system with high power consumption.

An antenna system, consisting of a multi-band multi-port array and a multi-band multi-port feed network, provides the spectral and spatial selectivity at the system port level. In its full capability, the CR node can process each degree-of-freedom simultaneously. This would, however, lead to a complex, expensive and power-consuming hardware. On the other extreme, switching circuits can be used to access the degrees-of-freedom in a consecutive way (time division multiplexing). This would, however, introduce latency depending on the switching speed. This trade-off exists and is not studied within the scope of this thesis.

The complexity of such an antenna system would also increase with an increase in the degrees-of-freedom. An increase in the *directional* degrees-of-freedom would introduce complexity in the feed network, and an increase in the *frequency* degrees-of-freedom would require extra antenna elements. Hence, flexibility can

be introduced at the expense of complexity. This work is limited to three frequency bands and three directions, giving rise to nine degrees-of-freedom in total.

3.2 Reference Antenna System

In order to design an elementary antenna system with individual access to the frequency degrees-of-freedom, three concentric antenna arrays of monopole were designed. These concentric arrays were resonant at three selectable frequency bands: GSM 900 MHz, GSM 1800 MHz, and IEEE 802.11b/g. Each array consisted of three $\lambda/4$ monopoles at vertices of an equilateral triangle, optimum arrangement for a 3-element array [49]. These triangles of monopoles form an array at 900 MHz (outer), 1800 MHz (middle) and 2450 MHz (inner) as shown in Fig. 3.1. The directional selectivity in this laboratory version of the antenna was achieved with the help of absorber and metal walls, for the measurement campaigns.

Moreover, such an arrangement can be made compact by reducing the electrical spacing between the array elements. Such a compact multi-band multi-port antenna array must, therefore, be connected to a feed network while preserving the port-level access to all degrees-of-freedom. The design of the feed network for compact concentric arrays is discussed in section 4.3. This multi-band feed network can be combined into one network using reconfigurable components, for example, varactor diodes as discussed in section 4.3.3 [44]. Moreover, the individual feed networks can also be made reconfigurable to cover a range of fre-

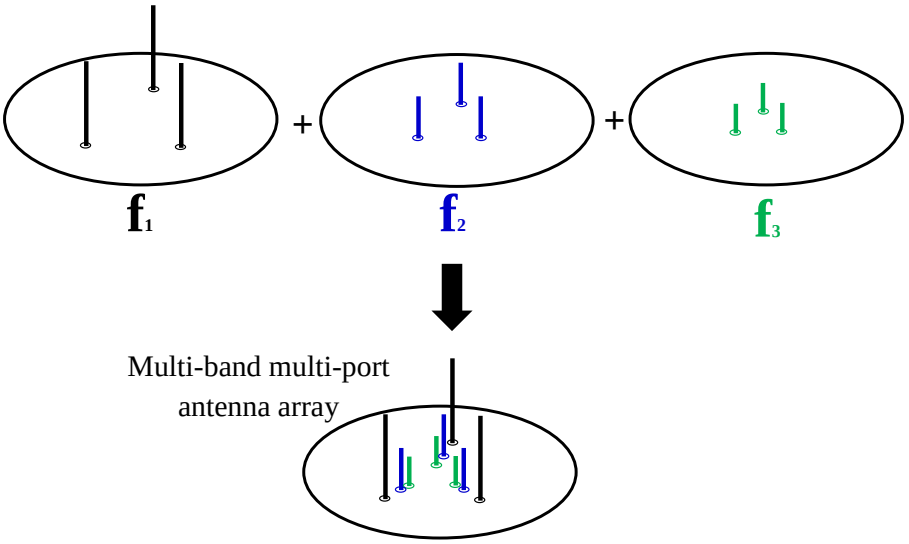

Figure 3.1: Sketch and the formation of the proposed generic multi-port multi-band antenna array operating at three frequencies f_1, f_2, and f_3 illustrated with black, blue, and green colours, respectively.

quencies within a certain band of interest. The tuning ranges may vary from a few MHz to hundred MHz depending on the number of tunable components in the network, degree of compactness, etcetera. Such reconfigurability behind the antenna aperture does not influence the radiation properties of the antennas as in case of the state-of-the-art reconfigurable antennas.

In the next sections the feasibility of such an array arrangement is studied for the identification of directional opportunities through measurement campaigns. Measurements were performed to evaluate the capability of the proposed antenna system, and to identify the existence of directional resources for CR.

3.3 Proof-of-Principle Measurement Campaigns

The following sections describe the proof-of-principle measurement campaigns performed in order to get a proof.of.principle on the availability of directional resources for CR.

To gain a proof-of-principle, measurements were performed for a line-of-sight (LOS) and a multipath scenario. The LOS measurements were performed in an anechoic chamber while the multipath measurement campaign was performed outdoor. For both measurement campaigns, a laboratory version of the reference antenna system was built. The antenna system was connected to a commercial wideband transceiver USRP2 (Universal software radio peripheral) from Ettus research lab [1], which was accessed with MATLAB [2] for reconfiguration and baseband processing. These two building blocks form a CR node that is used for sensing in the following measurement campaigns.

3.3.1 Line-of-Sight Measurements in an Over-the-Air Test Setup

A laboratory version of the CR node was tested in receive mode in an over-the-air (OTA) test setup [45]. The setup and the main results of this measurement campaign are discussed below.

3.3.1.1 Cognitive Radio Node

The CR node consisted of a laboratory version of the proposed multi-band directional antenna system connected with a commercial wideband transceiver USRP2. The directional patterns were obtained by placing a Y-shaped absorber wall between the elements of the proposed antenna arrays on a rectangular ground plane. These absorber walls divide the hemisphere above ground plane in three distinct sectors as shown by the resulting measured radiation patterns in Fig.

[1] Ettus Research. http://www.ettus.com.

[2] MATLAB. version 7.10.0 (R2010a). The MathWorks Inc., Natick, Massachusetts, 2010.

3.2(b). The beamwidth of the directional patterns is not identical because of asymmetric Y-shaped absorber walls defining the sectors. The respective realised gain shown in Table 3.1 confirm this asymmetry. This asymmetry in the radiation patterns, however, does not influence the following analysis. Moreover, the desired characteristics of the antenna system, orthogonality among the directional patterns at one frequency band and self-similarity of patterns at different frequency bands, are shown in Table 3.2 and 3.3 respectively. The orthogonality and self-similarity is computed using correlation coefficient of eq. (2.27).

A switch network was used behind the antenna arrangement to provide access to all degrees-of-freedom using a single wideband receiver. The initialisation and control of the USRP2 device, data acquisition, switch control, and post-processing was implemented in MATLAB on a personal computer. USRP2 was used for off-line, instead of real-time, processing. *RFX2400* (full-duplex transceiver for Wi-Fi frequency range of 2.3 - 2.9 GHz) and *WBX* (full-duplex wideband transceiver for 50 MHz - 2.2 GHz) daughter boards were used for the realisation of the CR node. Averaging of 100 samples per snapshot was used for elimination of time variant non-linearities of the receiver. For the observation of frequency ranges wider than

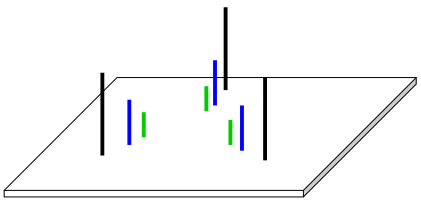

(a) Sketch of the multi-port multi-band antenna array with square ground plane

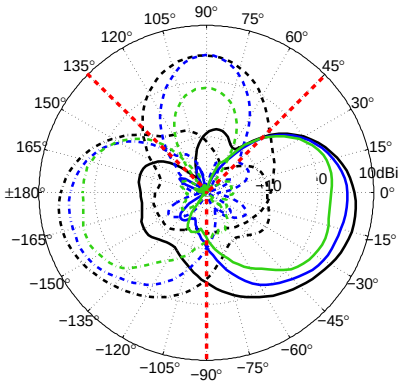

(b) Azimuth-cut of the proposed antenna system with absorber walls

Figure 3.2: The antenna consisted of three monopole arrays operating at GSM 900 MHz, GSM 1800 MHz, and IEEE 802.11 b/g shown in black, blue, and green colour, respectively. The radiation patterns are shown in black, blue, and green colour respectively. 18 cm tall absorber walls were used in this design to define directional patterns d_1 (solid), d_2 (dashed), and d_3 (dotted). The placement of absorber walls are shown by dashed red lines. The ground plane measures 40 cm $\times$ 40 cm.

Table 3.1: Measured Gain of a laboratory antenna with absorber walls, over all θ and ϕ in different frequency bands and directions, in dBi

Directions	**Frequency bands**		
	f1	**f2**	**f3**
d1	4.91	7.96	2.52
d2	7.63	9.69	7.58
d3	8.18	10.21	7.72

Table 3.2: Orthogonality (eq. (2.27)) among directions of the reference antenna (Fig. 3.2(b)), with respect to d_1.

Directions	**Frequency bands**		
	f_1	f_2	f_3
d_2	0.011	0.010	0.040
d_3	0.009	0.008	0.038

Table 3.3: Self-similarity (eq. (2.27)) among frequency bands of the reference antenna (Fig. 3.2(b)), with respect to f_1.

Directions	**Frequency bands**	
	f_2	f_3
d_1	0.712	0.862
d_2	0.739	0.896
d_3	0.758	0.890

the data transfer bandwidth of USRP2 (25 MHz), the carrier frequency was swept.

3.3.1.2 Test Setup

OTA testing accounts for the real antenna and radio channel characteristics, and enables the simultaneous excitation of the CR node from different directions at different frequency bands. For this measurement, a static channel was used without any distinction between primary and secondary users, thereby emulating LOS links between the CR node and virtual surrounding users. The CR node was not used for uplink within this measurement campaign. The details of the OTA test-bed for CR nodes were discussed in [46]. This test was the first phase of a projected, more complex OTA test and deals with an observation of radio environment under LOS conditions only.

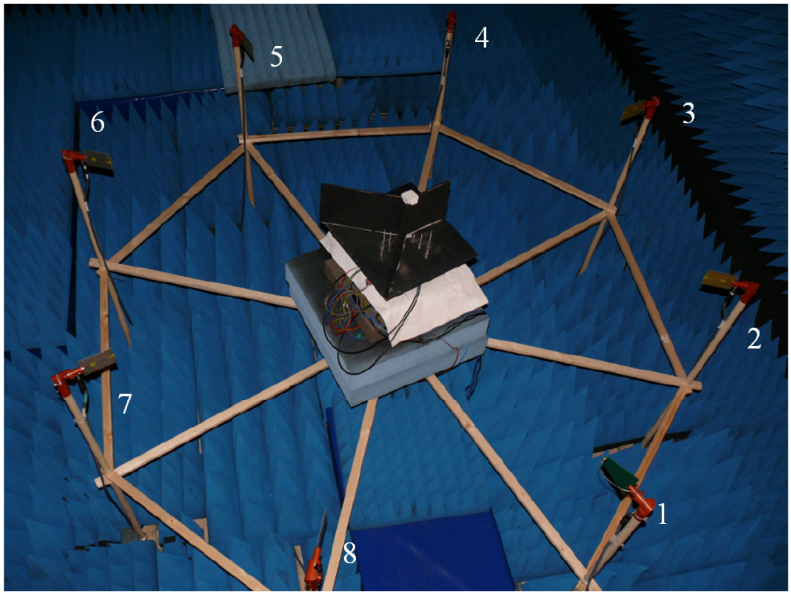

Figure 3.3: The CR node (multi-port multi-band directional antenna system with absorber walls, USRP2 and switch network) placed in the centre of OTA ring. The antennas $\#1$ - $\#8$ denote the transmitting antennas of the OTA ring.

Eight wideband transmit antennas were used in a circular arrangement. The antennas were mounted on a wooden structure, as illustrated in Fig. 3.3. The transmit antennas consisted of six Vivaldi antennas with a gain varying between 2 and 7 dBi across a frequency range from 1.8 to 3 GHz, and two log-periodic dipole antennas (LP0926 by Ettus) with a gain of $5 - 6$ dBi in the range of $900 - 2600$ MHz. Each transmit antenna was fed with a fictitious user signal. Two of these signals were transmitted in the 900 MHz band, three in the 1800 MHz band, and three in the 2450 MHz band.

A static 9 MHz wide multi-carrier signal, generated by a vector signal generator (R & S[3] SMU200A), was used as the main test signal. Using slight shifts in the carrier frequency, eight equally shaped but non-overlapping spectra were generated, representing the different users. This test signal was up-converted to the aforementioned frequency bands with the help of mixers of a wideband fading emulator (Elektrobit[4] PROPSim C8). Since the measurements were LOS, the full capability of the fading emulator was not used. Arbitrary waveform/vector signal

[3]Rohde & Schwarz. Muehldorfstrasse 15, 81671 Munich, Germany. http://www.rohde-schwarz.com.

[4]Elektrobit. Hannoversche StraÃ§e 60B, 38116 Braunschweig, Germany. http://www.elektrobit.com.

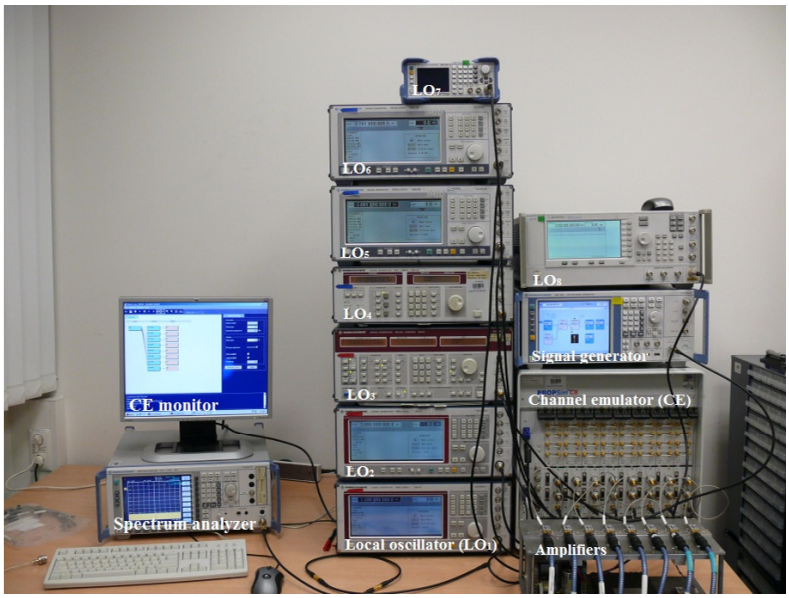

Figure 3.4: OTA signal generation setup with the different measurement units indicated in the figure and further explained in the main text.

generators by R&S and Agilent were used as local oscillators. After mixing of the channel emulator, the lower side-bands were used as transmit signals. Fig. 3.4 shows a picture of the whole signal generation setup in the control room of the anechoic chamber. An illustration of the different test signals (power spectra) and an allocation to the transmit antennas is illustrated in Fig. 3.5. The power level of the main transmit signal was -5 dBm. Each local oscillator (LO) had a power of 0 dBm. To cope with the cable attenuation (about 5 to 6 dB), a bank of power amplifiers (PA , Mini-circuits[5] ZX60-2534M+) were used after the mixer stage. At the beginning of the OTA test, the setup was checked in a conducted way, to calibrate attenuations and emulator settings. Next, the signals for OTA transmission were calibrated to have a magnitude of -15 dBm at the output of the PA. Thereafter, the actual OTA-test was performed by rotating the receiver antenna system of the cognitive node in steps of 45^0.

3.3.1.3 Measurement Results and Discussion

Each measurement at different frequencies and directions revealed the desired signal, the interference from other directions, and further non-idealities from the receiver. The power spectral density (PSD) sensed from different directions is shown in Fig. 3.6 for GSM 1800 MHz as an example. In general, a signal-to-

[5]Mini-Circuits Europe Dale House, Wharf Road Frimley Green, Camberley, Surrey GU16 6LF, England.

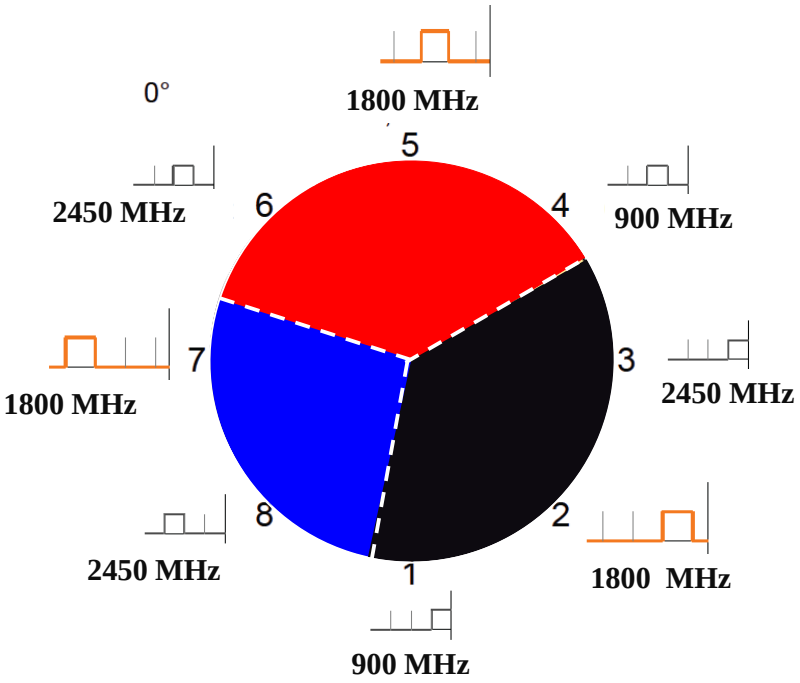

Figure 3.5: Illustration of the OTA test signals (power spectra histograms along the outer contour of the diagram). There were only two 900 MHz signals (terminals $\#1$ and $\#4$). Starting from the reference point (terminal $\#$ 8, in the 0^0 direction), the antenna with three segments (blue, red, black) was rotated counter-clockwise.

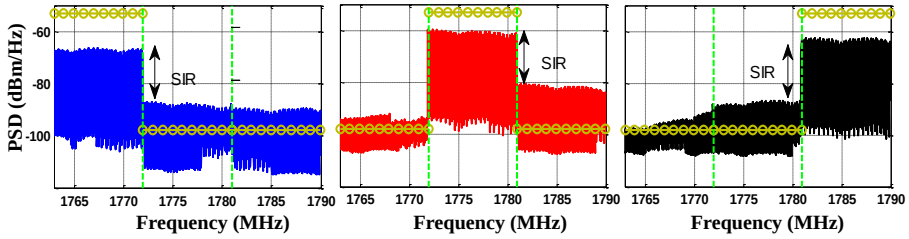

Figure 3.6: Typical measurement results at 0^0 (referred to Fig. 3.5) for all receive directions d_1-d_3 at 1800 MHz. The different coloured signals correspond to the respective sectors in Fig. 3.5. The yellow envelope indicates the expected signals and the green lines separate the signals transmitted in different sectors. Signal-to-interference-ratio (SIR) of about 20 dB is observable among sectors.

interference-and-noise-ratio (SINR) of 20 dB or more was observed in all frequency bands. Fig. 3.6 illustrates the results at 0^0 orientation of the receive antenna. Similar results were obtained as the antenna was rotated counter clockwise in steps of 45^0. However, the interference from undesired directions was relatively higher when the transmit terminals were at the border of the dividing absorber walls of the receive antenna (overlap regions of the respective radiation patterns). This test yielded a proof-of-principle that if the proposed antenna system provides directional beams with reasonably low side-lobe levels, a good SINR can be achieved, at least under LOS conditions.

3.3.2 Outdoor Measurement Campaign

After the initial LOS measurements, it was reasonable to perform outdoor measurements to observe the situation of directional opportunity in a multipath scenario. The downlink frequency spectrum of the mobile communications operator *Vodafone D2*[6] ranging from 1847.9 MHz to 1852.9 MHz was observed [48]. These measurements were limited to GSM 1800 MHz, as the objective was to gain a proof-of-principle. The results of this campaign can be generalised for other frequency bands of interest in similar scenarios.

3.3.2.1 Measurement Setup

The measurement setup consisted of three synchronised wideband receivers (USRP2), a multi-band directional antenna, and a personal computer, as shown in Fig. 3.7. In this measurement campaign, the reference antenna system was built on a circular ground plane. This allows homogeneous distribution of sectors into 120^o each, by placing metal walls between the antenna elements of the multi-band array. The metal walls divide the space around the antenna array into three equal sectors. The realised gain in Table 3.4 indicates this symmetric distribution of directional patterns. The metal walls were used in this design for mechanical strength as well as for obtaining well shaped patterns with low side-lobe level as shown in Fig. 3.9. The comparative study of this approach of laboratory antenna construction did not reveal significant differences with the one presented in the last section, in terms of the feasibility of the idea. Both the approaches provided orthogonal patterns in different directions and self-similar patterns at different frequency bands (Table 3.6 and 3.5).

The sensing node was placed such that each of the directional patterns d_i, $i = 1, 2, 3$ faced a base-station. The GPS coordinates of the sensing node and base stations are shown in Fig. 3.8. The measurements were performed with a data acquisition rate of 2 snapshots/min. The acquired data were saved on a computer and processed off-line using MATLAB.

[6] Vodafone D2. http://www.vodafone.de.

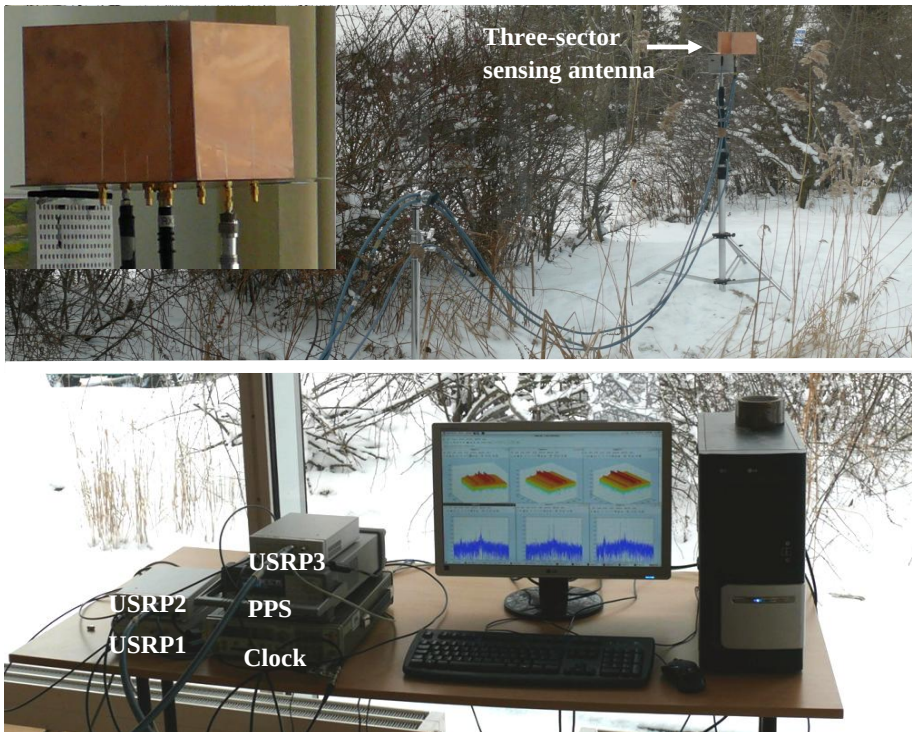

Figure 3.7: Outdoor measurement setup consisting of three synchronised USRPs connected to a three-sector antenna and a personal computer. The clock and pulse per second (PPS) signals were used to synchronise USRPs externally.

3.3.2.2 Analysis Approach

The evaluation of this measurement campaign was different from conventional spectrum sensing, in the sense that the intention was to investigate the directional resources in addition to the frequency resources. In case of directional resources, it is interesting to see if a particular frequency channel is occupied in all directions or only in some directions. It is proposed to determine the *opportunity* available in different directions, and to analyse the *dissimilarity* of the spectrum occupation among them. The choice of the threshold for opportunity analysis is crucial in this case, as it may over- or under-estimate the opportunity. Depending on the signal-to-noise ratio (SNR), the receiver noise level may already be sufficient to provide a directional opportunity. However, for higher SNR, the threshold must be specified higher than the system noise level depending on the side-lobe level of the directional patterns, their beamwidth and mutual orthogonality. In this measurement campaign, the threshold was chosen to be 23 dB below the global maxima over all snapshots.

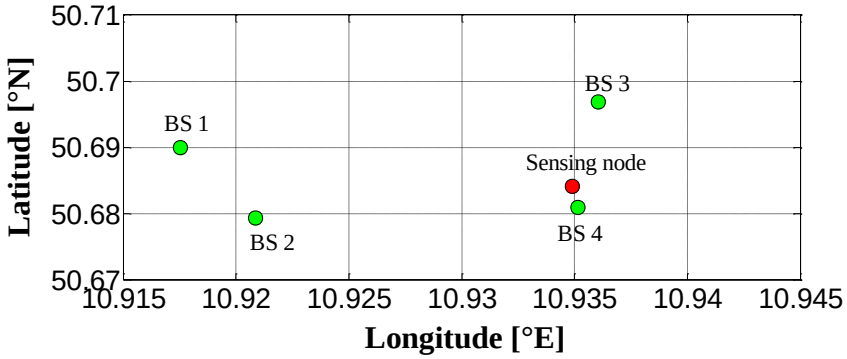

Figure 3.8: GPS coordinates of base-stations (BS) indicated by green dots and sensing node indicated by red dot.

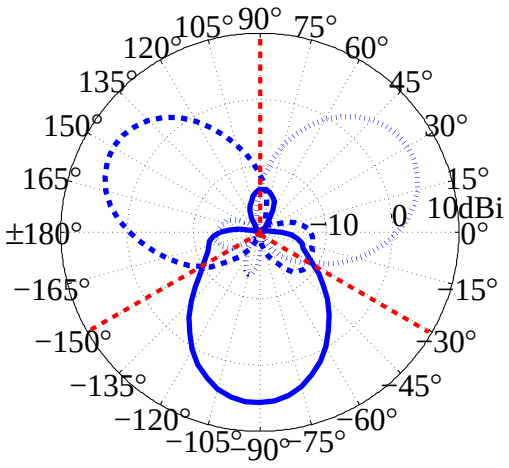

Figure 3.9: Measured directional patterns d_1, d_2, and d_3 of sectors $\#1$, $\#2$, and $\#3$ of the sector antenna with Y-shaped metal walls. The placement of metal walls is shown by dashed red lines. The size of the ground plane was 40 cm.

For both the proposed analyses, the signal presence (1) or absence (0) was determined by comparing the received signal strength with a threshold. The threshold level was set as the minimum possible value that provides different frequency occupancy for different directions. This involved an iterative process with a stepwise decrease in the threshold level until a further decrease provided similar frequency occupancy in different directions.

Table 3.4: Measured gain of the reference antenna with metal walls, over all θ and ϕ in different frequency and direction bins in dBi

Directions	**Frequency bands**		
	f1	**f2**	**f3**
d1	7.27	10.45	9.86
d2	6.74	10.12	9.74
d3	6.87	10.58	10.23

Table 3.5: Orthogonality (eq. 2.27) among directions of the reference antenna (Fig. 3.9), with respect to d_1

Directions	**Frequency bands**		
	f_1	f_2	f_3
d_2	0.0005	0.0009	0.0006
d_3	0.0007	0.0003	0.00002

Table 3.6: Self-similarity among frequency bands (eq. 2.27)of the reference antenna (Fig. 3.9), with respect to f_1

Directions	**Frequency bands**	
	f_2	f_3
d_1	0.637	0.779
d_2	0.552	0.751
d_3	0.572	0.772

3.3.2.3 Opportunity Analysis

The opportunity analysis was performed using energy detection on each of the 200 kHz GSM channels within the 5 MHz downlink frequency band (25 GSM channels). The received signal strength indicator (RSSI) for every GSM channel (CH_{RSSI}) was computed by integrating the power spectral densities (PSD). This involved the interpolation of the acquired data which does not normally provide one sample per Hertz. For example, the measurement campaign provided 160 frequency samples per channel, hence 1250 more samples were added through interpolation.

$$CH_{RSSI} = \sum_{n=1}^{N_{samples}/200kHz} y[n]y[n]^*, \tag{3.1}$$

where $y[n]$ indicates the signal at frequency sample n.

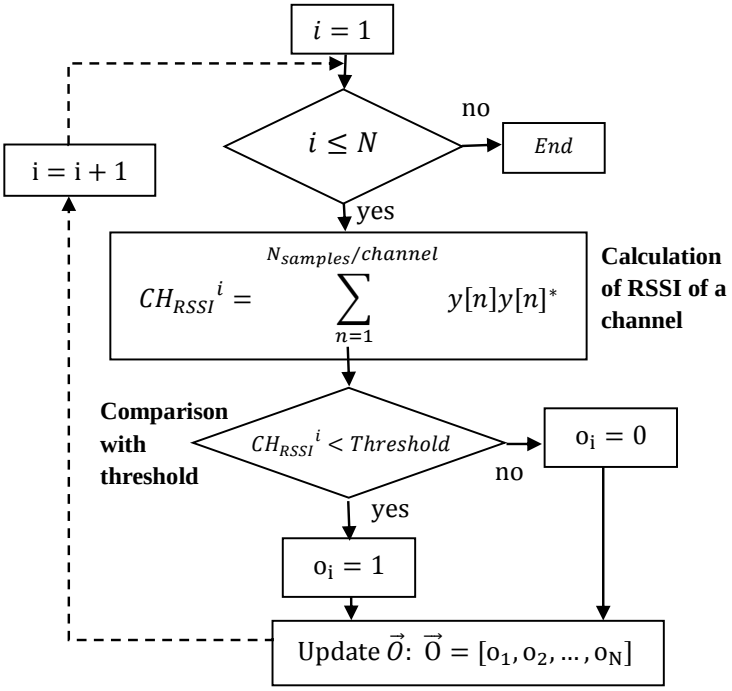

Figure 3.10: Flow chart describing the opportunity analysis, where $y[n]$ is the received signal at frequency sample n and $\{\cdot\}^*$ is the complex conjugate.

CH_{RSSI} is then compared with a threshold to determine the presence (1) or absence (0) of opportunity as described in Fig. 3.10. The process was repeated for every one out of N snapshots, and the decision was stored in vector $\vec{O}$ $= [o_1, o_2, ..., o_N]$. Once the energy detection was performed for all snapshots, the opportunity available for the GSM channel was computed by taking the arithmetic mean over all snapshots

$$P_{opp} = \frac{1}{N} \sum_{i=1}^{N} o_i, \tag{3.2}$$

which can also be expressed as a percentage. The process is repeated for every channel within the band of interest to determine the opportunity available for secondary transmission in every GSM channel.

3.3.2.4 Dissimilarity Analysis

While the opportunity analysis helps in determining the opportunity available in a particular radio resource (frequency, space, etcetera), it is significant to identify those opportunities that are unique. This becomes very important when resources other than frequency are considered. The dissimilarity analysis is an extension of

the opportunity analysis that helps in differentiating between *frequency opportunity* and *directional opportunity*.

The dissimilarity analysis involved the calculation of the *frequency opportunity* for every directional resource. An opportunity was said to be purely *frequency opportunity* ($\vec{D_c}$) when it was available in all directions. A unique *directional opportunity* ($\vec{D_u}$) existed when it was available only in one direction. This can be determined by the logical XOR operation among frequency opportunity in different directions. The off-line processing for the dissimilarity analysis is shown in Fig. 3.11. Furthermore, the arithmetic mean of $\vec{D_c}$ and $\vec{D_u}$ can provide the percentage similarity and dissimilarity respectively.

$$C_{diss} = \frac{1}{N} \sum \vec{D_{diss}}. \tag{3.3}$$

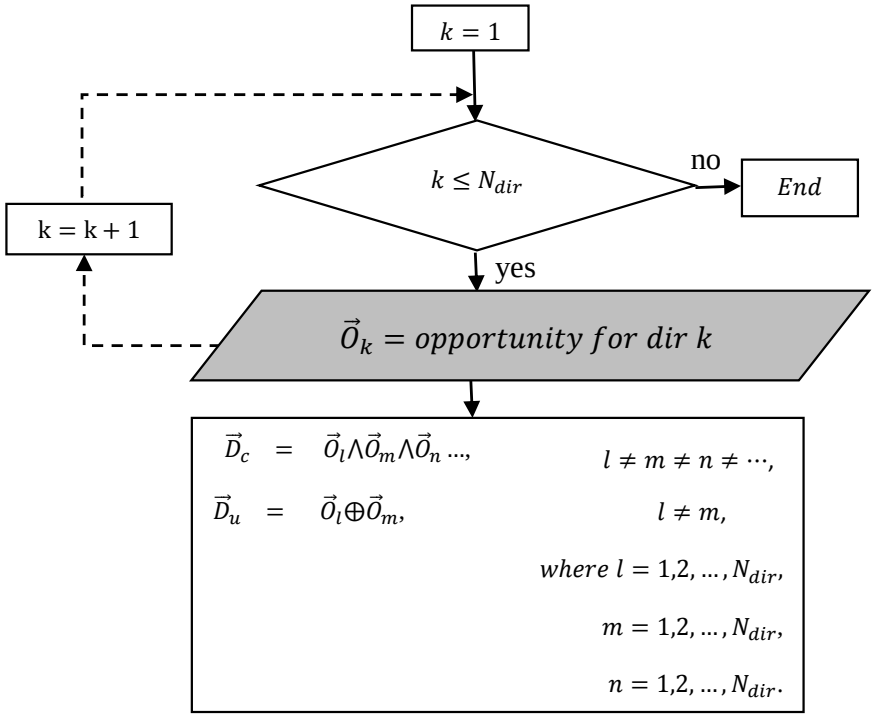

Figure 3.11: Flow chart describing the dissimilarity analysis, the opportunity for all directions is calculated and then compared with others to obtain the common ($\vec{D_c}$) and unique ($\vec{D_u}$) opportunities. $\oplus$ and $\wedge$ represent logical XOR and AND respectively.

3.3.2.5 Measurement Results and Discussion

The measurement was carried out for five hours giving a total of 600 snapshots. Fig. 3.12 shows the channel occupancy for the *Vodafone D2* downlink frequency band for a decision threshold set 23 dB below the maxima over all directions and snapshots. For a lower threshold level, the percentage dissimilarity among sectors decreases dramatically. It can be easily seen that out of 25 available channels, only few were used in the cell where the measurements were performed. Channel $\#5$ and channel $\#9$ show some activity in directions d_2 and d_3 while d_1 is completely free, identifying a unique *directional opportunity*. Channel 4 is sparsely occupied in d_1 while it is highly occupied in d_2 and d_3. Channels 12 and 14 show high occupancy in d_3 while they are partially free in d_1 and d_2. Fig. 3.13 shows the percentage opportunity for all three sectors, and the percentage dissimilarity between pairs d_1 - d_2, d_1 - d_3, and d_2 - d_3. It can be seen in this figure that although many opportunities are available for channel 9 in all three directions (100%, 67%, and 81%), little dissimilarity (32%, 18%, and 22%) exists among directions. However, channel 4 shows a *directional opportunity* in direction d_1 which is dissimilar to d_2 and d_3. The remaining channels may be interpreted accordingly.

Furthermore, the dissimilarity analysis for the evaluation of directional opportunity proves to be worthwhile. As seen in the results in Fig. 3.13, looking at the opportunity in different directions separately may be deceiving. For example, for the case of an omnidirectional opportunity where the results could be overestimated as many directional opportunities, comparison of the directional op-

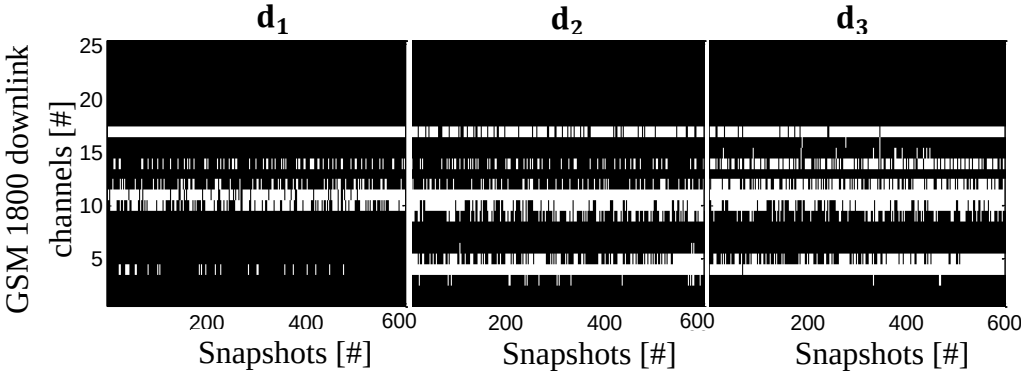

Figure 3.12: Image plots showing the decision about the occupancy of the *Vodafone D2* GSM 1800 MHz downlink channels in different directions d_1, d_2, and d_3 in an outdoor environment. The decision threshold is 23 dB below the maxima over all directions and snapshots. Black colour indicates free channels and white colour indicates occupied channels.

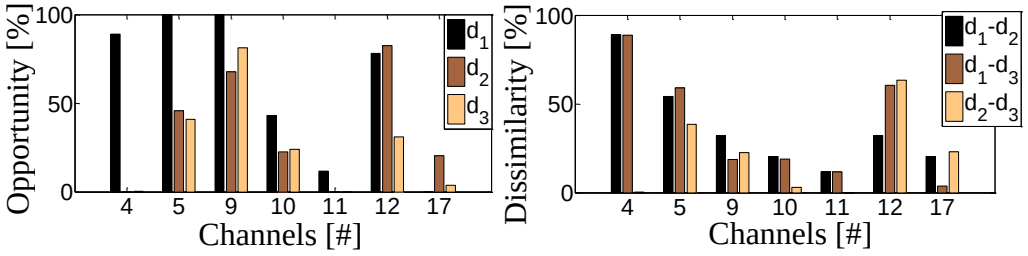

Figure 3.13: Percentage opportunity seen by sector antenna (left) and percentage dissimilarity among directions d_1, d_2, and d_3 (right).

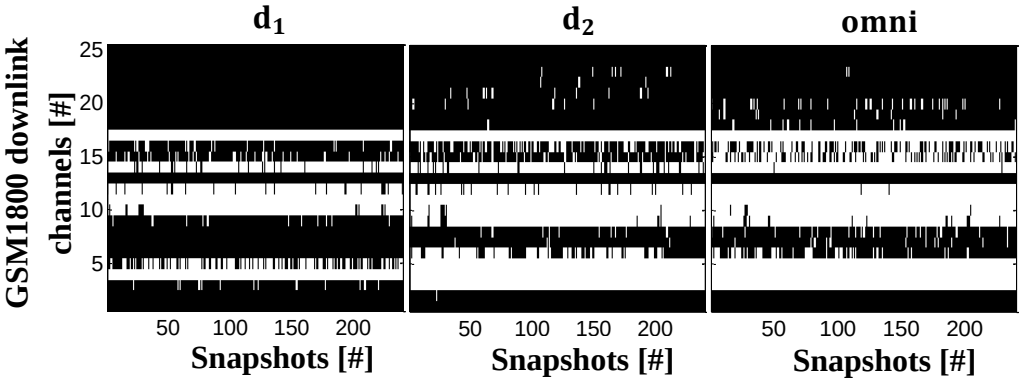

Figure 3.14: Image plots showing the decision about the occupancy of the *Vodafone D2* GSM 1800 MHz downlink channels in directions d_1, d_2 of the sector antenna, and the omni-directional antenna. The decision threshold is 25 dB below the maxima over all directions and snapshots. Black colour indicates free channels and white colour indicates occupied channels.

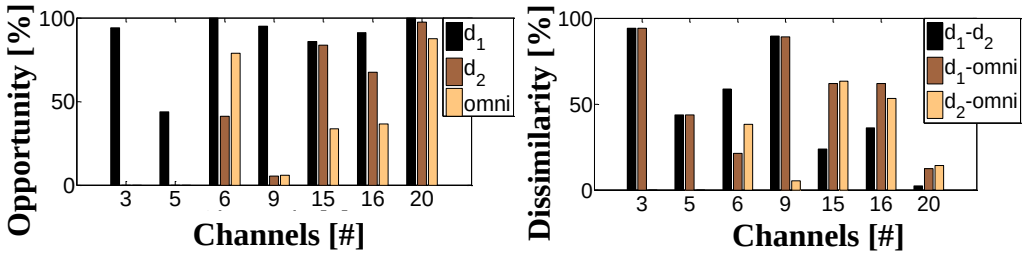

Figure 3.15: Percentage opportunity seen by d_1, d_2 of the sector antenna, and the omni-directional antenna (left), and the percentage dissimilarity among pairs (right).

portunities through dissimilarity analysis unfolds the reality. Hence, dissimilarity analysis is used further for analyses in chapter 6.

Optimal results for dissimilarity are expected at locations where channels from one base station have very low power while very strong signals are received from another base station. The results are expected to be poor if the radiation patterns of the sector antenna are not properly shaped.

Finally, to evaluate the performance of the sector antenna, a comparison with an omni-directional antenna was carried out with a two-hour measurement using an omni-directional monopole antenna and two sectors of the sector antenna (because of the limitation on the number of synchronised receivers). Fig. 3.14 and Fig. 3.15 show the channel occupancy, percentage opportunity, and percentage dissimilarity detected by the two antennas. It is worth mentioning here that a different frequency spectrum occupancy trend is seen in Fig. 3.14 compared to Fig. 3.12 because the measurements were taken at different times of the day.

It can be seen in Fig. 3.15 that the channel occupancy is higher in omnidirectional antennas. The interpretation of this result should be done carefully. The higher gain of sector antenna may result in detecting weak signals which cannot be detected by omni-directional antenna. On the other hand, omni-directional antenna is receiving signals from all directions while sector antenna is receiving with two directional patterns covering a range of 120^0 each. This may result in detecting more signals by omnidirectional antenna compared to sector antenna. As seen in Fig. 3.15, the sector antenna detects more opportunity compared to omni-directional antenna.

3.4 Proof-of-Principle Simulations

Simulations were performed as part of a Master thesis [12] that focused on the evaluation of directional antennas using a ray tracer tool [6]. The city of Ilmenau was modelled in AWR[7] ray tracer and wave propagation was simulated deterministically for the study of directional spectrum sensing and transmission, while GSM base-stations were modelled to simulate primary users. MATLAB was used in the post-processing phase for the statistical evaluation of the results obtained from the ray tracer.

Directional spectrum sensing and transmission were performed using a number of sectors at different locations. The performance of sector antenna was analysed by evaluating spatial opportunity, detection of unknown primary signals, service probability of secondary communications, and the range of communication while sector antenna was used at CR node. The thesis presented the quantitative analysis of spatial opportunities in CR and detection of primary signals using measured and simulated sector antenna patterns. Interested reader is referred to [12, 47].

[7] AWE Communications. http://www.awe-communications.com.

Summary

This chapter presented the design of a reference antenna system, consisting of concentric arrangement of monopole antenna arrays, where the directional patterns were obtained by using metallic/absorber walls between antenna elements. This reference antenna system was used to perform proof-of-principle measurement campaigns. With an antenna array of nine elements, nine degrees-of-freedom (spectral-spatial resources) were obtained at the antenna ports. These consisted of 3 selectable frequency bands, namely GSM 900 MHz, GSM 1800 MHz, and IEEE 802.11b/g, and 3 directions per frequency band. The reference antenna system was capable of separating frequency and directions with a signal-to-interference-ratio of 20 dB, inside an anechoic chamber. An outdoor measurement of such an antenna system was carried out for GSM 1800 MHz at a location surrounded by four base-stations. Power detection was used as the spectrum sensing algorithm. From the results of the measurement campaign, directional opportunity was observed for about 50% of the sensing time for various GSM channels.

4. APPROACHES TO DESIGN COMPACT MULTI-BAND DIRECTIONAL ANTENNAS

An antenna for cognitive radio directional communications should be capable of identifying the frequency band and directional-of-arrival of the incident signals. In addition, it should be capable of supporting secondary communication in the selected frequency band and direction. The state-of-the-art antenna designs for CR achieve this by reconfiguring the aperture of the antenna with switches [21, 60, 62]. Such a reconfigurability disturbs the radiation properties of the antenna.

A novel approach proposed in this thesis suggests to use a combination of multi-band antennas in the form of diversity arrangements or antenna arrays. For example, a multi-band circular array shown in Fig. 4.1 can provide multiple beams at various frequency bands. Such an array can support multiple orthogonal beams which are self-similar at multiple frequency bands. Feed networks can be built for such antenna arrays in order to achieve separate access to all frequency-direction

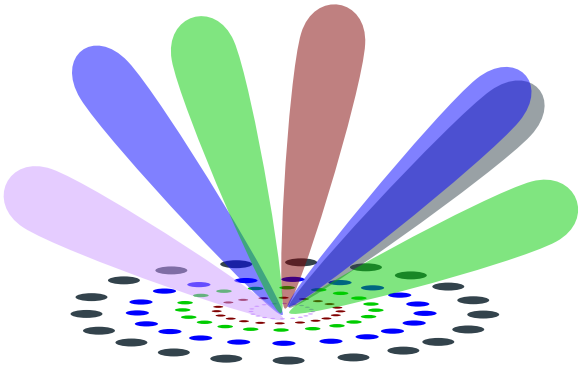

Figure 4.1: Sketch of a generic multi-port multi-band antenna for CR directional communications. The multiple frequency bands are represented in different colours. The coloured beams indicate the directional patterns achievable by the antenna system.

pairs. Such an antenna system can be seen as a filter that provides all frequency and directional degrees-of-freedom simultaneously and separately.

Single-port and multi-port multi-band antennas are studied in this thesis. Single-port antennas provide access to all spectral resources at one port, by embedding more than one resonant structure in a limited space. Multi-port antennas provide separate access to all spectral resources. The frequency and directional resources can be successfully extracted at the antenna system ports using various arrangements of multi-band antennas. Some approaches to design multi-band antenna elements are discussed in section 4.1. The access to directional resources can be provided using antenna arrangements presented in section 4.2, or compact antenna arrays presented in section 4.3. The design of fixed and reconfigurable feed networks for compact multi-band antenna arrays is explained in detail in sub-section 4.3.1 and 4.3.3, respectively.

4.1 Design of Multi-band Antennas

In today's mobile communications, there is an emerging requirement of adding multiple frequency bands in a limited volume antenna. This requirement was initially met with external antennas like monopoles, helix antennas, and their combinations, fed by a single port [7, chapter 3]. At the end of twentieth century, Nokia launched the first internal mobile phone antenna (in 1999). Since then, various multi-band antenna designs have been proposed. These antennas are mainly based on inverted-F (IFA) and planar inverted-F (PIFA) antennas [7, chapter 4]. Recently, *fractal antennas* have been proposed as a candidate for compact multi-band antennas [73]. In the following sub-sections, the design of two different multi-band antennas, namely Siepinski and IFA, are taken into consideration.

4.1.1 Sierpinski Gasket

Sierpinski gasket belongs to the class of fractal antennas. The term *fractal* means broken or irregular fragments. In antenna engineering, this term is used for a class of antennas that possess self-similarity in their structure [4, chapter 33]. In fractal antennas, a certain basic structure is repeated on different length scales, in an effort to reduce the size of the antenna. The geometrical self-similarity results in self-similar radiation properties at design frequencies. Famous fractal structures are the Minkowski loop [74], Sierpinski carpet [32], and Sierpinski gasket [33].

Sierpinski gasket is formed by repeating a triangular structure on different length scales. The scale factor corresponds to the ratio of subsequent resonant frequencies. A Sierpinski gasket with a scale factor 2 is shown in Fig. 4.2. For scale factor other than 2, the gasket is referred to as *perturbed* Sierpinski gasket [34]. In [75], it is shown that the small triangles can be removed during the development of the Sierpinski gasket while preserving the log-periodic behaviour of the

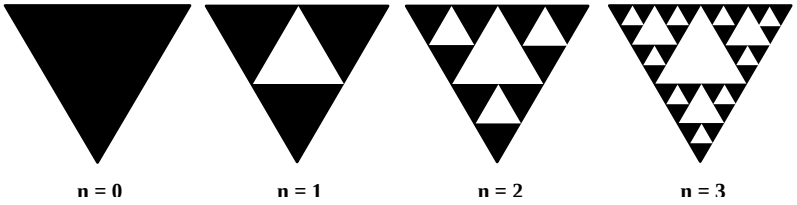

Figure 4.2: The first four stages ($n = 0, 1, 2, 3$) of a conventional Sierpinski gasket construction. The scale factor s for the gasket is 2. Futher explanations are provide in the text.

antenna structure. Such a structure is called *Parany* Siepinski gasket in [34]. It is shown in [34] that a perturbed antenna exhibits poor matching when fed at the apex from the back side of the substrate. Song et al. [75] proposed a microstrip feed to improve the input matching of a perturbed Sierpinski gasket. Since similar structure radiates at multiple design frequencies, the current distribution, and hence the radiation properties at all design frequencies are self-similar.

Sierpinski gasket, with a transmission line feed, was designed using the equation

$$f_r = 0.3\cos(\alpha)\sqrt{\frac{2.5}{\epsilon_r}}\frac{c}{h}s^n, \tag{4.1}$$

where f_r = resonance frequency , α = flare angle (the angle subtended at the apex of the triangle), ϵ_r = relative permittivity of the substrate, h = height of the gasket, s = scale factor (log-periodic) $= \frac{f_{r2}}{f_{r1}}$, n = iteration/stage, and c = speed of light. The proposed design equation, eq. (4.1), is different from the design equation mentioned in [76] by a factor of 2 in the argument α. Hence the proposed Sierpinski gasket results in a smaller antenna as compared to the state-of-the-art. This size reduction is attributed to the transmission line feed, in contrast to a direct feed from the ground plane in [76]. The heights h_n at different stages n of the Sierpinski gasket, for a scaling factor s, can be calculated as:

$$h_n = 0.3\cos(\alpha)\sqrt{\frac{2.5}{\epsilon_r}}\frac{c}{f_{r_n}}s, \tag{4.2}$$

The remaining parameters of the gasket can be found by simple trigonometry,

$$l_{x_n} = 2h_n \tan\left(\frac{\alpha}{2}\right), \tag{4.3}$$

$$l_n = \sqrt{h_n^2 + (l_{x_n}/2)^2}. \tag{4.4}$$

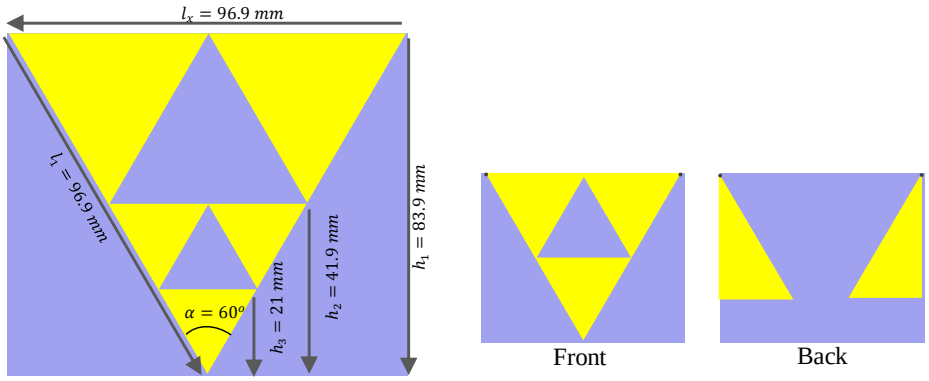

(a) Parany Sierpinski gasket antenna (b) Folded Sierpinski gasket antenna

Figure 4.3: Sketch of (a) conventional and (b) folded 2-stage Parany Sierpinski gasket antenna with scale factor 2. The dimensions of the antenna are shown in panel (a). The yellow colour represents the metal and the blue colour illustrates the substrate.

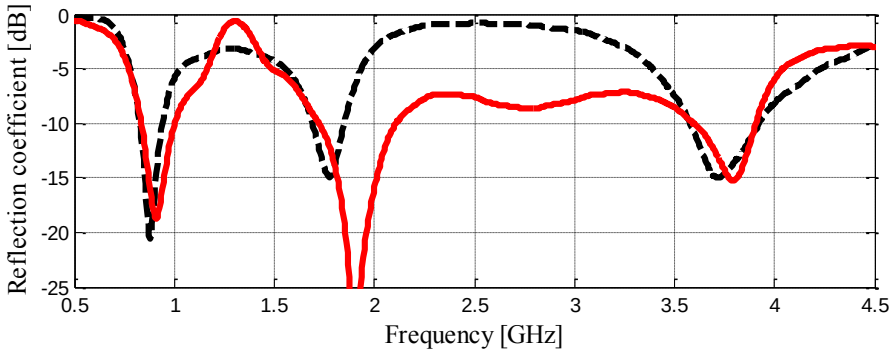

Figure 4.4: Simulated reflection coefficient of folded (solid), and unfolded (dashed) Parany Sierpinki gasket antenna.

where l_{x_n}, and l_n are lengths of the triangle edges (see Fig. 4.3 for details). Hence, the whole structure can be constructed with the knowledge of the desired frequency band, and the flare angle α.

A prototype 2-stage Parany Sierpinski gasket was designed on Rogers RO4003 [1] to provide resonances at 900 MHz, 1800 MHz, and 3600 MHz, respectively. Optimum matching bandwidth was achieved for a flare angle of 60^o. This antenna was fed with a microstrip line at the apex. The resulting dimensions are shown in Fig. 4.3. In order to reduce the size of the gasket, the upper portion of the largest

[1] Rogers Corporation. http://www.rogerscorp.com.

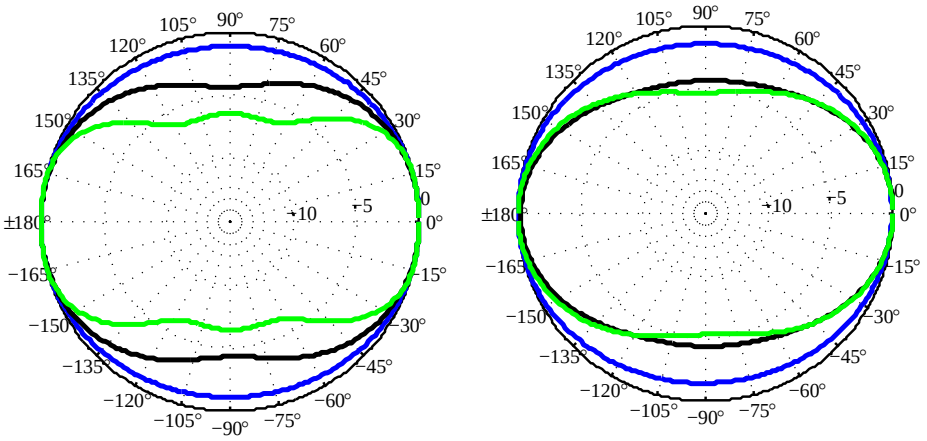

(a) Unfolded Sierpinski (b) Folded Sierpinski

Figure 4.5: Simulated azimuth-cuts of (a) unfolded and (b) folded Sierpinski antenna. The radiation patterns at 940 MHz, 1850 MHz, and 3600 MHz are shown in blue, black, and green colours, respectively.

triangle was folded to the back side of the substrate [43]. A lateral folding of the Sierpinski gasket can also be achieved, as proposed in [75], where the antenna is folded parallel to the ground plane above a certain height, to form an antenna similar to an inverted-F antenna. The proposed folding of Sierpinski gasket to the back of the substrate, however, results in a planar structure. Fig. 4.4 compares the simulation results of an unfolded and folded Sierpinski gasket. These simulations were performed with CST Microwave Studio[2]. It can be seen that the log-periodic behaviour, inherent to the Sierpinski gasket, is preserved after the folding. However, the spectral filtering is not very well-defined, as the antenna shows a wideband behaviour above the second resonance. Nevertheless, the self-similarity in the radiation patterns at the design frequencies, shown in Fig. 4.5, is preserved after folding.

Sierpinski gasket antenna provides all frequency degrees-of-freedom at a single port. The proposed folding of the antenna disturbs the frequency filtering feature of the antenna. The self-similarity feature is, however, preserved. The log-periodic resonances are dependent on the scale factor s, and are achievable at a single-port. In order to overcome these shortcomings, a multi-port multi-band inverted-F antenna design was considered.

[2]CST-Computer Simulation Technology, Bad Nauheimer Str. 19, 64289 Darmstadt, Germany. Available [Online] http://www.cst.com

4.1.2 Multi-port Multi-band Inverted-F Antenna

Inverted-F antenna (IFA) has desirable characteristics: large bandwidth, high efficiency, and omnidirectional radiation pattern [77]. Multiple frequency bands can be added to the antenna, by embedding higher resonances in the ground plane of the IFA designed at the lower frequency. Such a multi-band antenna, shown in Fig. 4.6, was designed for three frequency bands centred at 950 MHz, 1850 MHz, and 2450 MHz, respectively. The multiple bands were fed with a proximity coupled feed on the back side of the substrate. The antenna was designed on Roger RO3010 substrate with relative permittivity of 10.2 and substrate height of 1.27 mm. The antenna was realised over a ground plane of $\lambda_g/4$ at 950 MHz. Independent microstrip transmission lines were used to feed multiple frequency bands using proximity coupled feed ports. Height and width of the short-circuited edges, and the location of the feed has been used to tune the resonant frequencies and bandwidths. The resultant multi-port multi-band antenna is shown in Fig. 4.6. Reflection coefficients at the feed ports, shown in Fig. 4.7, indicate that such a multi-band arrangement ensures good spectral filtering among feed ports. The radiation patterns illustrated in Fig. 4.8, indicate self-similarity among radiation patterns at multiple frequency bands.

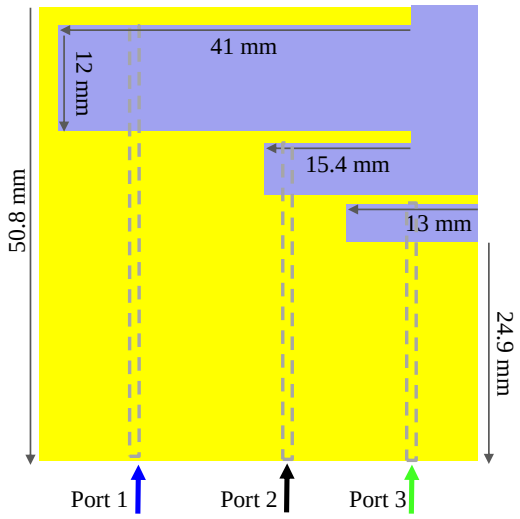

Figure 4.6: Sketch of a multi-port multi-band inverted-F antenna. The dotted lines indicate (three) proximity-coupled feed lines on the back of the substrate. The yellow colour represents the metal and the blue colour illustrates the substrate.

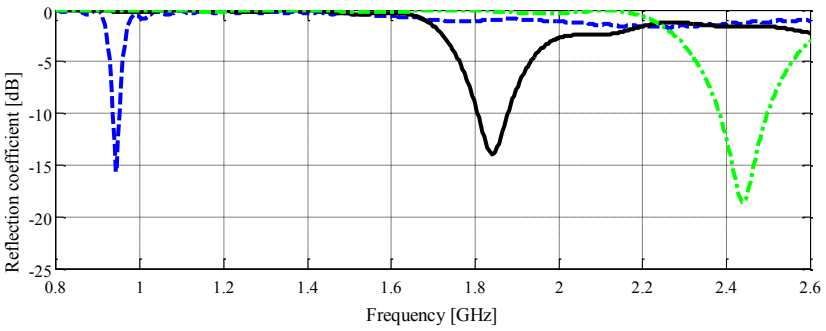

Figure 4.7: Simulated reflection coefficient of a three-port triple-band inverted-F antenna. The blue, black, and green lines indicate the reflection coefficients at the respective ports of Fig. 4.6.

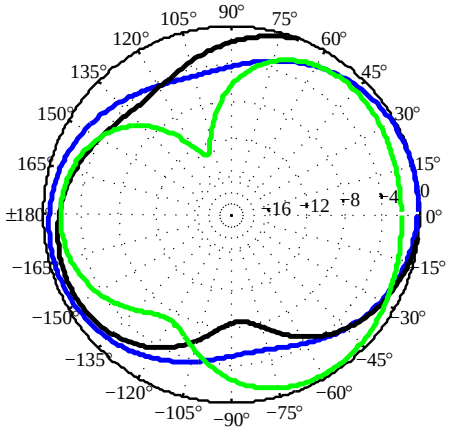

Figure 4.8: Simulated radiation patterns of multi-port multi-band inverted-F antenna (Fig. 4.6). The radiation patterns at 940 MHz, 1850 MHz, and 2450 MHz are shown in blue, black, and green colours, respectively .

4.2 Diversity Arrangements

In order to achieve a number of directional modes in a compact volume, an arrangement of multiple antennas might be considered. These antennas can be arranged such that coupling between the antennas is negligible, which in turn requires that the contributing antenna elements generate orthogonal radiation modes. A class of antennas, known as *diversity antennas*, ensure such orthogonal radiation modes. A conformal and a planar diversity arrangement of antennas are examined in the follwoing sub-sections.

4.2.1 Conformal Arrangement of Wire Antennas

A simple diversity arrangement consists of three orthogonally oriented dipole antennas [35] as shown in Fig. 4.9. The simulation results of this arrangement show that there is virtually no coupling between the antennas. Further diversity modes can be added in such an arrangement by adding three magnetic dipoles (loops) in the same volume. Such an arrangement with six degrees-of-freedom in a small volume, although theoretically possible, introduces practical limitations. The $\lambda/2$ dipoles and the loop radiators (with circumference λ) couple with each other in such an arrangement. The limitations of this arrangement are discussed in detail in doctoral dissertation of J. Weber [10].

The arrangement of dipoles can be extended to multiple bands by adding dipoles resonant at multiple frequency bands within the same volume. One major problem with such an arrangement, however, is to feed the dipoles in the centre. Such an antenna arrangement is referred to as isotropic antenna by Psychogiou et al. [78]. Feed network for this isotropic antenna is proposed in Fig. 4.10.

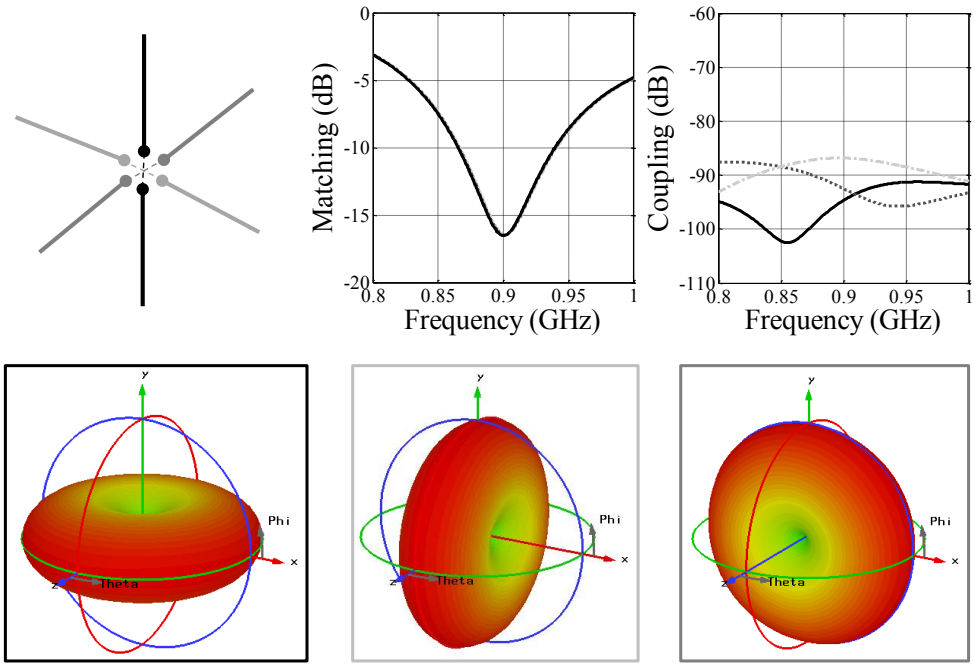

Figure 4.9: Three orthogonally oriented dipole antennas shown with different shades of gray. The respective matching and coupling coefficients are shown on top right. The radiation patterns are shown on the bottom within a border of the respective colour.

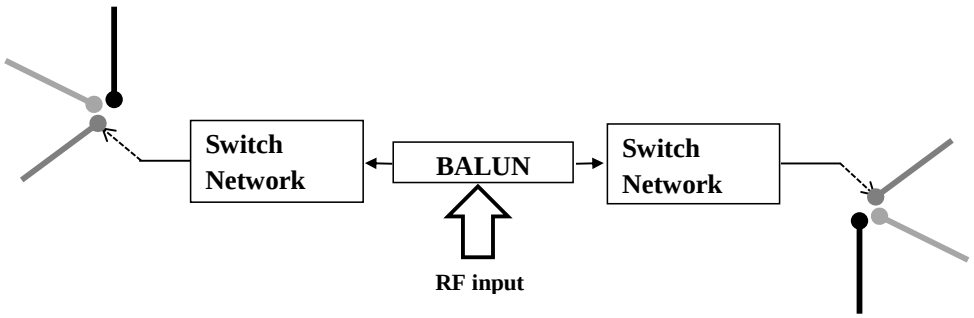

Figure 4.10: Feed network for an isotropic antenna arrangement of dipoles. The network consists of a balun for conversion of coaxial mode to differential mode, required for a dipole, and two switch networks required to simultaneously switch between the respective dipole arms.

The feed network consists of a balanced-unbalanced transformer (balun), and switch networks on both sides in order to switch between three arms of the dipoles on each side of the differential output. The detailed design, and the measurement results of this feed network are presented in section 5.3.

4.2.2 Planar Arrangement

Multi-band antennas, discussed in section 4.1, can be used to form a diversity arrangement capable of providing orthogonal radiation patterns. The multi-band antennas can be orthogonally oriented to form a strictly planar arrangement as shown in Fig. 4.11. This arrangement was simulated for triangular patches to show a proof-of-principle. The basic equation governing an equilateral triangular patch is [36]

$$f_{m,n,l} = \frac{2c}{3a\sqrt{\epsilon_r}}\sqrt{m^2 + mn + n^2}, \tag{4.5}$$

where m, n and l are the mode integers due to electric and magnetic boundary conditions, c is the speed of light in free space, ϵ_r is the dielectric constant, and a is the side-length of the triangle.

Several methods have been suggested for correcting the side-length in order to incorporate the effect of the fringing fields on the sides of the triangular patch. These effects deal with the change of the side-length a and the dielectric constant ϵ_r. For example in [8], it is suggested to calculate the side-length as

$$a_{eff} = a + \frac{h}{\sqrt{\epsilon_r}} \tag{4.6}$$

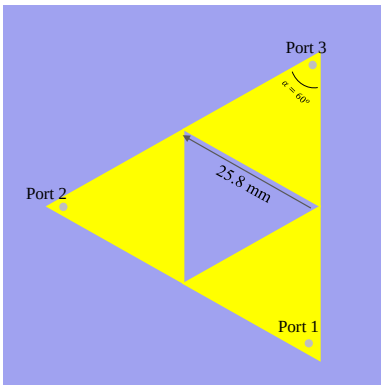

Figure 4.11: Diversity arrangement of three triangular patch antennas, covering a hemisphere with three orthogonal patterns achieved at back-fed ports (gray dots). The yellow colour represents the metal and the blue colour illustrates the substrate.

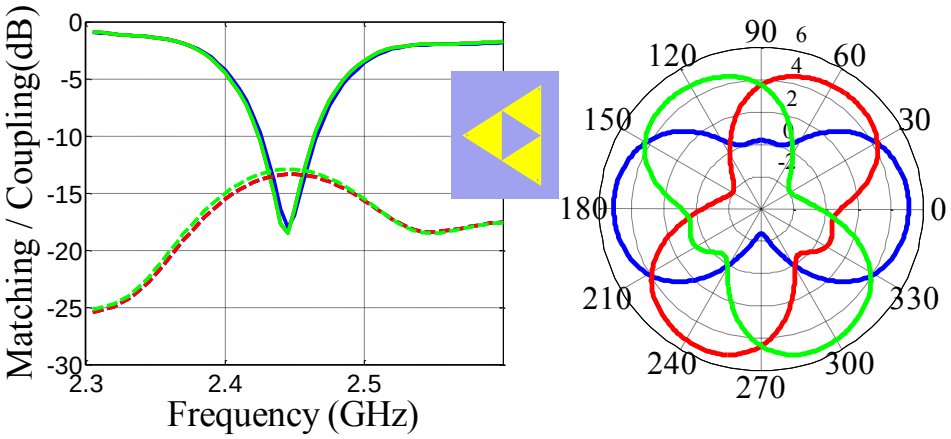

Figure 4.12: Simulation results of the diversity arrangement of three triangular patch antennas. The matching and coupling coefficients (left) indicate a good matching. Azimuth-cuts (right) show that orthogonal patterns are obtained. The results at different ports are represented with different colours.

and

$$\epsilon_{eff} = \frac{1}{2}(\epsilon_r + 1) + \frac{1}{4}(\epsilon_r - 1)\left(1 + \frac{12h}{a}\right)^{\frac{-1}{2}} \tag{4.7}$$

where h is the height of the substrate.

The triangular patch arrangement was simulated for Rogers RO3010 substrate, for a substrate height of 1.27 mm. The arrangemnent is shown in Fig. 4.11. It can be seen in Fig. 4.12 that a planar arrangement provides orthogonal patterns covering a hemisphere. Such planar arrangements can be built with Sierpinski gaskets or IFA to introduce spatial coverage at multiple frequency bands.

4.3 Compact Multi-band Antenna Arrays

Consideration of arrays for CR communications, gives the freedom to control the patterns more rigorously by controlling the array coefficients, and the number of elements in the array. In order to design an elementary antenna system with individual access to frequency degrees-of-freedom, concentric antenna arrays res-

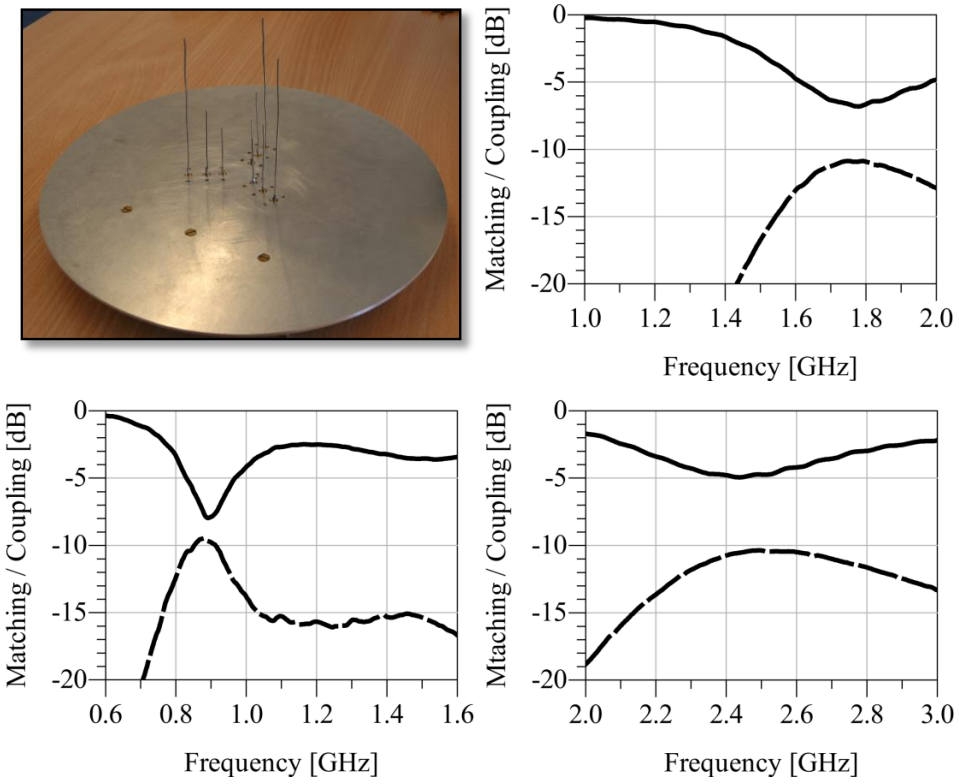

Figure 4.13: Photograph of a compact multi-port multi-band antenna array operating at three frequency bands GSM 900 MHz, GSM 1800 MHz, and IEEE 802.11 b/g (top left). The measured matching and coupling coefficients of the concentric arrays are represented with solid and dashed lines, respectively. The diameter of the ground plane is 22 cm.

onant at three selectable frequency bands (GSM 900 MHz, GSM 1800 MHz, and IEEE 802.11b/g) are proposed for the reference antenna design in section 3.2. However, a $\lambda/2$ array arrangement, as used in the proof-of-principle measurements, turns out to be quite large in terms of its physical size. This makes $\lambda/2$ array impractical for small platforms. An electrically small antenna array was designed by reducing the inter-element spacing to $\lambda/6$. This arrangement was realised on an aluminium ground plane of diameter 22 cm (0.6λ) as shown in Fig. 4.13. Monopoles of length 0.223λ were realised with silver-plated copper wires. The compactness introduced in the antenna array results in mutual coupling between array elements as discussed in chapter 2. The mutual coupling can be reduced by the excitation of orthogonal beam patterns with the help of a decoupling and matching network. The design concept of such a feed network for n-band array is shown in Fig. 4.14. The feed network provides m directional patterns at n frequency bands. A total of mxn degrees-of-freedom are obtained at the system ports. The patterns are self-similar at different frequency bands, and orthogonal in different directions.

The compact multi-band antenna array together with a multi-port multi-band feed network is called *spectrum- and space-selective cognitive antenna system*. For the multi-band array shown in Fig. 4.13, three separate feed networks were built on the same substrate.

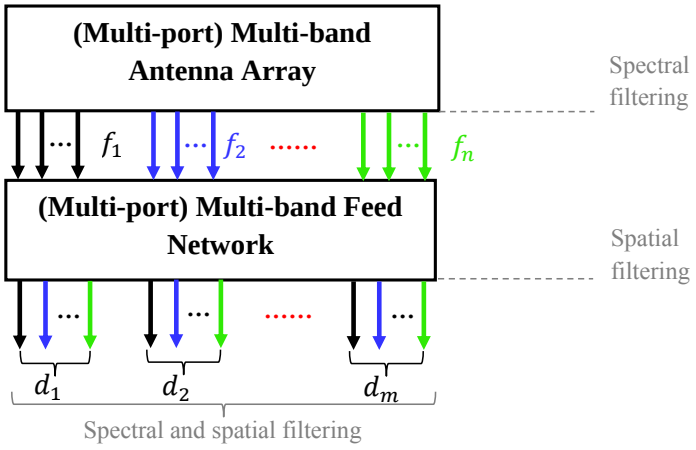

Figure 4.14: Generic block diagram of a multi-port multi-band directional antenna system with n frequency resources ($[f_1, f_2, ...f_n]$), and m directional resources ($[d_1, d_2, ...d_m]$). Spectral filtering is obtained at the array ports, and spatial filtering is achieved at the network (system) ports.

4.3.1 Feed Network Design

The feed network was designed by using the design equations proposed in [10]. J. Weber achieved the network reduction using minmum search algorithm, and implemented the network with quasi-lumped elements. However, a slighty different procedure was used to design the feed network during this work. The feed network was reduced using the sensitivity analysis in Agilent ADS[3], and the network was realised with off-the-shelf lumped components. This allows a small size for the feed network, which is particularly important for small antenna systems. As an example, a feed network for the compact concentric monopole array, Fig. 4.13, was designed.

The feed network for the innermost, highest frequency array, was designed first. The networks for lower frequency bands were then added in the same layout. The addition was done in a concentric way, similar to the design of the array. Output ports of the feed network were designed such that it could be directly connected behind the antenna array.

The feed network for the innermost 3-element monopole array is explained here in detail. The measured S-parameters of the array are shown in Fig. 4.13. The S-matrix was used to obtain the design equations for the feed network using the procedure in 2.2.5. The antenna admittance matrix of this array at 2.45 GHz was

$$\tilde{Y_a} = \begin{bmatrix} 0.0056 - 0.0125j & 0.0019 + 0.0062j & 0.0019 + 0.0064j \\ 0.0019 + 0.0062j & 0.0053 - 0.0109j & 0.0019 + 0.0059j \\ 0.0019 + 0.0064j & 0.0019 + 0.0059j & 0.0052 - 0.0110j \end{bmatrix}. \quad (4.8)$$

The excitation modes were selected such that they pointed in three orthogonal directions, with minimum back-lobe level. The patterns of antenna elements were super-imposed with various current vectors to obtain the desired current transfer matrix. The desired matrix was chosen to be

$$\tilde{T_a} = \begin{bmatrix} 0.81e^{130^\circ} & 0.41e^{-150^\circ} & 0.41e^{-150^\circ} \\ 0.41e^{-150^\circ} & 0.81e^{130^\circ} & 0.41e^{-150^\circ} \\ 0.41e^{-150^\circ} & 0.41e^{-150^\circ} & 0.81e^{130^\circ} \end{bmatrix}. \quad (4.9)$$

Such a current transfer matrix excites the radiation modes shown in Fig. 4.15. The side-lobe level for all modes is well below -10 dB. The power excited by all three modes is equal but it is radiated in three orthogonal directions.

[3] Agilent Advanced Design System. Herrenberger Str. 130, 71034 Böblingen, Germany.

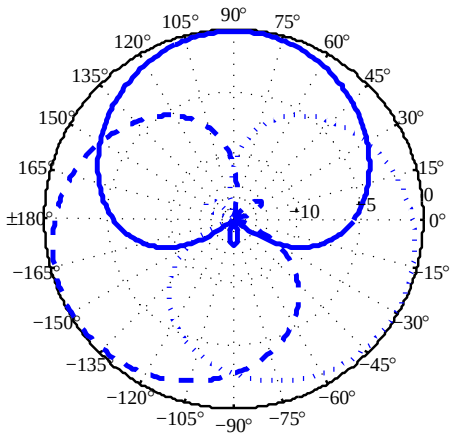

Figure 4.15: Azimuth-cuts of the desired radiation modes for the multi-port multi-band directional antenna system. The three directional patterns are represnted with different colours.

The voltage transfer matrix for the desired excitation modes was calculated using eq. (2.29) as

$$\tilde{T}_u = \begin{bmatrix} 1.7018e^{140.8614\circ} & 0.6920e^{-90.8176\circ} & 1.0169e^{-117.2268\circ} \\ 0.2276e^{-152.4616\circ} & 0.9645e^{-105.1420\circ} & 1.9148e^{68.3903\circ} \\ 0.4970e^{-154.0300\circ} & 2.0724e^{100.6497\circ} & 0.5015e^{133.7460\circ} \end{bmatrix}. \quad (4.10)$$

The network admittance matrix, $\tilde{Y}_n$, was calculated using eq. (2.30), for a lossless DMN. Such a network matrix returns a large number of components depending on the number of elements in the array, $m(2m+1)$ for an m element array. A three element antenna array requires 21 lumped elements to achieve decoupling and matching. The resultant feed network takes the form shown in Fig. 4.16. The resultant scattering parameters of the antenna array with and without the feed network are shown in Fig. 4.17.

4.3.1.1 Feed Network Reduction

The resultant network (Fig. 4.16) is hard to imagine on a single layer without cross-overs. Nevertheless, it is possible to reduce the number of elements by removing the insensitive elements.

The feed network reduction was achieved by following an iterative procedure, shown in Fig. 4.18. After the calculation of the network elements, a circuit diagram of the feed network was built in ADS. The insensitive elements were recognised through statistical analysis. These elements were removed from the network and the remaining elements were optimised for the design goals. The process was

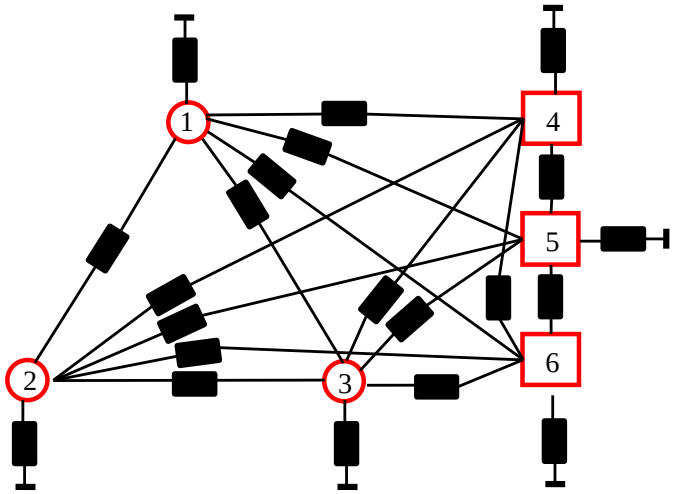

Figure 4.16: Circuit diagram of the decoupling and matching network IEEE 802.11 b/g compact array, obtained from eq. (2.30). The boxes represent the output ports, and the circles correspond to the input ports of the network.

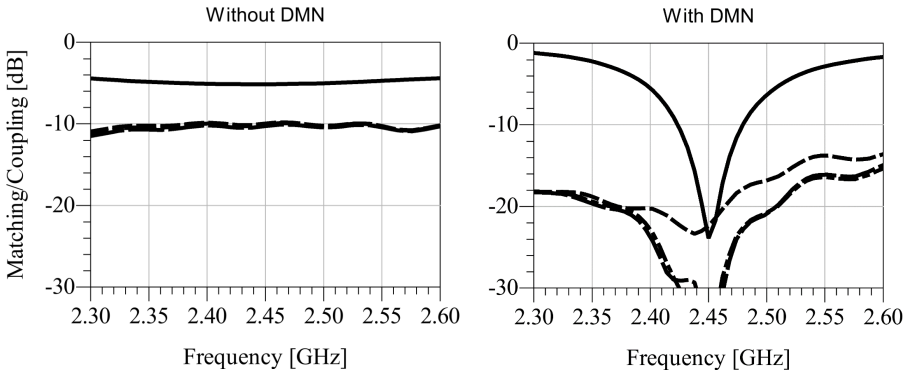

Figure 4.17: Matching (solid) and decoupling (dashed) of the IEEE 802.11 b/g compact array of the proposed antenna system, Fig. 4.13, without DMN (left) and with 21 element DMN (right).

repeated until further reduction resulted in unrecoverable results. The optimisation goals included 1) a high bandwidth for decoupling and matching at the input ports of the network (6 goals), and 2) excitation of the required modes (3 goals per mode, returning a total of 9 goals). Using this iterative process, a reduction of 67% was achieved by reducing the number of elements from 21 to 7 for the 3-element array.

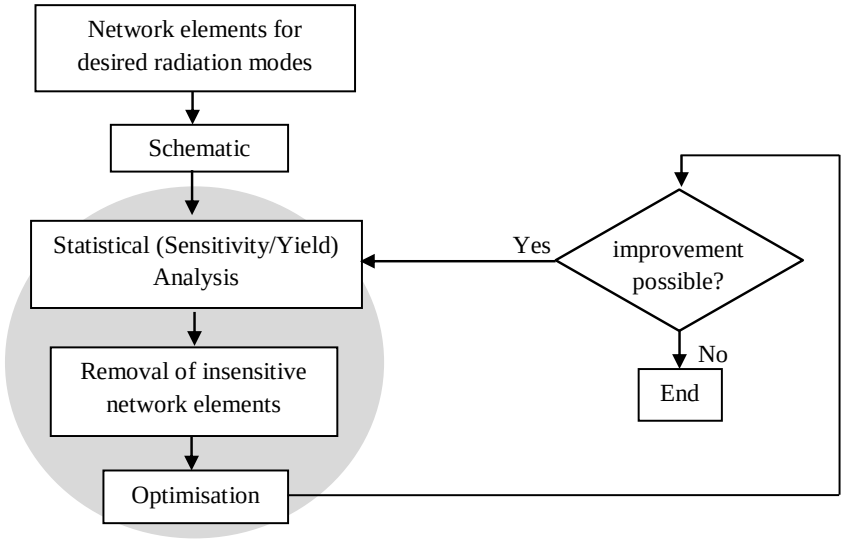

Figure 4.18: Iterative procedure for reduction in the number of lumped elements in the feed network.

element	value
L13	1.5 nH
C14	3.0 pF
L15	1.3 nH
L23	2.2 nH
L25	1.5 nH
C26	2.4 pF
C35	1.5 pF

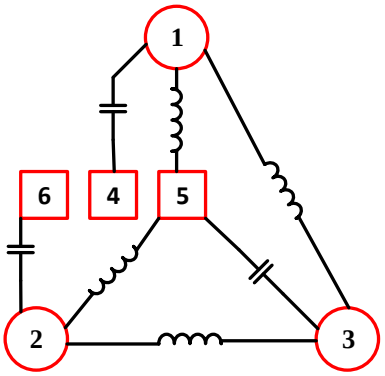

Figure 4.19: Decoupling and matching network for a single-band compact array. The square boxes indicate the input ports of the network, and circles represent the output ports of the network (antenna ports). The right hand table summarises the respective network elements.

It was further observed that once the amplitudes and phases of the excitation modes were set by the design equation, they were not heavily affected by the optimisation process. Hence the number of goals could be reduced to 6, namely the goals for matching and decoupling. The resultant feed network with reduced number of elements is shown in Fig. 4.19.

4.3.1.2 Network Realisation

Once the number and values of the lumped components are finalised, the network could be realised with distributed, quasi-lumped, or lumped reactive components. Compared to [10], lumped components were chosen for realisation of the feed network. Using lumped elements, a multi-band feed network for the compact antenna system, Fig. 4.13, could be realised on a substrate as small as 30 mm $\times$ 30 mm (without the transmission lines to feed the antennas). SMD components of size 0402 (0.4 mm $\times$ 0.2 mm) were used for the realisation of the feed network. At the same time, it must be noted that the system performance is highly dependent on the tolerance ranges and quality factor of the lumped components. Moreover, commercial lumped components are not available in arbitrary values. Hence, the design needs to be fixed for certain fixed values. This could result in deteriorated network performance for highly compact arrays, implemented with medium tolerance lumped elements.

The tolerance of the lumped elements needs to be low enough to ensure a high yield. The required tolerances can be foreseen through Monte Carlo simulations in ADS. The tolerances of the lumped elements can be set. Through Monte Carlo simulations, all element values are randomly changed within their tolerance ranges, and deviation from the design goals can be studied. For example, for the feed network of IEEE 802.11b/g compact array, Monte Carlo simulations for 10% and 1% tolerance are shown in Table 4.1 and 4.2. The design goals were to achieve decoupling and matching at 2450 MHz with a bandwidth of at least 30 MHz. Mean and standard deviation of the centre frequency/bandwidth from the desired centre frequency and bandwidth were calculated. The percentage realisations when the circuit failed to deliver the desired performance are also summarised.

Table 4.1: Results of Monte Carlo simulations for the feed network realised with lumped elements of 10% tolerance. Further explanations are provided in the text.

Goal	Bandwidth [MHz] mean (std)	Centre frequency [MHz] mean (std)	Failure ($\%$)
S11	53.9 (8.6)	2470 (15.2)	0
S12	44.3 (41.2)	2444 (5.5)	37
S13	46.1 (5.7)	2454 (19.2)	0
S22	56.1 (28.6)	2455 (9.0)	3.4
S23	54.7 (11.2)	2441 (18.9)	0
S33	78.8 (52.6)	2451 (88.0)	17.9

Table 4.2: Results of Monte Carlo simulations for the feed network realised with lumped elements of 1% tolerance. Further explanations are provided in the text.

Goal	Bandwidth [MHz] mean (std)	Centre frequency [MHz] mean (std)	Failure ($\%$)
S11	52.8 (1.0)	2466 (1.2)	0
S12	45.2 (6.2)	2442 (0.4)	0
S13	42.7 (0.7)	2451 (2.0)	0
S22	51.4 (2.6)	2452 (0.9)	0
S23	46.9 (1.1)	2437 (2.1)	0
S33	119.8 (4.0)	2456 (1.2)	0

Table 4.1 shows that for 10% tolerance, the matching frequency of $S33$ has a standard deviation of 88 MHz around mean value of 2451 MHz. The mean centre frequency for all other design goals is spread over 20 MHz. The bandwidth of the antenna system is above 40 MHz, and varies with a standard deviation of up to 52 MHz for $S33$. Moreover, the feed network fails to achieve matching and decoupling at the desired centre frequency and bandwidth for 37% iterations for $S12$. When the tolerance for lumped elements was reduced to as low as 1%, the results in Table 4.2 indicate that the desired goals were achieved without any failure. This implies that lumped elements with very low tolerances are required to realise feed networks with off-the-shelf capacitors and inductors.

Inductor series LQW and capacitor series GRM15 from Murata[4] were used for realisation of the networks during the course of this research. The element tolerances for capacitors were as low as 0.1 pF and varied up to 2 $\%$. The inductor tolerances varied from 0.1 nH to 2 $\%$.

4.3.2 Multi-port Multi-band Feed Network

A feed network for the triple-band compact array, shown in Fig. 4.13, was designed by combining the feed networks for individual frequency bands. Port-level access to all nine degrees-of-freedom was preserved at output ports of the feed network. The conceptual diagram of the antenna system is shown in Fig. 4.20. The scattering (S), impedance (Z), and admittance (Y) matrices at the antenna and the system plane are also summarised in the figure.

The feed networks were designed using the procedure explained in section 4.3.1. Fig. 4.21 shows the resultant network of 21 elements for the three frequency

[4]Murata Elektronik GmbH, Holbeinstrasse 23, 90441 Nürnberg, Germany. [Online] http: www.murata.com

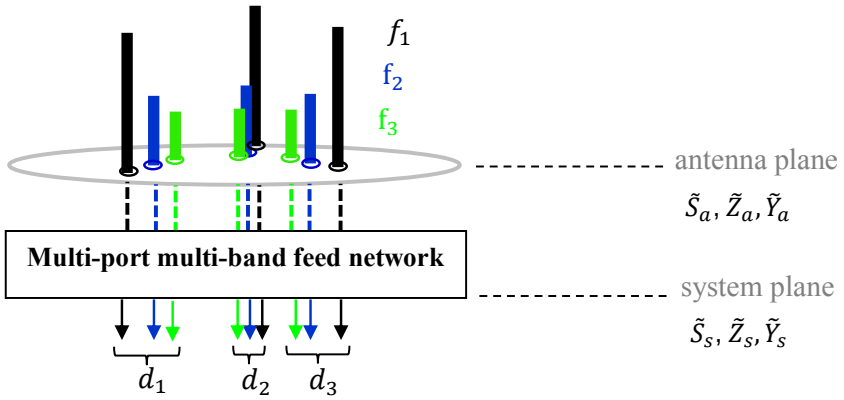

Figure 4.20: Design concept of compact antenna system consisting of nine-port triple-band antenna (Fig. 4.13), and a nine-port triple-band feed network. The arrays at different frequency bands are represented with different colours. The S-, Z-, and Y-matrix at the antenna and system planes are summarised on the right-hand-side.

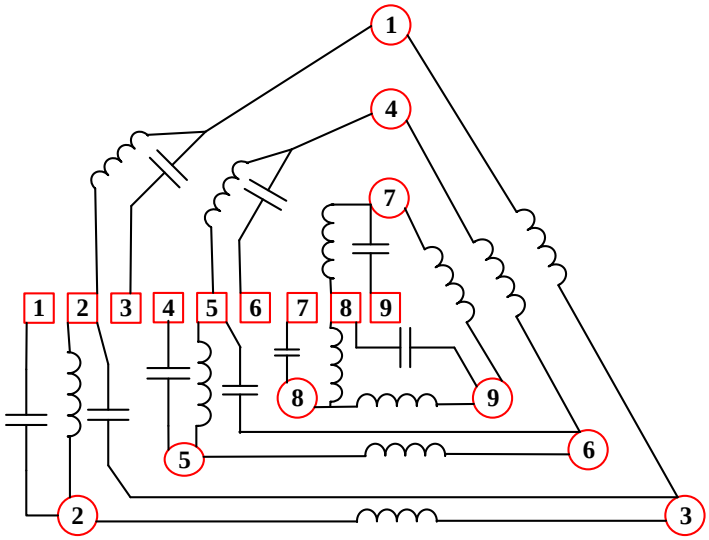

Figure 4.21: Circuit diagram of the feed network for a compact nine-port triple-band antenna system. The feed network consists of 21 network elements (7 for each frequency band). The circles represent the input ports of the network (antenna) and the squares represent the output ports of the feed network.

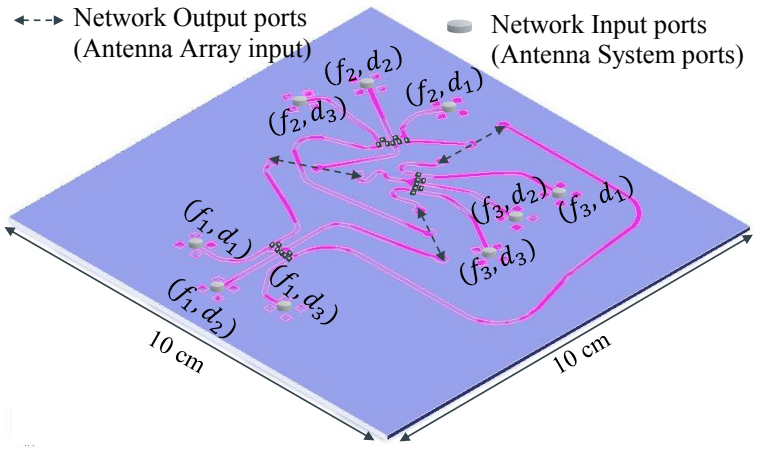

Figure 4.22: Layout of the nine-port triple-band feed network. Transmission lines are added to the feed networks in order to connect directly behind the concentric antenna array (Fig. 4.13).

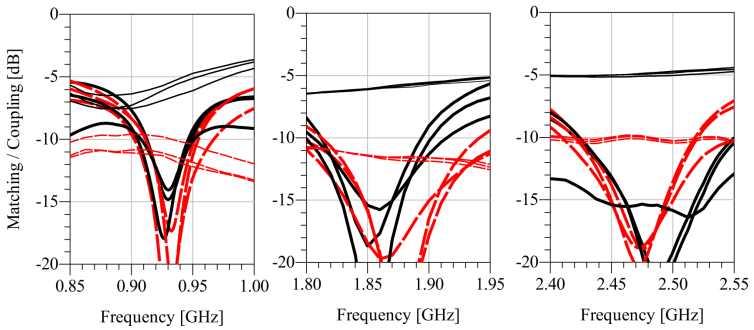

Figure 4.23: Matching (solid) and decoupling (dashed) of the proposed antenna array, Fig. 4.13, with (thick) and without (thin) the feed network.

bands. The network was realised on Rogers RO3010 substrate with effective permittivity of 10.2, and substrate height of 1.27 mm. All three feed networks were realised on the same substrate, and the feed lines were added such that all nine antenna elements of the multi-band array could be fed directly behind the array. The resultant layout of the feed network, with the lumped elements, is shown in Fig. 4.22.

The simulation results of the antenna system, with and without the feed network, are shown in Fig. 4.23. It can be seen that such a feed network can provide matching and decoupling at the antenna system ports. In consequence, such a design accomplishes spectral and directional filtering. Such multi-port feed networks can

also be realised directly behind the ground plane of planar antenna arrays using multi-layer substrates.

4.3.3 Reconfigurable Feed Network

Feed network of compact antenna arrays can be made reconfigurable by using variable lumped elements [79, 80]. For example, varactor diodes can be used to realise variable capacitors. Such reconfigurable feed networks can provide tuning between widely separated frequency bands, for example, GSM 900 MHz, GSM 1800 MHz, and IEEE802.11b/g in the proposed design. Furthermore, feed network for a single-band array can be made tunable to provide various frequency states within a single frequency band, for example, for each one of the arrays in Fig. 4.23. The former can be helpful for single-port multi-band arrays where such a reconfigurable feed network can act as a frequency filter behind the antenna array. The latter is appropriate for single-band antenna arrays. Reconfigurable feed network designs were explored for the multi-band compact antenna array (Fig. 4.13). The results can, however, be generalised for various antenna types and array arrangements.

Contrary to the conventional antenna designs for CR, reconfigurability behind the radiating aperture of the antenna does not disturb the radiation properties of the antenna. The design procedure, and simulation results for the reconfigurable (switchable and tunable) feed networks are presented in the following sections. The design goals for such reconfigurable feed networks are to obtain: 1) low coupling (transmission coefficients between input ports), and reflection (at the input ports), and 2) wide operational bandwidth of the feed network.

4.3.3.1 Switchable Feed Network

A switchable feed network operates at discrete frequency bands. The design of such a feed network for the multi-port multi-band compact array is presented as a proof-of-principle. The feed network for this array can be realised with three switchable states. In order to feed the multi-port antenna array, a switch network must be employed behind the array as shown in Fig. 4.24. The network was designed in cooperation with a visiting research fellow, Evgenia Zamaschaeva, and the simulation results are published in [44].

The operational frequency of the feed network was reconfigured through discrete variation of capacitors. Voltage-controlled varactor diodes were used to realise variable capacitors. The capacitance of a varactor diode is controlled through the reverse-bias control voltage. Varactor diodes have already been used for reconfiguration of antennas [37, 38], filters [39], and feed networks [40].

The operational frequency of the feed network was reconfigured using a set of control voltages. In order to design such a reconfigurable feed network, the in-

dividual networks were optimised such that they led to several fixed components and a few variable capacitors. The values of the lumped elements for this regime were optimised such that: 1) low coupling and reflection were obtained within the operational frequency bands, 2) the values of the network elements (capacitance of varactor diodes and inductance) complied with commercially available components, and 3) all inductors had fixed values.

A switchable feed network was designed for the multi-band array with $\lambda/2$ inter-element spacing. The equivalent circuit of the resultant feed network is shown in Fig. 4.25. Ports 1, 2, and 3 represent input ports of the network. Ports 4, 5, and 6 are the output ports connected to the respective antenna arrays through switch network. Varactor diodes with low series resistance, SMV2020 from skyworks[5], were used as variable capacitors. All varactor diodes (tunable capacitors in Fig. 4.25) were adjusted simultaneously, to change the operational frequency band. S-parameters of the fixed components, and equivalent circuits of the varactor diodes (supplied by the manufacturer) were used during the design process. The equivalent circuit of the feed network has a complicated structure with numerous line crossings. Due to this reason, a double-sided printed circuit board was designed on Rogers RO3010 with SMD components. The size of the designed switchable feed network was approximately 20 mm x 20 mm.

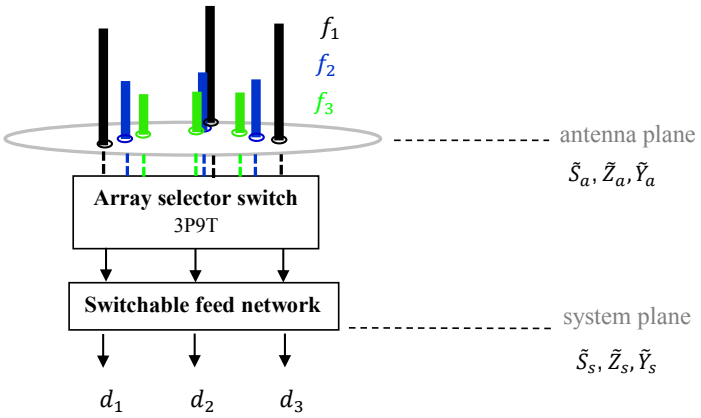

Figure 4.24: Design concept of a switchable feed network. The switch network selects an antenna array, and the feed network switches to the respective frequency state.

[5]Skyworks Solutions, Inc. [Online] http://www.skyworksinc.com/

4.3.3.2 Tunable Feed Network

A tunable feed network can be designed to reconfigure to a number of frequency states within a specific frequency band. Tunable feed networks were designed for the multi-port multi-band compact antenna array during a Master thesis [13]. A tunable feed network for the outermost GSM 900 MHz array of Fig. 4.13 is presented here as an example. The 10 dB bandwidth of this array, resonant at GSM 900 MHz frequency band, with the fixed DMN was 30 MHz as shown in Fig. 4.23. A tunable feed network was designed for this array to provide frequency states covering a bandwith of about 90 MHz. The feed network elements (eq. (2.30)) were obtained for six frequency states, separated by 30 MHz, within GSM 900 MHz frequency band. The elements were then reduced using the procedure explained in Fig. 4.18. The inductors were fixed for all states using a stepwise procedure, and capacitors were allowed to vary.

The tunable feed network, with the biasing circuit and varactor diode, is shown in Fig. 4.26. The network design was accomplished with three reconfigurable elements, realised with varactor diodes. The biasing circuit of the varactor diode consisted of 1000 pF DC block capacitor to block DC current flowing to RF ports, and RF chokes of 220 nH to eliminate biasing lines from the RF path. SMV1283-011LF, varactor diode from Skyworks, were used to realise variable capacitors.

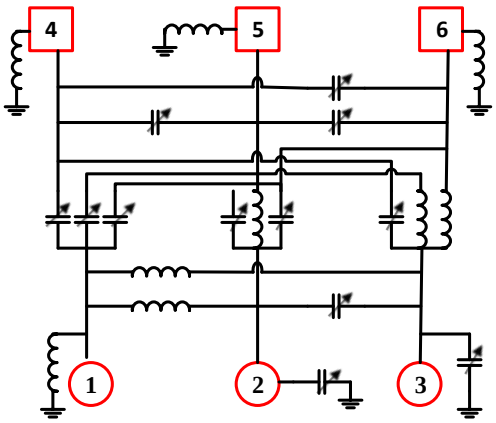

(a) Schematic

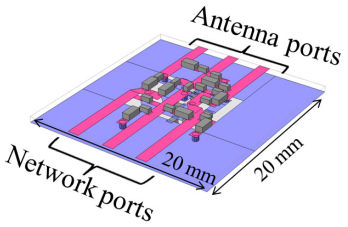

(b) Layout: blue, pink and grey colour represent ground, conductor, and components, respectively [44]

Figure 4.25: Reconfigurable feed network for a triple-band antenna array with $\lambda/2$ inter-element spacing. (a) Circuit diagram, and (b) layout. The variable capacitors are realised with voltage-controlled varactor diodes.

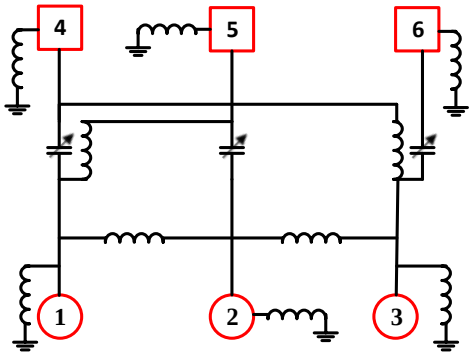

(a) Circuit diagram

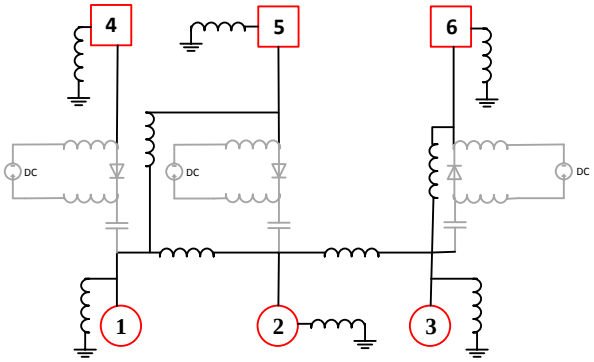

(b) Circuit diagram with varactor diode and biasing circuit

Figure 4.26: Equivalent circuit of the tunable feed network with (a) variable capacitors, and (b) varactor diodes and the biasing circuit.

The equivalent circuit of SMV1283 is shown in Fig. 4.27. The realisation of the network on a substrate alongwith all the circuit elements and fixed inductor values is shown in Fig. 4.28. The The tuning range of the varactor diode is from 0.517 to 14.228 pF for a reverse bias voltage of 26 to 0 V, respectively. The capacitance range required for the reconfigurable feed network was from 1 to 12 pF. The bias voltages required to achieve the simulation results shown in Fig. 4.29 are summarised in Table 5.6.

The simulation results of the feed network with the biasing circuit of the varactor diode is shown in Fig. 4.29. It shows that the tuning range could be successfully increased from 890 - 960 MHz. Each state covered approximately 20 MHz. The

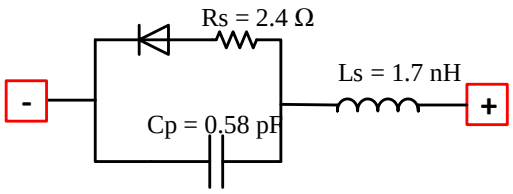

Figure 4.27: Circuit diagram of Skyworks SMV1283 varactor diode.

element	value
L11	9 nH
L13	5.1 nH
L15	15 nH
L22	10 nH
L23	5.1 nH
L25	5.8 nH
L33	10 nH
L44	7.5 nH
L55	2.5 nH
L66	7.5 nH

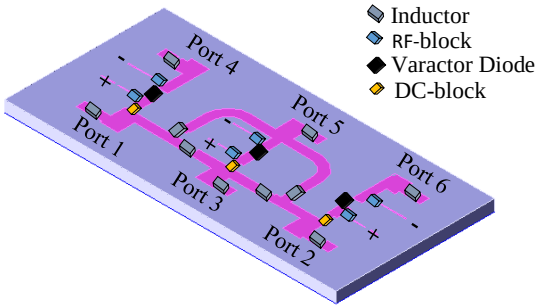

Figure 4.28: Layout of the tunable feed network with the biasing circuit, designed for GSM 900 MHz frequency band. The fixed elements of the network, cf. Fig. 4.26, are summarised in the table.

middle four states in Fig. 4.29 can be alternatively chosen for CR sensing and secondary communication. The outer two states (#1 and #6) are shown to highlight the frontier of reconfigurability.

Compared to the tunable network over widely separated frequency bands in the switchable regime, a tunable feed network for closely separated frequencies in a single frequency band required less network elements (less variable capacitors). Hence, the operating states could be tuned using low number of control voltages. Moreover, such reconfigurable feed networks can be built for a variety of multi-band antenna arrays. Various commercially available varactor diodes with diverse capacitance ranges, can be used for relisation of reconfigurable networks. Such networks also provide possibility for post-production tuning.

Table 4.3: Biasing voltage for the reconfigurable states of the feed network.

Voltage (V)	State					
	State 1	State 2	State 3	State 4	State 5	State 6
V_1	1.6	4.3	5	5.6	6.5	7.5
V_2	2.3	4.3	4.9	5.6	6.3	7.3
V_3	1.8	3.5	3.9	4.2	4.5	4.8

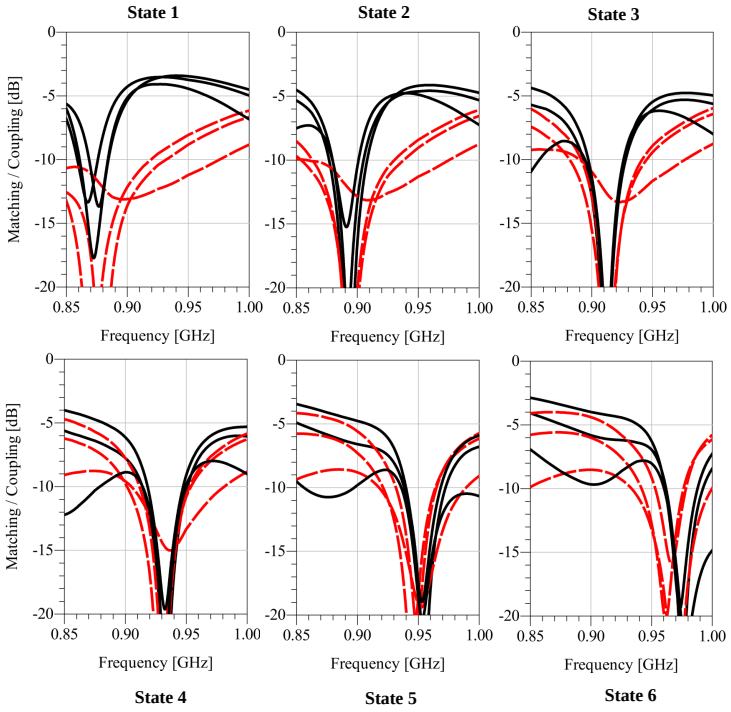

Figure 4.29: Matching (solid) and coupling (dashed) coefficients of the simulated tunable feed network, designed for GSM 900 MHz frequency band.

Summary

This chapter described multi-band antenna designs, and diversity/array arrangements to obtain multiple directional patterns. The multi-band antennas provided omni-directional patterns. A fractal antenna structure, known as Sierpinski gasket antenna, was designed. Because of the log-periodic structure of this antenna, it provided self-similar radiation properties at the design frequency bands even after folding. The limitation of Sierpinski gasket, however, is that it can resonate only on multiples of the principle frequency band. Furthermore, all frequency

degrees-of-freedom are accessible at a single port, and the spectral filtering among designed frequencies is not well-defined. Due to these limitations, multi-port multi-band inverted-F antenna was designed. This antenna provided access to frequency degrees-of-freedom at separate ports. These antennas can be used to build diversity arrangements, and multi-band antenna arrays. Design concept of a feed network for the conformal dipole arrangement was also proposed. Such an antenna arrangement covers the whole sphere with three orthogonal patterns. Further frequency resources can be added to this arrangement to add more frequency bands.

Compact multi-band antenna arrays with suitable feed networks can provide simultaneous access to spectral and spatial degrees-of-freedom. Fixed and reconfigurable decoupling and matching networks were designed for such antennas. The simulations of the fixed feed network provided a decoupling and matching bandwith of about 30 MHz. The decoupling and matching networks were made reconfigurable, within a specific frequency band or switched between various (well-separated) frequency bands, by using varactor diodes. Reconfigurable network provided a bandwidth above 100 MHz, achievable in 5 reconfigurable states.

Compared to conventional antenna designs for cognitive radio, multi-band directional antenna systems provide additional access to the *unconventional* directional resource. The presented designs serve as proof-of-principle approaches, with no specific application in mind, and correspondingly no efforts for ultimate miniaturisation. The size can be reduced by an appropriate choice of the individual antenna element (monopole, slot, patch etcetera) and array arrangement.

5. REALISED ANTENNA SYSTEMS

Measurement results of the fabricated antennas are presented in this chapter. The scattering parameters (reflection and coupling) were measured with a network analyser. The radiation parameters (radiation patterns, radiation efficiency, gain/-directivity) were measured inside an anechoic chamber. The beam patterns of the realised antennas were analysed for their orthogonal radiation patterns in different directions, and self-similar radiation patterns at different frequency bands. In order to analyse how well the realised antenna systems succeed in defining the frequency-direction interface, the correlation coefficient among the radiated modes $\vec{f_l}(\Theta, \phi)$ and $\vec{f_k}(\Theta, \phi)$ defined by eq. (2.27) was used.

A low correlation among the radiation modes at one frequency indicates that the radiation patterns are orthogonal. A high correlation among modes at different frequency bands indicates that the radiation patterns at different frequency bands are self-similar. Orthogonal beam patterns in different directions, and self-similar patterns among various frequency bands reduce the burden on signal processing for directional communications in CR.

The multi-band antennas, Sierpinski and IFA, were evaluated for their frequency filtering, and self-similar radiation capability. The multi-port multi-band antenna arrays were analysed for the frequency and directional filtering capability.

5.1 Sierpinski Antenna

The 2-stage Parany Sierpinski gasket, described in section 4.1.1, was fabricated on Rogers RO4003 substrate with $\epsilon_r = 3.38$, thickness = 0.508 mm, and a copper cladding of 17 μm. It was seen that $\alpha = 60^o$ and a ground plane of 98.6 mm^2 provided the optimum log-periodic behaviour for Sierpinski gasket. The area occupied by the antenna without the feed was 81.3 $mm^2 \approx (\lambda_g/2)^2$ at the base frequency (900 MHz), where λ_g is the guided wavelength. In order to reduce the size of the gasket to $(\lambda_g/4)^2$, the upper portion of the largest gasket was folded to the back side of the substrate [43]. The antenna was fed with a microstrip line of 80 mm.

The fabricated folded Sierpinski antenna is shown in Fig. 5.1. The reflection coefficient (S_{11}) of the folded Sierpinski is shown in Fig. 5.2. The antena exhibits matching at 900 MHz, 2 GHz and 3.6 GHz. However, folding resulted in

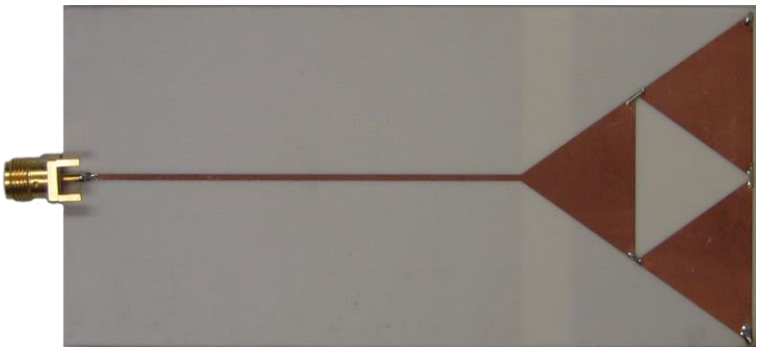

Figure 5.1: Photograph of the 2-stage folded Sierpinski antenna realised on Rogers RO4003 substrate. The upper portion of the largest gasket is folded on the back of the substrate.

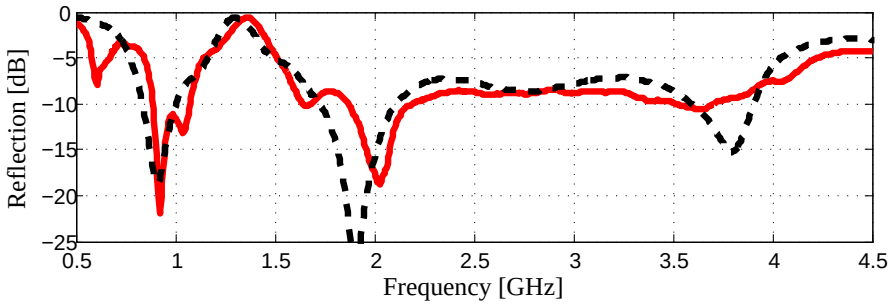

Figure 5.2: Measured (solid) and simulated (dashed) reflection coefficient of the folded Sierpinki antenna.

Table 5.1: Self-similarity, eq. (2.27), of radiation patterns at 2 GHz (f_2), and 3.6 GHz (f_3) with respect to the radiation pattern at 940 MHz (f_1)

Frequency band	ρ
f_2	0.632
f_3	0.716

wideband matching above 2^{nd} harmonic. This effect was also observed in the simulations. The respective gains, shown in Fig. 5.4 were comparable to the gain of a monopole antenna, especially at the 2^{nd} and 3^{rd} harmonics. The normalised radiation patterns, shown in Fig. 5.3, exhibit self-similarity at the design frequency bands. The correlation coefficients are summarised in Table 5.1.

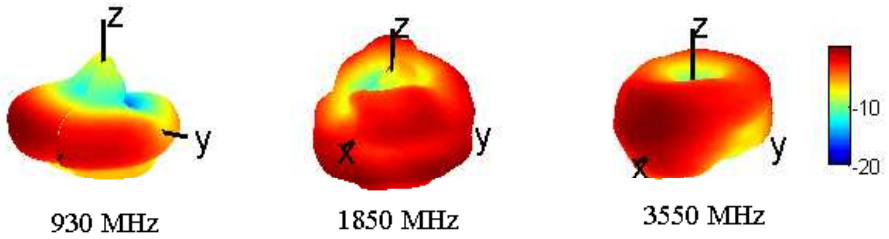

Figure 5.3: Measured radiation patterns of the two-stage Sierpinski antenna at resonance frequencies $f_1 = 940$ MHz, $f_2 = 1.85$ GHz, and $f_3 = 3.55$ GHz. all three patterns are self-similar and omnidirectional (monopole-like).

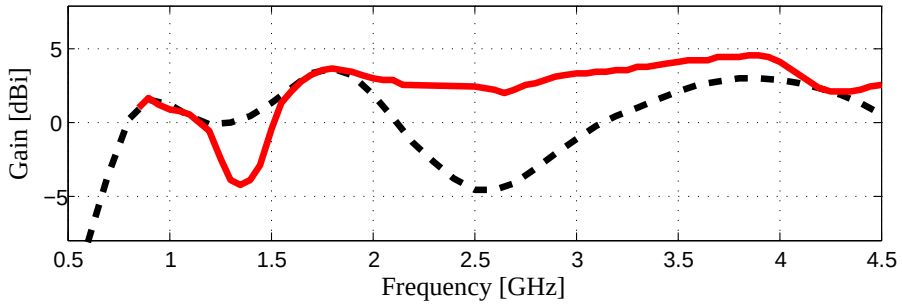

Figure 5.4: Measured (solid) and simulated (dashed) realised gain of the folded Sierpinki antenna.

5.2 Multi-port Multi-band Inverted-F Antenna

The design of a multi-port multi-band inverted-F antenna was presented in section 4.1.2. This antenna was fabricated on Rogers RO3010 with a height of 1.27 mm. The fabricated antenna is shown in Fig. 5.5. The simulated and measured reflection coefficient of the antenna are shown in Fig. 5.6. The three ports of the antenna provide resonance at 900 MHz, 1.85 GHz, and 2.5 GHz, respectively. Contrary to the Siepinski gasket antenna, IFA succeeded in achieving good spectral filtering at the ports. The narrow bandwidth at the lower frequency band is attributed to the fact that the ground plane for the lower resonance is defected by the addition of higher resonances.

The radiation patterns at the three frequency bands (ports), shown in Fig. 5.7, were omnidirectional. The self-similarity among the patterns was better than 50% at the resonance frequency bands. Self-similarity coefficients are summarized in Table 5.2. The frequency filtering, and spatial self-similarity features make this antenna

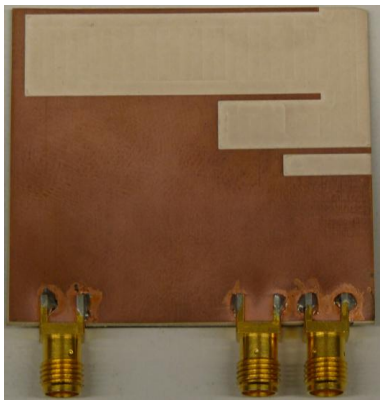

Figure 5.5: Photograph of the multi-port multi-band IFA fabricated on Rogers RO3010 substrate.

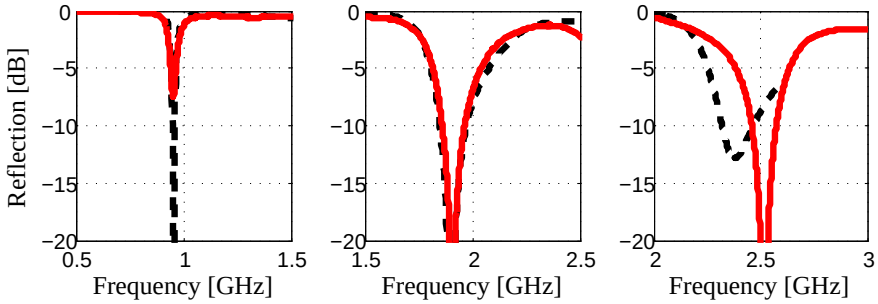

Figure 5.6: Measured (solid) and simulated (dashed) reflection coefficient of the multi-port multi-band IFA, at three ports of the antenna (Fig. 5.5).

Table 5.2: Self-similarity (eq. (2.27)) of the radiation patterns of multi-port multi-band IFA, with reference to $f_1 = 900$ MHz.

Frequency bins	ρ
f_2	0.704
f_3	0.575

element suitable for building arrays, or planar diversity arrangements discussed in section 4.2 and 4.3, respectively.

5.3 Conformal Dipole Arrangement

Feed network for a conformal dipole arrangement, designed at ETH Zürich [78], was developed using the procedure described in section 4.2.1. The antenna shown in Fig. 5.8(a) was designed for 900 MHz. Dipole arms of this antenna could be

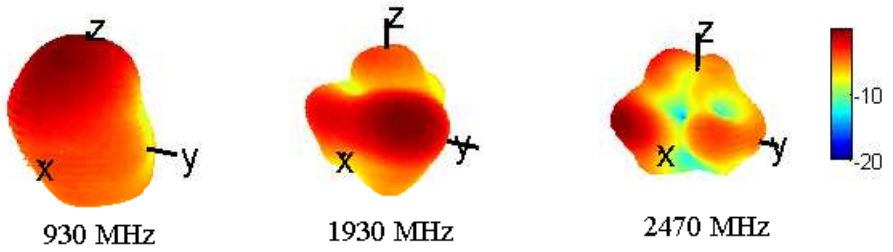

Figure 5.7: Measured radiation patterns of the multi-band multi-port IFA. The patterns at the three ports are self-similar and omnidirectional (monopole-like).

fed inside a metal sphere of 30 mm diameter. The feed strategy developed for this antenna is shown in Fig. 5.8(b). The balun in the middle converts the unbalanced (common) mode of the coaxial transmission line to balanced (differential) mode at the ports of the dipole antenna. The arms of one out of three dipoles can be selected using SP3T switch at the differential outputs of the balun.

The balun and the SP3T switch network were fabricated on the printed circuit board, and tested for the desired functionality. The circuits were realised on Rogers RO3010 substrate with a height of 1.27 mm. All transmission lines were

(a) Conformal dipole arrangement [78]

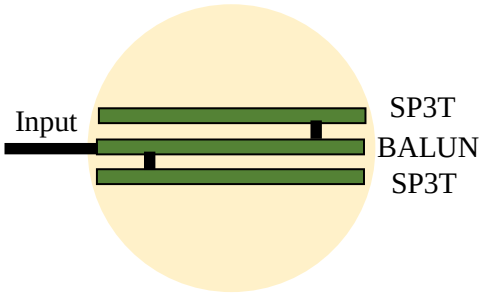

(b) Feed strategy for the conformal antenna [78]

Figure 5.8: (a) Conformal dipole arrangement, and (b) the feed strategy developed for this arrangement. The thick green lines illustrate the printed circuit boards. The black lines indicate transmission lines.

designed as coplanar waveguide with ground (CPWG), and DC block capacitors were used at the RF ports.

5.3.1 Balun

$ETC1-1-13V5$ transformer from M/A-COM [1]was used to realise a balun. Test circuit for the balun circuit was manufactured as shown in Fig. 5.9.

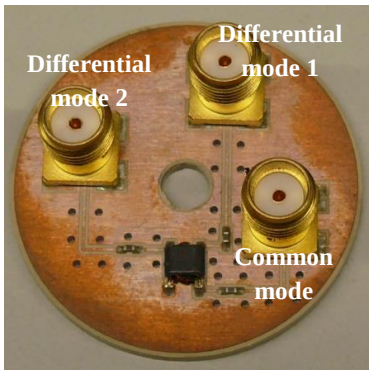

Figure 5.9: Test circuit of balun for the conformal dipole antenna arrangement (Fig. 4.10). The balun converts the common (unbalanced) mode to the differential (balanced) mode.

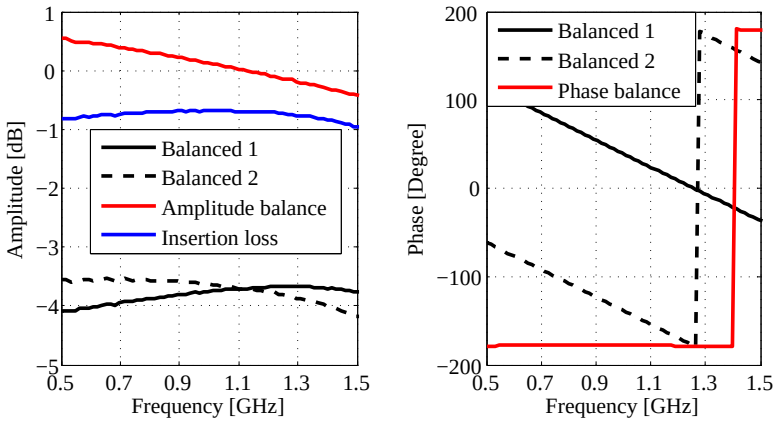

(a) Amplitude balance (b) Phase balance

Figure 5.10: Measurement results of (a) amplitude and (b) phase balance of the balun (Fig. 5.9), for conformal dipole arrangement. Legends define the coloured lines in the graphs.

[1]M/A-COM Technology Solutions Inc. Chelmsford Street 100, Lowell, 01851 Massachusetts . [Online] http://www.macomtech.com.

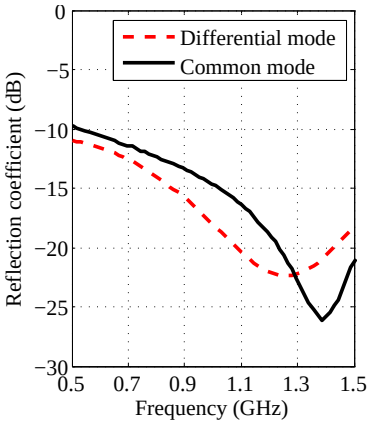

Figure 5.11: Measurement results of matching for the common and differential modes of the balun (Fig. 5.9) for the conformal dipole arrangement.

The performance of the balun was characterised by the amplitude balance, phase balance, insertion loss, and reflection coefficient at the balanced and unbalanced ports. The amplitude and phase balance were calculated by

$$T = \frac{S_{21}}{S_{31}} \tag{5.1}$$

where S_{21} and S_{31} represent the transmission coefficients from unbalaced port (1) to balanced ports $(2, 3)$. Insertion loss was calculated as

$$I = S_{21} - S_{31}. \tag{5.2}$$

The reflection coefficient at the differential port was calculated by the formula

$$S_{11} = \frac{1}{2}(S_{22}^2 + S_{33}^2) - \frac{1}{2}(S_{23}^2 + S_{32}^2), \tag{5.3}$$

where S_{22} and S_{33} are the reflection coefficients at the balanced ports and S_{23} is the transmission between the balanced ports. The measurement results, shown in Fig. 5.10 and 5.11, indicate a low insertion loss of 0.8 dB, amplitude balance of $+/-0.5$ dB, phase balance of 180^0, and reflection coefficient lower than -10 dB for both the common (unbalanced) and differential (balanced) modes.

The circuit for the balun was fabricated on a circular PCB with a diameter of 30 mm, such that it fit inside the feed sphere of the isotropic antenna [78]. The fabricated circuit is shown in Fig. 5.12. The hole, in the middle of the PCB, holds the screw of the feed sphere. It also supports the whole feed network inside the sphere. Differential port 1 of the balun was modelled on top of the board such

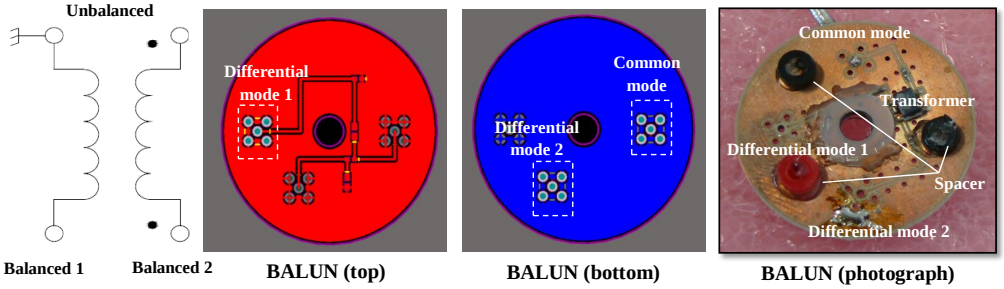

Figure 5.12: The printed circuit board of the balun employing transformer to convert common (unbalanced) coaxial mode to differential (balanced) mode, excited by the dipoles.

that it could be directly connected to the combined port (RFC) of the upper SP3T switch. Differential port 2 and common port were designed at the bottom of the circuit board, where the second SP3T board was connected.

5.3.2 Switch Network

SP3T switch networks were built using HMC245QS16 SP3T switch IC from Hittite[2]. A test circuit of the switch network was built on Roger RO3010 substrate with 1.27 mm height. The measurement results of the resultant switch network,

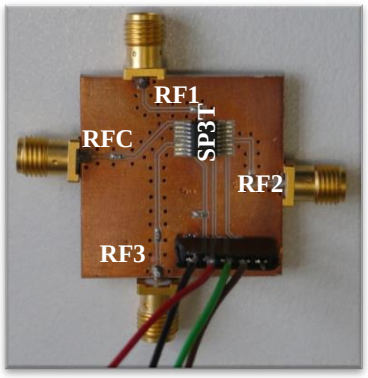

Figure 5.13: Test circuit of the switch network for the conformal dipole antenna arrangement (Fig. 4.10). The combined RFC port is connected to one of the three (RF1, RF2, RF3) ports depending on the control voltages applied at SP3T IC. All RF ports contain DC block capacitors.

[2]Hittite Microwave Corporation. [Online] http://www.hittite.com.

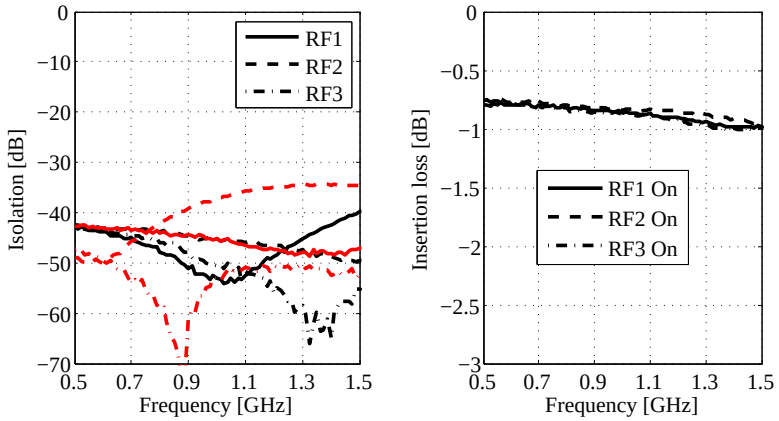

(a) Isolation between the RF ports in OFF (black) and ON (red) state

(b) Insertion loss from the input port (RFC) to the switched RF ports

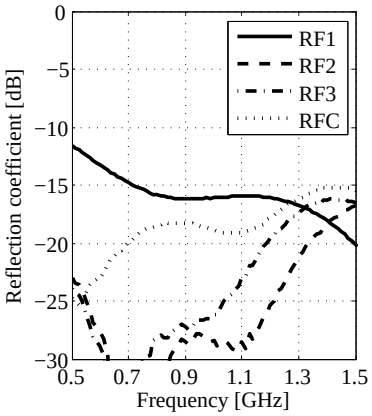

(c) Reflection coefficient at the input and output ports

Figure 5.14: Measurement results of the SP3T switch network for the conformal dipole arrangement. The combined port RFC is connected to one of the three (RF1, RF2, RF3) ports depending on the control voltages.

Fig. 5.14, show 30 dB isolation in the OFF states, 1 dB insertion loss in the ON states, and reflection coefficient less than -15 dB.

Two switch networks were fabricated on circular PCB of 30 mm diameter. The RF ports RF1, RF2, and RF3 shown in Fig. 5.15 were realised as three pins (ground, signal, ground). These RF ports were at angular displacement of 120^0 from each other (in coherence with the location of dipole arms). RFC port was connected to the balun PCB with a $SM86$ cable, and is designed as MMCX connector. Four control lines were provided for Ground, Vcc, Ctrl A, and Ctrl B. Two such PCB were used to feed the upper and the lower hemisphere of the conformal antenna

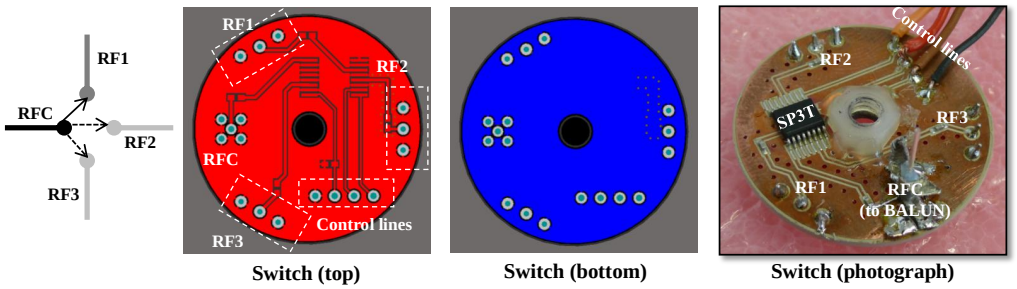

Figure 5.15: The sketch, top, bottom, and photograph of the printed circuit board of the SP3T switch.

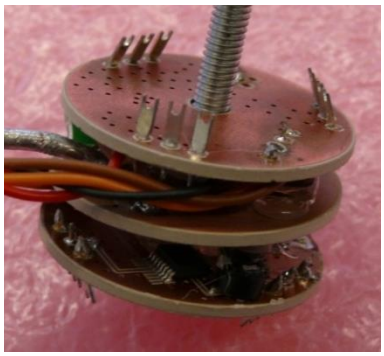

Figure 5.16: Combined feed network for the conformal dipole arrangement [78], consisting of a balun surrounded by two SP3T switches on both sides.

with a balun PCB in the middle. Spring connectors were used on the switch boards to connect the arms of the dipoles on the switch network boards as shown in Fig. 5.16.

The design presented difficulty with the mounting of the dipole arms, and strength of the spring contact. Hence the pattern measurements with the feed network could not be performed in the anechoic chamber. Nevertheless, the design principles for such an arrangement were studied, and the sample circuits were built and tested.

5.4 Compact Multi-port Multi-band Directional Antenna System

The fixed and tunable feed networks for the compact multi-port multi-band directional antenna system, explained in section 4.3, were fabricated on 1.27 mm thick Rogers RO3010 substrate. The photograph of the fixed feed network for the

compact antenna system (Fig. 4.13) is shown in Fig. 5.17. The coloured circles indicate the feed network for each of the three design frequency bands. The network consisted of nine input and nine output ports, to provide with separate and simultaneous access to the nine degrees-of-freedom.

Fig. 5.18 shows the measurement results for matching and coupling of the multi-port multi-band antenna array, with and without the feed network. Stubs were required for the upper frequency bands to improve matching at input ports of the feed network. A decoupling and matching bandwidth of about 30 MHz was achieved at all ports, for the compact array (Fig. 4.13) with an inter-element spacing of $\lambda/6$.

Radiation patterns of the compact antenna system (antenna array and the feed network) are shown in Fig. 5.19, at all nine input ports (3 frequency bands). Fig. 5.19(a) depicts the patterns at the three ports of GSM 900 MHz network with different line types. It can be seen that the patterns point in orthogonal directions. Similar results are obtained for GSM 1800 MHz and IEEE 802.11 b/g in Fig. 5.19(b) and 5.19(c), respectively. Comparison of the directional patterns at all three frequency bands indicate a certain level of self-similarity for the theta-cut shown in Fig. 5.19. The three-dimensional patterns, shown in Fig. 5.20, reinforce this observation.

The gain at all frequency-direction pairs is shown in Table 5.3. The efficiency of the network for a representative radiation mode of the compact antenna system is shown at different frequency bands, in Fig. 5.21. It can be seen here that the radiation efficiency of this mode varies from 60 % to 70% indicating a loss of about $30 - 40\%$ in the feed network.

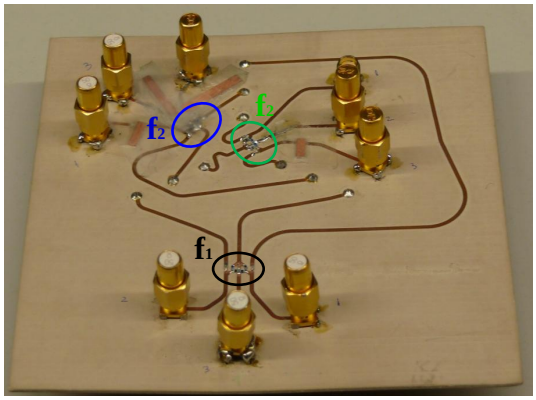

Figure 5.17: Photograph of the feed network for compact multi-port multi-band array (Fig. 4.13). The coloured circles indicate the feed network for different design frequency bands.

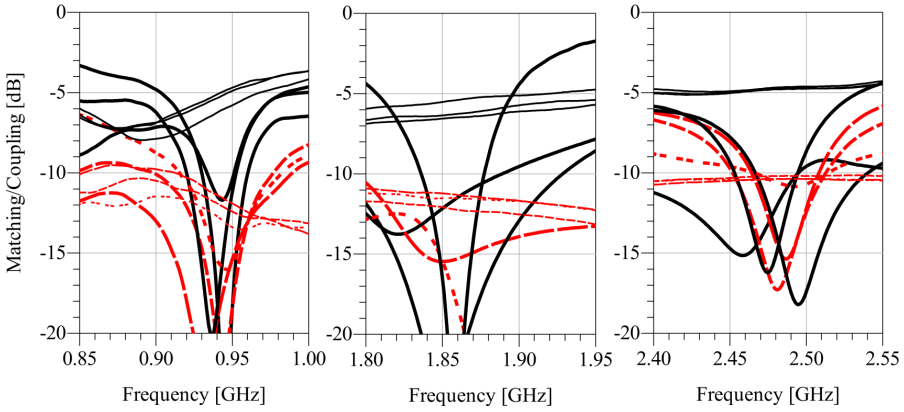

Figure 5.18: Reflection (solid) and coupling (dashed) coefficient of the fabricated multi-port multi-band antenna system at the three design frequency bands. The results are shown with (thick) and without (thin) the feed network.

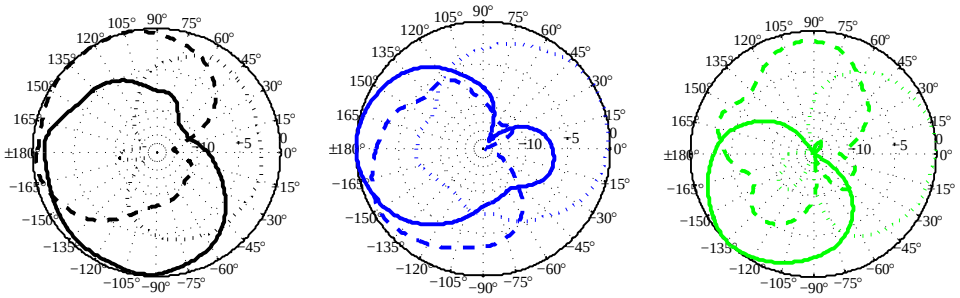

(a) 940 MHz (b) 1850 MHz (c) 2460 MHz

Figure 5.19: Measured radiation patterns of the multi-port multi-band directional antenna system (Fig. 4.13). The radiation patterns at (a) f_1, (b) f_2, and (c) f_3 (colours) are depicted for three directions (line-types).

Orthogonality among radiation patterns in different directions, and self-similarity among different frequency bands was calculated using the correlation coefficient. Orthogonality among directions calculated with respect to direction d_1 is shown in Table 5.4. The correlation coefficient among direction d_1 and d_2 was large for higher frequency bands. The self-similarity among the radiation patterns at different frequency bands calculated with reference to frequency f_1 is shown in Table 5.5. A correlation coefficient higher than 70% was calculated for all frequency bands, indicating self-similar directional patterns among frequency bands.

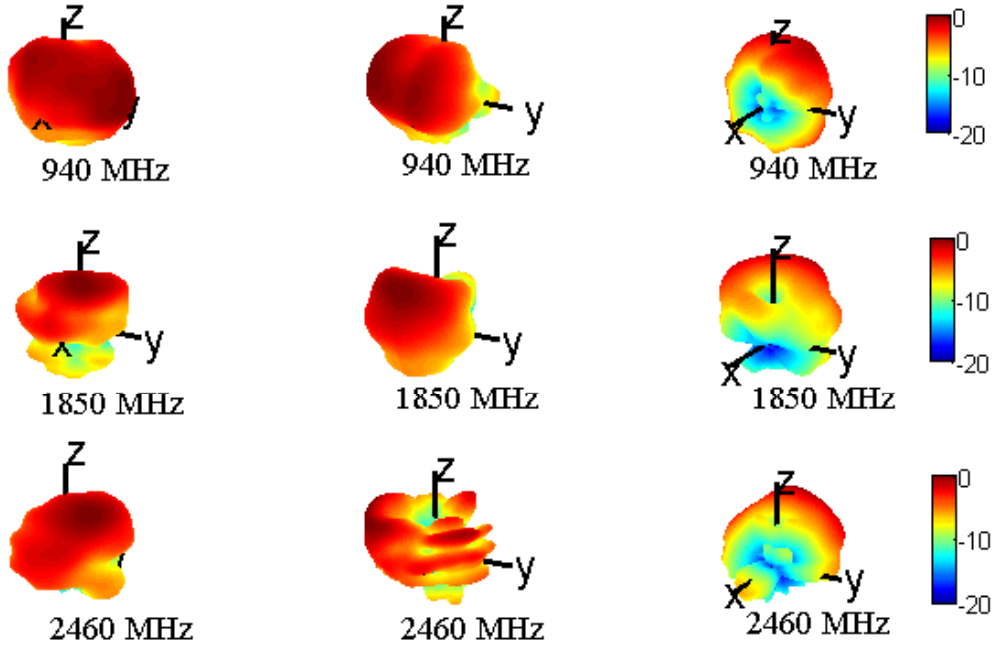

Figure 5.20: Measured three-dimensional radiation patterns of the multi-port multi-band directional antenna system. The directional patterns at one frequency band (rows) are orthogonal and the patterns at different frequency bands (columns) are self-similar.

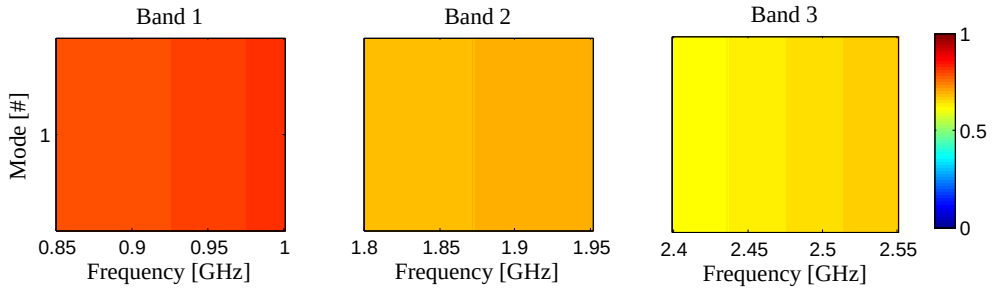

Figure 5.21: Conversion efficiency of the fabricated feed network for a representative radiation mode.

5.5 Reconfigurable Feed Network

Tunable feed network was fabricated for GSM 900 MHz array of the compact multi-band directional antenna array, shown in Fig. 4.13. This work was supported by a Master thesis [13]. The network consisted of three tunable capacitors realised with reverse biased varactor diodes. The network was fabricated on Ro-

Table 5.3: Gain of the measured compact multi-port multi-band directional antenna system, over all θ and ϕ at different frequency bands and directions, in dBi.

Direction	Frequency band		
	f_1	f_2	f_3
d_1	4.7	7.9	4.5
d_2	4.8	7.7	3.57
d_3	8.7	6.6	7.3

Table 5.4: Orthogonality (eq. (2.27)) among directions with reference to d_1, for compact antenna system with fixed feed network.

Direction	Frequency band		
	f_1	f_2	f_3
d_2	0.017	0.51	0.39
d_3	0.024	0.14	0.139

Table 5.5: Self-similarity (eq. (2.27)) among frequency bands with reference to f_1, for compact antenna system with fixed feed network.

Direction	Frequency band	
	f_2	f_3
d_1	0.73	0.74
d_2	0.80	0.75
d_3	0.82	0.87

gers RO3010 substrate with 1.27 mm substrate height. The photograph of the fabricated network is shown in Fig. 5.22. The red and yellow cables indicate the DC biasing wires, which were applied to varactor diode through 220 nH RF chokes. 1000 pF DC block capacitors were added to prevent DC flow at RF transmission lines.

Table 5.6: Biasing voltage for the reconfigurable states of the feed network.

Voltage (V)	State					
	State 1	State 2	State 3	State 4	State 5	State 6
V_1	5	5.5	6.1	7.1	8.1	12.5
V_2	5.6	5.8	6.5	6.9	7.9	9.5
V_3	4.4	5.6	4.85	5.1	5.3	5.5

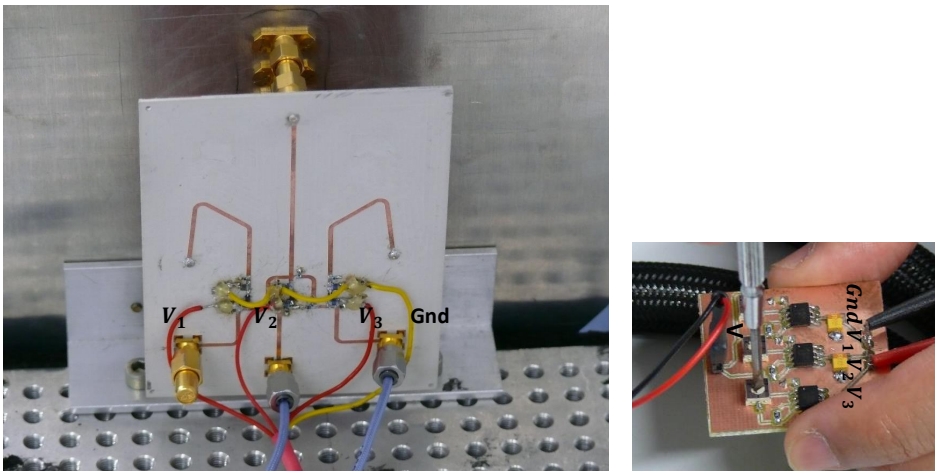

(a) Reconfigurable feed network (b) Voltage regulator circuit

Figure 5.22: (a) Photograph of the reconfigurable feed network for GSM 900 MHz array of the compact multi-band directional antenna (Fig. 4.13). The bias voltages for varactor diodes (V_1, V_2, V_3) were controlled using a voltage regulator circuit (b).

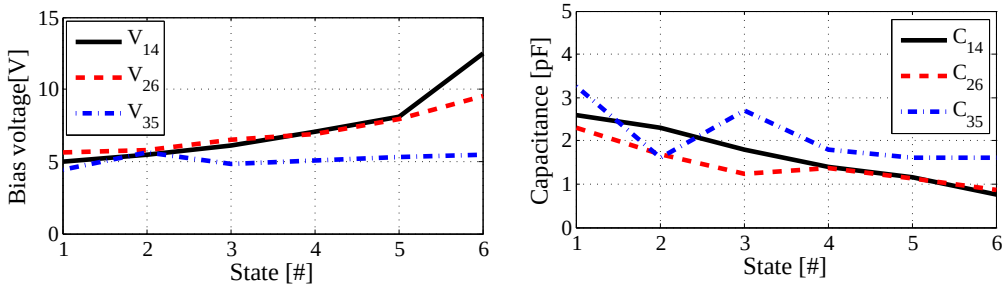

(a) Bias Voltage (b) Capacitance

Figure 5.23: The (a) bias voltage, and (b) capacitance at the reconfigurable states of the feed network.

The biasing voltages to the varactor diodes (V_1, V_2, V_3) were controlled with the help of a voltage regulator circuit built with STMicroelectronics[3] LM317 regulator IC. This circuit consisted of variable resistors, which were used to control the voltage supplied to the regulator ICs. Six frequency states with a 10 dB bandwidth of 20 MHz were obtained by tuning the biasing voltage of the varactor diodes. The voltages required for the tunable states are summarised in Table 5.6. The corresponding capacitor values are shown in Fig. 5.23. A voltage tuning of 5

[3]STMicroelectronics,39, Chemin du Champ des FillesPlan-Les-Ouates, Geneva, Switzerland.

V, corresponding to a capacitance range of 3 pF, was required to achieve a tuning range of about 100 MHz for the feed network. Compared to the simulation results, a constant voltage shift of about 1 V was observed in the measurements. This shift was attributed to the potential drop in the regulator circuit, and other non-idealities.

The decoupling and matching results of the measured states of the reconfigurable feed network are shown in Fig. 5.24. For all states, a matching coefficient better than 6 dB was measured, and a decoupling better than 10 dB was measured for 5 out of 6 states. The azimuth-cut of the radiation modes at the reconfigurable states are shown in Fig. 5.25 for dynamic range of 15 dB. It can be observed that the radiation modes at the output ports of the tunable feed network are orthogonal among each other, for all states. The radiation modes among the reconfigurable states are also self-similar. The Gain of the radiation patterns for all states are summarised in Table 5.3. The correlation among the radiation patterns in different directions, summarised in Table 5.8, is about 40%. The self-similarity among the radiation patterns (Table 5.9), at all reconfigurable states, is better than 80%.

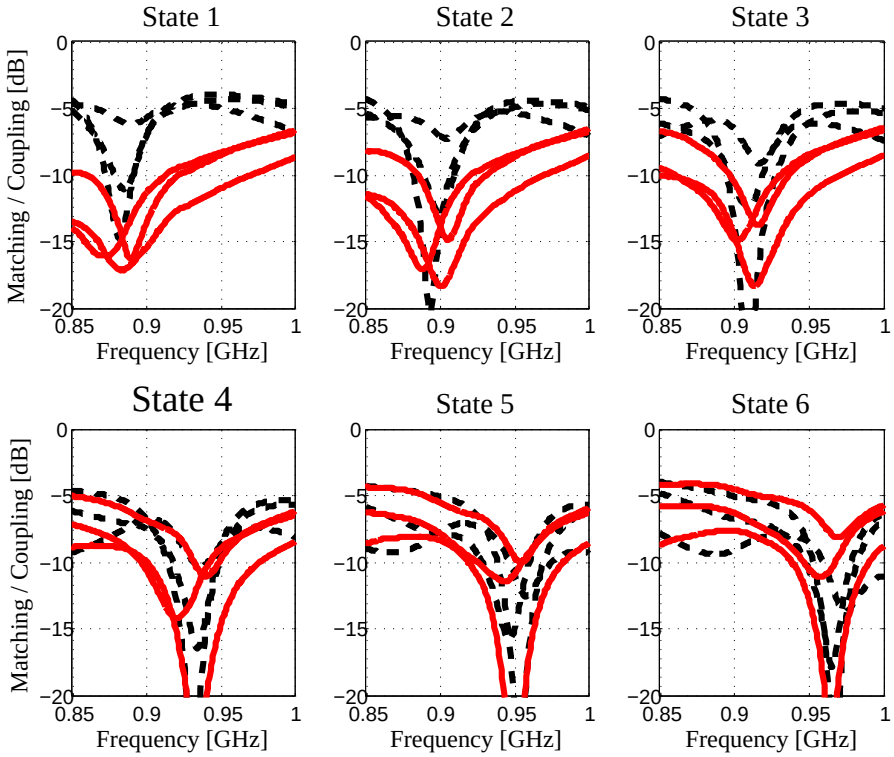

Figure 5.24: Reflection (solid) and coupling (dashed) coefficient of the reconfigurable states of the feed network.

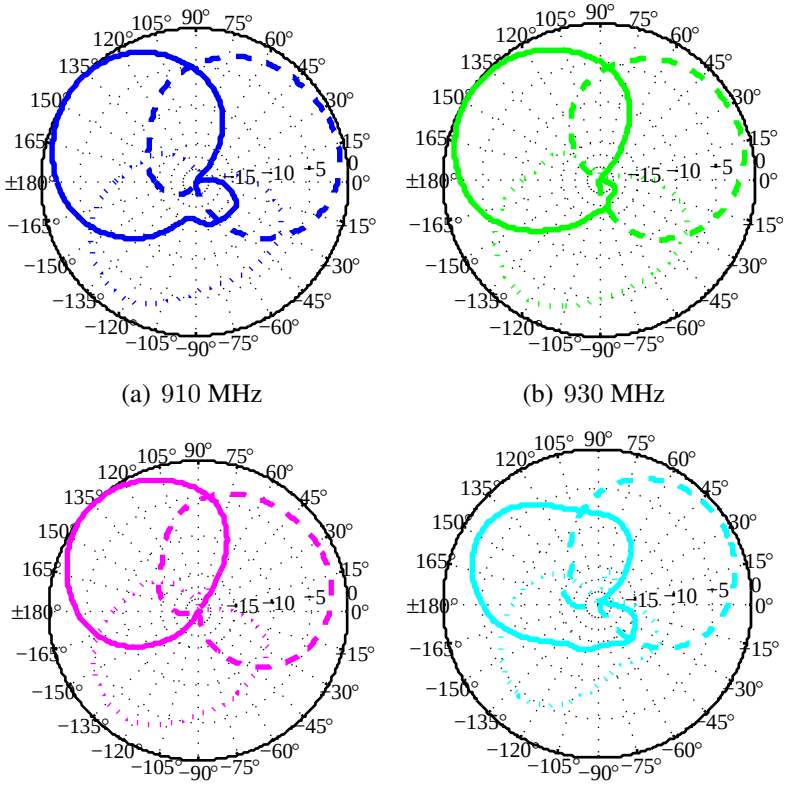

(a) 910 MHz (b) 930 MHz

(c) 950 MHz (d) 970 MHz

Figure 5.25: Measured radiation patterns of the reconfigurable feed network. The radiation patterns for three directions (ports) at the reconfigurable states (a) 910 MHz, (b)930 MHz, (c) 950 MHz, and (d) 970 MHz are illustrated with different colours.

Table 5.7: Gain of the compact multi-port multi-band directional antenna system with a reconfigurable feed network, over all θ and ϕ in different directions and frequency bands, in dBi.

Direction	Frequency band			
	910 MHz	930 MHz	950 MHz	970 MHz
d_1	5.7	5.8	5.7	5.8
d_2	5.8	5.8	5.8	5.7
d_3	5.7	5.8	5.8	5.7

Hence, the reconfigurable feed network successfully provides orthogonal patterns in different directions, and self-similar patterns at different frequency bands. Although, the bandwidth at one frequency state is less than the fixed feed network,

a reconfigurable feed network allows tuning to adjust the operational frequency of the network. Such a reconfigurability behind the aperture of the antenna also ensures undisturbed radiation properties compared to the conventional reconfigurable antennas for CR.

Table 5.8: Orthogonality (eq. (2.27)) among directions of the reconfigurable feed network, with reference to d_1.

Direction	Frequency band			
	910 MHz	930 MHz	950 MHz	970 MHz
d_2	0.38	0.44	0.29	0.32
d_3	0.38	0.44	0.41	0.30

Table 5.9: Self-similarity (eq. (2.27) among frequency bands of the reconfigurable feed network, with reference to f_1.

Direction	Frequency band		
	930 MHz	950 MHz	970 MHz
d_1	0.97	0.96	0.95
d_2	0.98	0.96	0.83
d_3	0.95	0.92	0.86

Summary

This chapter presented measurement results of the realised antenna systems. The multi-band antennas presented in section 5.1 and 5.2 provide monopole-like omnidirectional patterns. These antennas can be used to build diversity arrangements, and multi-band antenna arrays. The frequency filtering of the inverted-F antenna was better than that of the Sierpinski antenna, and it provided multiple frequency bands at multiple ports. These features could be helpful for antenna designs that provide simultaneous and separate access to all resources at port-level. A feed strategy for the conformal dipole arrangement was presented in section 5.3. A successful conversion of the common mode to differential mode was achieved with balun, which converts the coaxial transmission line mode to the differential mode required at the input of the dipole arms. The switch network on both sides of the balun selects the corresponding dipole arms. Such antenna arrangement covers the whole sphere with three orthogonal patterns. The design of such an arrangement may be extended to multiple frequency bands.

The decoupling and matching networks were fabricated for the compact multi-band antenna array. The array provides separate ports for all antenna elements.

Networks for this array were built such that they provided separate access to each frequency band and directional pattern. The measurement results of the fixed feed network in section 5.4 indicated a decoupling bandwidth of about 30 MHz. Extra matching stubs were required in order to provide a 10 dB matching bandwidth of about 30 MHz. A reconfigurable feed network for GSM 900 MHz frequency band was also fabricated. The measurement results indicate matching discrepancy for one of the modes. Nevertheless, a 6 dB matching bandwidth of 20 MHz was achieved.

6. SIMULATION AND EMULATION IN HETEROGENEOUS PROPAGATION SCENARIOS

The results of the measurement campaigns presented in chapter 3 already provide a proof-of-principle that directional antennas are capable of extending the parameter space for CR. Directional opportunities were already observed for a LOS and a static multipath scenario in section 3.3. Since these results are representative of specific static scenarios, the influence of heterogeneous propagation scenarios on directional opportunity is studied in this chapter. Hence, the findings presented in chapter 3 are extended and generalised in the following. Moreover, the influence of mobility on the availability of directional opportunity is also studied. The following aspects must be considered for the analyses of directional antennas for CR:

Antennas - First of all, its important to think about the kind of antennas used for the analyses. Influence of the number of array elements, beamwidth and side-lobe level can be studied.

Channel Model - For the study of directional resources, spatial channel model needs to be considered. The spatial channel model can be two-dimensional or three-dimensional. In this context, existing channel models include SCM (spatial channel model) [41, 81], WINNER (wireless world initiative new radio) [82], WINNER II [68], and ITU (international telecommunication union) [83] channel models. Most of these channel models are two-dimensional. Three-dimensional channels are occasionally considered for WINNER II [84], and ITU channel model for large-scale parameters [85].

Mobility - An interesting feature that can be studied for CR is the impact of mobility on its performance. It is interesting to a evaluate how the directional opportunities differ for a moving node, compared to a static node. The channel models mentioned above do not have any mobility models.

Therefore, spatial channel parameters must be obtained from other sources, for example, existing channel measurements.

Directional opportunity - A significant feature of directional opportunity analyses is the definition of *directional opportunity*. Should it be defined as an absence of signal in one direction at all frequency resources? or in one spatio-spectral pair (direction-frequency bin)? Do the existing spectrum sensing algorithms suffice or new algorithms need to be developed for directional spectrum sensing?

Threshold - Threshold is required to quantify the presence or absence of a white space in cognitive radio, as discussed in section 2.1.1. For energy detection, this threshold is determined based on the receiver noise distribution according to a certain probability of detection and false alarm. Since in simulations, receiver noise energy cannot be computed, threshold can be chosen to have a fixed value, for example, -120 dBm or it can be chosen certain dB below maximum signal strength in all directions.

The most realistic method to perform this evaluation is to perform static and mobile measurement campaigns with the reference and/or designed antenna systems. However, this requires planning of extensive measurement campaigns. Since this is a time- and effort-consuming process, alternatives needed to be investigated. One alternative was to make use of spatial channel models that could provide spatial distribution of multipath in addition to the temporal distribution. In comparison to the conventional channel models, where angular distribution is considered to be uniformly distributed $[0, 2\pi]$, the spatial channel models provide the angular distribution of multipath according to the propagation environment. These models include the geometric channel models [42, 86], measurement based models [69, 87], and geometry-based ray tracer channel models.

Ray tracer based channel models are very specific to the location and environment database used for generation of the channel parameters. On the other hand, there are measurement based channel models like WINNER [69], which are derived from a number of measurements performed at multiple locations around the world. In addition, they provide channel parameters according to the scenario, e.g., micro-cell, macro-cell, urban, rural, indoor, etcetera.

The simulations in this chapter were performed for various static scenarios using *WINNER II SCME* spatial channel model [69]. WINNER channel model, however, does not include mobility parameters. The mobility features of CR were studied using channel sounder measurements in Ilmenau, the *Ilmenau Reference Scenario* [14, 88]. The designed antennas were embedded on to the channel sounder measurements using the techniques described in [89, 90].

Various directional antenna systems were considered to analyse the availability of directional resources for cognitive radio in static and mobile scenarios. Analytical patterns of circular arrays were used to analyse the influence of antenna patterns on directional opportunity for CR. Static scenarios were simulated using WINNER II channel model and mobility scenarios were analysed using channel measurement data from the measurement campaign *Ilmenau Reference Scenario*[1] [91]. Directional opportunity was computed using the existing spectrum sensing technique, energy detection, and dissimilarity analysis introduced already in section 3.3.2.4. The threshold was chosen using two approaches: 1) with reference to the instantaneous maxima, and 2) fixed levels.

6.1 Static Scenario

Simulations were performed for various antenna arrays in heterogeneous static scenarios ranging from rural to highly urban scenarios, using WINNER II spatial channel model (SCME) [69]. The motivation for these simulations was two-fold: 1) to investigate the effect of array patterns, and 2) to analyse the influence of channel properties (propagation scenarios) on directional opportunities.

6.1.1 Simulation Framework

A generic block diagram of a CR communications scenario is shown in Fig. 6.1, where a primary transmitter is connected to a CR node through a spatial channel. The simulation framework, therefore, requires a spatial channel model, a directional antenna system, and directional opportunity analysis at the CR node.

WINNER II channel model follows a geometry-based stochastic channel modelling approach, which allows creation of an arbitrary radio channel. The channel parameters (complex multipath powers, angle of arrival) are determined stochastically, based on statistical distributions extracted from channel measurements. Moreover, channel models are antenna independent, which implies that different antenna patterns can be embedded on to the channel parameters [69].

To extract the channel parameters from WINNER II channel model, the simulation parameters (e.g., frequency, time samples) are set in the structure *wimpar*, and the simulation layout (e.g. location of nodes, scenario definition) is set in the structure *layoutpar*. The model then computes the channel parameters which can be used to embed the antenna characteristics and to perform further signal processing. Measured and analytical antenna patterns can be embedded on to complex power angular profiles to compute the directional opportunities for heterogeneous propagation scenarios. Due to stochastic nature of the channel, Monte

[1] http://www-emt.tu-ilmenau.de/ReferenceScenario

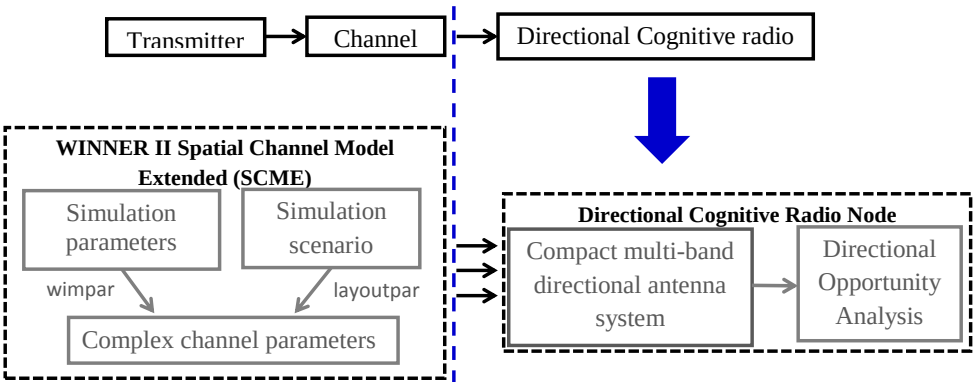

Figure 6.1: Primary transmitter is connected to CR node through a spatial channel. The spatial channel parameters are obtained from WINNER II SCME for simulations. The dashed blue line indicates the interface between the spatial channel and the CR node. Details are discussed in the text.

Table 6.1: Winner II SCME channel scenarios

Scenario	Definition	LOS/NLOS
A2	Indoor to outdoor	NLOS
B1	Typical urban micro-cell	LOS/NLOS
C1	Suburban	LOS/NLOS
C2	Typical urban macro-cell	NLOS
D1	Rural macro-cell	LOS/NLOS

Carlo simulations must be performed to obtain a reliable result from the channel model.

A heterogeneous set of propagation scenarios, shown in Table 6.1, was chosen for simulations. For all these scenarios, Monte Carlo simulations were performed with $10,000$ realisations, where the position of transmit antenna (primary user) was fixed at the origin and the receive antenna was randomly located in an area of 500 m $\times$ 500 m. Height of the transmitter for indoor and micro-cell channels was 2 m, while for the macro-cell it was 32 m. The sensing node was always at a height of 1.5 m. The channel parameters were calculated for a frequency of 2.4 GHz.

At every sense location, complex patterns of the antenna array were embedded on to the complex power angular profiles of the channels and the receive signal strength indicator (RSSI) was computed for every directional pattern. Threshold was applied and a binary decision about the presence or absence of directional op-

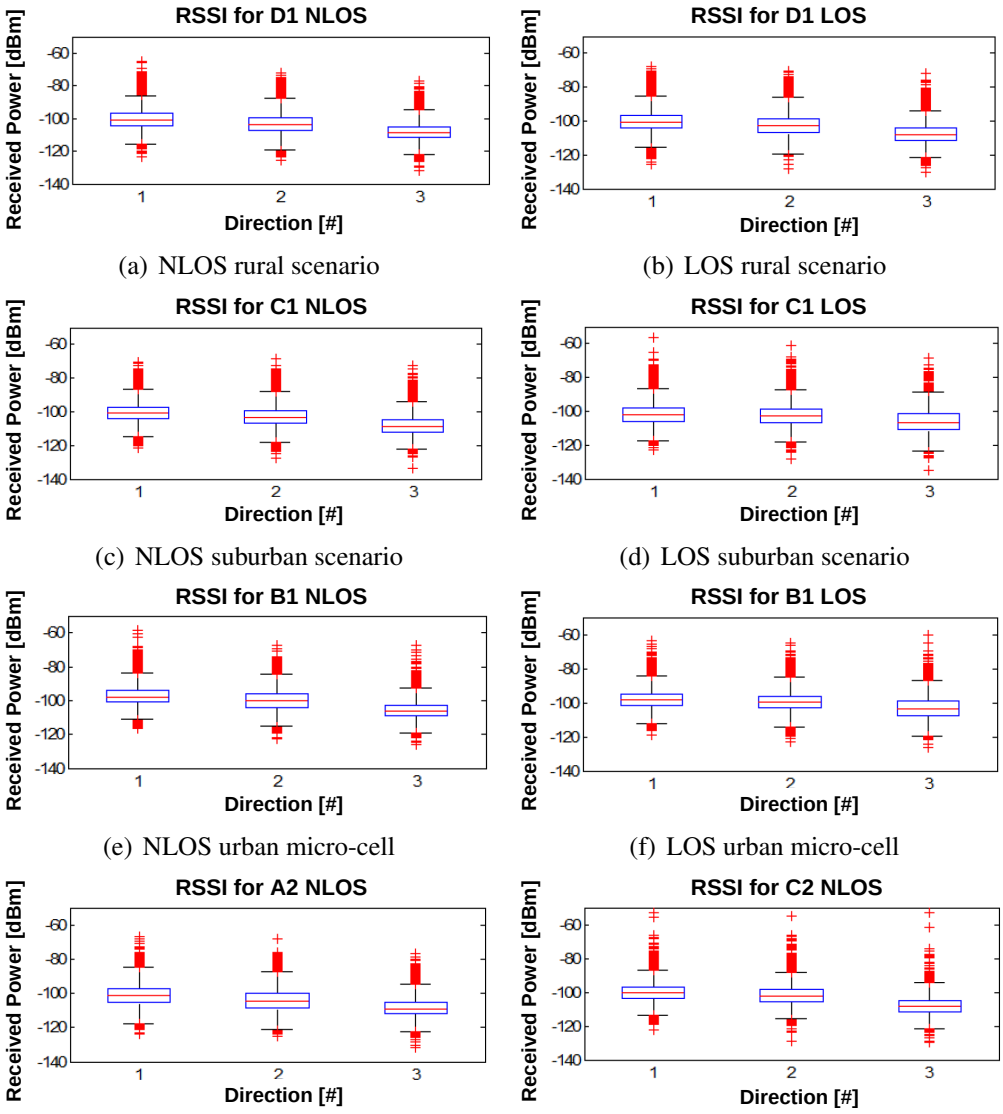

(a) NLOS rural scenario

(b) LOS rural scenario

(c) NLOS suburban scenario

(d) LOS suburban scenario

(e) NLOS urban micro-cell

(f) LOS urban micro-cell

(g) NLOS indoor to outdoor scenario

(h) NLOS urban macro-cell

Figure 6.2: Statistics of the received signal strength by the reference antenna (Fig. 3.9) for LOS and NLOS scenarios of Table 6.1, illustrated with box plot. The middle line indicates the mean value, and the box represents the range of values for 25 % of the locations. The black lines at the far end indicate the range where 75 % of the power levels lie, and the red plus indicate the outliers.

portunity was met. Dissimilarity among these binary vectors for all directions was computed through logical exclusive-OR operation. These steps are summarized in the flow chart shown in Fig. 3.11. The analysis was performed for two cases:

- **Case I** Fixed threshold
- **Case II** Instantaneous threshold

Instantaneous threshold was chosen certain decibels below the maximum among directions, for every snapshot. Fixed threshold was chosen based on the statistics of the received signal strength for the ports of the directional antenna. Statistics of the received signal strength for scenarios in Table 6.1 are illustrated with box plots in Fig. 6.2. The mean values for all scenarios vary from -100 dBm to -120 dBm. The difference between LOS and NLOS cases is mainly outliers which are higher for LOS cases for some scenarios. It is, therefore, interesting to see the situation with directional opportunity for threshold ranging from -100 to -120 dBm for Case I.

6.1.2 Directional Opportunity Analysis for the Reference Antenna System

Performance of the measured sector antenna shown in Fig. 3.7 was analysed by embedding the azimuth patterns on to the scenarios in Table 6.1. The variability of

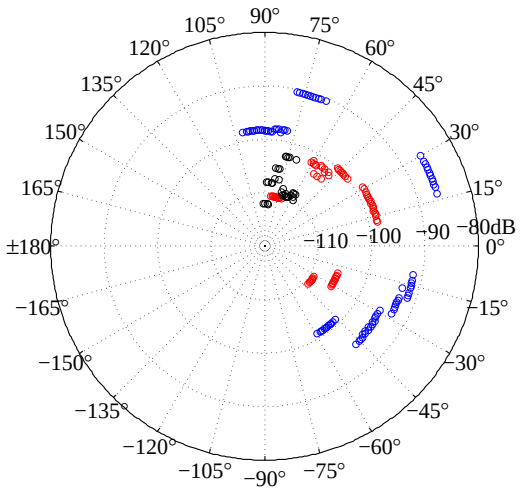

Figure 6.3: Power azimuth profile for D1 NLOS scenario obtained from WINNER II channel model. The colours blue, red, and black represent three consecutive snapshots. The figure illustrates the directional nature of the rural scenario.

the power angular profile for three consecutive realisations in Monte-Carlo simulations is shown in Fig. 6.3 for D1 NLOS scenario. As a representative example, the power received by the three sectors at 2.4 GHz, for 100 realisations in scenario D1 NLOS is shown in Fig. 6.4. From these 100 realisations, it can be observed that for about 50 % of the snapshots, the RSSI in the three directions differ by $10 - 20$ dB, indicating directional opportunity.

Case I

Fig. 6.5 shows the percentage directional opportunity for the reference antenna, for a fixed threshold ranging from -125 dBm to -95 dBm, for a relative transmit power of 0 dBm. The directional opportunity analysis was performed among different directions, and hence does not depend on the absolute transmit power. A

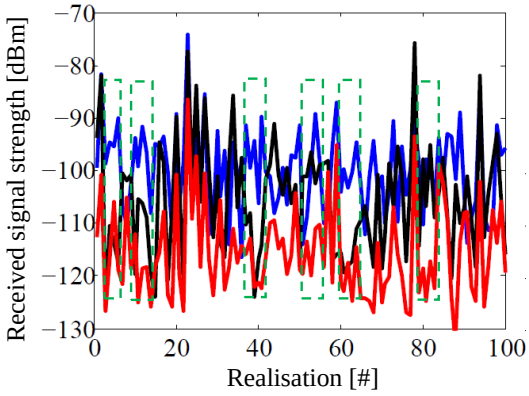

Figure 6.4: Power received by the reference antenna (Fig. 3.9) in NLOS rural scenario for the first 100 snapshots, at 2.4 GHz. Different colours indicate the power received by different directional patterns. The green boxes indicate the opportunity for directional communications.

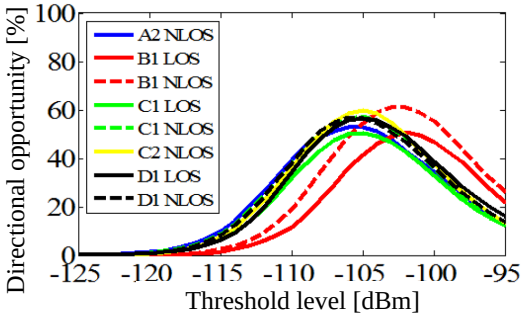

Figure 6.5: Directional opportunity versus threshold for the reference antenna, for the scenarios summarised in Table 6.1.

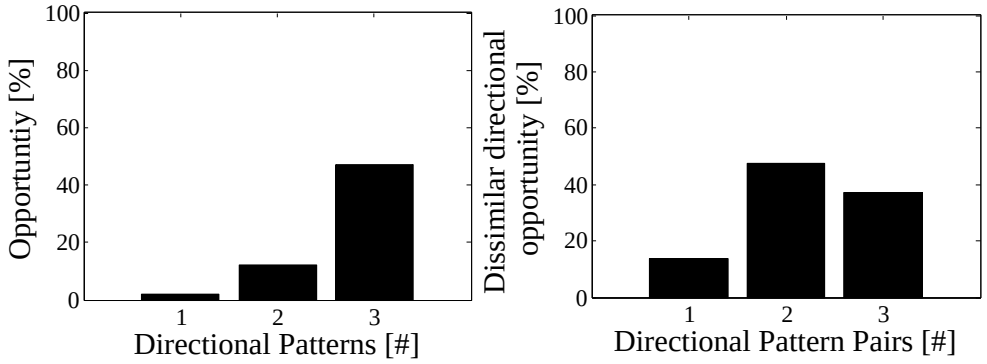

Figure 6.6: Opportunity available at three sectors of the reference antenna (left-hand panel), Fig. 3.9, and dissimilarity among pairs (1) $d_1 - d_2$, (2) $d_1 - d_3$, and (3) $d_2 - d_3$ (right-hand panel), for D1 NLOS scenario of WINNER II channel model. An instantaneous threshold of 20 dB below instantaneous maximum per snapshot was chosen.

directional opportunity was available when it existed for one directional pattern and not for the others. It is evident that for all scenarios, an optimum threshold level exists where the number of directional opportunities is maximum. The optimum threshold level for all cases, except for the urban micro-cell, lies at -104 dBm. When the threshold level was higher or lower than this optimum value, the number of directional opportunities decreased. A higher threshold level resulted in an increase in the number of individual opportunities, while a lower threshold level resulted in a decrease in the number of individual opportunities. For a threshold level of -110 to -100 dBm, a directional opportunity ranging from 40 to 60 $\%$ can be observed. This indicates that a directional opportunity is available for 40 to 60 $\%$ of the total snapshots for all undertaken scenarios.

Case II

It can be observed from Fig. 6.4 that the difference among the received power from different sectors of the reference antenna varies from 5 to 20 dB over snapshots. This indicates that for a threshold level 10 to 20 dB below the instantaneous maximum signal level, directional opportunity exists in rural scenario. For example, the opportunity for and the dissimilarity among the directional patterns of the reference antenna in NLOS rural scenario is shown in Fig. 6.6, for a threshold level that is 20 dB below instantaneous maximum per snapshot. It can be observed that for the best case ($d_1 - d_3$), about 50 $\%$ of the snapshots provide a directional opportunity in the rural scenario.

In general, directional opportunities were obtained for all scenarios under discussion. However, the reference antenna has narrow beamwidth and low side-lobe

level due to the presence of metal walls between the array elements. Since such metal walls are not practical and hence the results obtained above cannot be generalised, it was found reasonable to analyse the performance of various circular antenna arrays in heterogeneous propagation scenarios. These analyses provide guidelines for designing antennas for directional communications.

6.1.3 Directional Opportunity Analysis for Analytical Circular Array

Circular arrays of monopoles were analysed in the desired set of scenarios. The radiation patterns of these arrays were calculated from that of a dipole array with an addition of 3 dB in the gain. The radiation pattern of a dipole array can be computed from the element factor [3]

$$EF = \eta \frac{|I_o|^2}{8\pi^2} \sin^3\theta, \tag{6.1}$$

and the array factor

$$AF(\theta, \phi) = \sum_{n=1}^{N} I_n e^{jka[\sin\theta\cos(\phi-\phi_n)-\sin\theta_o\cos(\phi_o-\phi_n)]}, \tag{6.2}$$

as

$$\text{Array Pattern} = EF \times AF. \tag{6.3}$$

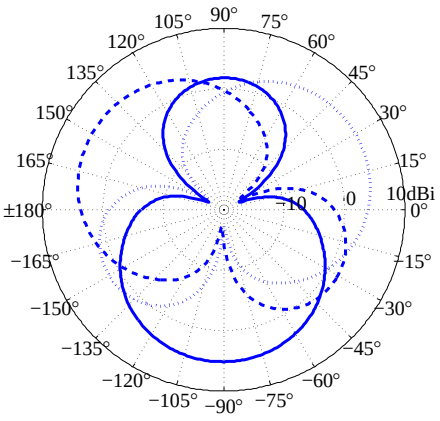

Figure 6.7: Analytical patterns of a $3-$element uniform circular array of monopoles with an inter-element spacing of $\lambda/2$. Three directional patterns are created by rotating and aligning them to the measured patterns of the reference antenna, cf. Fig. 3.9, for a comparison.

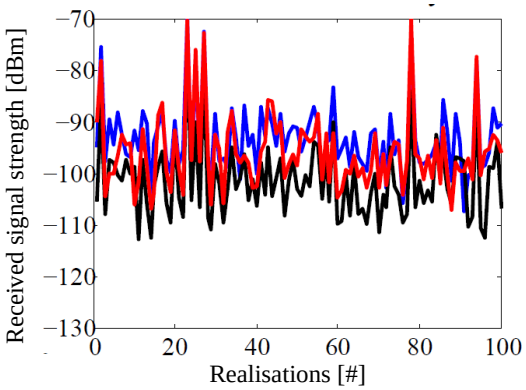

Figure 6.8: Power received by a 3-element uniform circular array in NLOS rural scenario for the first 100 snapshots, at 2.4 GHz. Different colours indicate the power received by different directional patterns.

θ and ϕ represent elevation and azimuth angle respectively, θ_o and ϕ_o are the desired beam direction, η is the free space impedance, k is the wave number, a is the radius of the circular array, I_n is the excitation coefficient, $\phi_n = \frac{2\pi}{N}$, and N is the number of elements in the array.

The radiation patterns of a uniform circular array of monopoles, represented in Fig. 6.7, were embedded on to the complex power angular profiles for the NLOS rural scenario (D1). The resultant received power for 100 realisations, shown in the Fig. 6.8, indicates that the analytical patterns receive more power than the measured patterns, cf. Fig. 6.4. This is due to higher beamwidth and back-lobe level of the analytical patterns, compared to the measured patterns of the reference antenna. Moreover, due to higher back-lobes, the received power levels from all three sectors are comparable, resulting in less directional opportunity. Side-lobe suppression algorithms were applied to reduce the side-lobe level for a circular array.

6.1.3.1 Influence of the Side-lobe Level on Directional Opportunity

The side-lobe level of an antenna array can be reduced by tapering the amplitude of the excitation vectors of an array, where the narrowest beam is achieved with uniform excitation but at the expense of highest side-lobe level. For the simulations described below, the side-lobe level was suppressed by applying a Chebyshev window to the phase-mode excitation vectors of the circular array, as described in [92]. The effect of side-lobe suppression for a 3-element array can be seen in Fig. 6.9. The beamwidth of the antenna becomes wide as the side-lobes are suppressed through windowing. It should be further noticed that a very narrow beam with very low side-lobe level cannot be created using a small number of

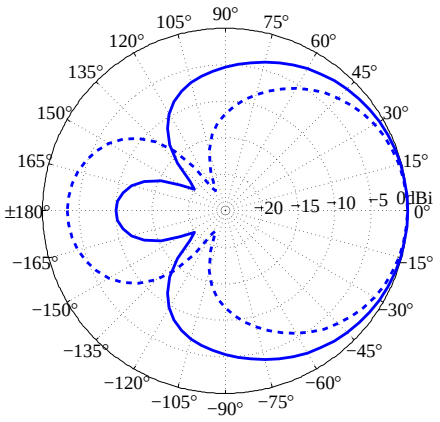

Figure 6.9: Analytical radiation patterns of a 3-element array with (solid) and without (dashed) side-lobe suppression (SLS).

weakly directive elements. The side-lobe level of the array pattern can be reduced further by increasing the number of array elements.

Analytical patterns of the uniform and tapered array were used to perform directional opportunity analysis for fixed and instantaneous threshold.

Case I

Directional opportunity was computed for a 3-element circular array with a threshold level ranging from -115 to -95 dBm. The resultant directional opportunity with and without side-lobe suppression is shown in Fig. 6.10. It can be observed that for a 3-element circular array, suppression of the side-lobe level increases the number of directional opportunities, but no significant role in drifting the optimum threshold level. The number of directional opportunities at optimum threshold level for a 3-element circular array were comparable to the reference antenna. The impact of side-lobe suppression was more evident for circular arrays with higher number of elements.

Case II

Instantaneous threshold level was used to compute directional opportunity for a 3-element circular array with uniform excitation, and with side-lobe suppression. An instantaneous threshold ranging from 5 to 20 dB was chosen for the analysis. The results, shown in Fig. 6.11, demonstrate that by reducing the side-lobe level, 5 % to 20 % higher directional opportunity can be achieved, depending on the propagation scenario. Line-of-sight scenarios showed a small improvement of 5 %, while non-line-of-sight (NLOS) scenarios showed a significant increase of about 20 %. Nevertheless, similar trend was seen for all propagation scenarios

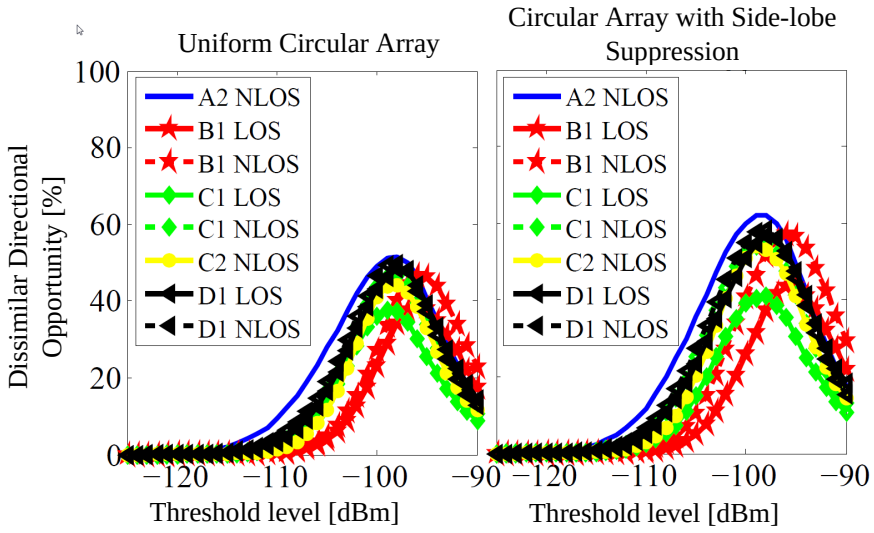

Figure 6.10: Percentage dissimilarity among patterns of a $3-$element array with fixed threshold level for uniform excitation (left-hand panel) and side-lobe suppression (right-hand panel). The results are shown for LOS (solid) and NLOS (dashed) scenarios detailed in the legend (Table 6.1).

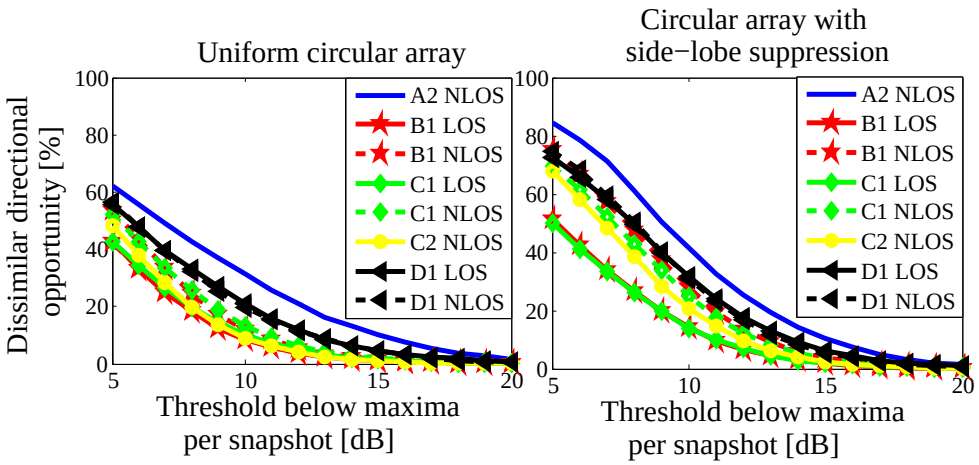

Figure 6.11: Percentage dissimilarity among patterns of a $3-$element array versus threshold below instantaneous maximum for uniform excitation (left-hand panel) and side-lobe suppression (right-hand panel). The results are shown for LOS (solid) and NLOS (dashed) scenarios detailed in the legend (cf. Table I).

undertaken during these analyses. The rural scenario shows similar opportunity level for the line-of-sight and the non-line-of-sight cases, possibly because of the inherent directional nature of the multipath.

It was observed that directional opportunity drastically drops beyond a threshold of 10 dB for a 3-element circular array. This threshold level is comparable to the side-lobe level of a 3-element circular array with tapered excitations (Fig. 6.9). Hence, it can be generalised that side-lobe level plays a decisive role in choosing a threshold level for sensing. Since limited suppression can be achieved for three elements, the effect of the number of elements on directional opportunity is studied in the next section.

6.1.3.2 Influence of Array Size on Directional Opportunity

3 to 12 element circular arrays with an inter-element spacing of $\lambda/2$ were considered for this study. Patterns with side-lobe suppression were considered, while the side-lobe levels were suppressed to the minimum level possible with the indicated number of elements. As seen in Fig. 6.12, the monopole antennas cannot provide very low side-lobe levels while employing a very small number of elements in an array.

Fig. 6.13 shows the directional opportunity on an average as the patterns were rotated over the whole azimuth with N (= number of elements) angular steps. It is apparent from this plot that a saturation is achieved for 6 elements, where directional opportunity ranging from 20 to 50 % was observed for all scenarios. Beyond six elements, increasing the number of elements does not increase the average directional opportunity. Moreover, the beamwidth becomes narrower as

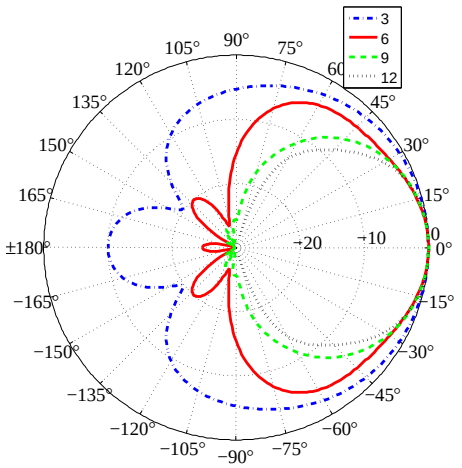

Figure 6.12: Analytical radiation patterns of a $3-$, $6-$, $9-$, and $12-$element circular array with maximum achievable side-lobe suppression (SLS).

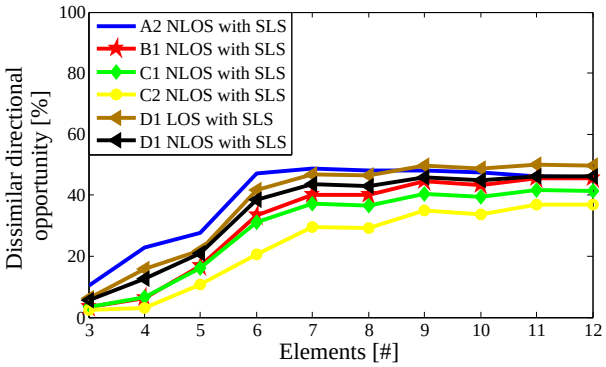

Figure 6.13: Dissimilar directional opportunity versus number of elements for a threshold that is 15 dB below instantaneous maximum per snapshot. The values shown are the mean of the opportunities for the patterns rotated over the whole azimuth.

the number of elements is increased as shown in Fig. 6.12. This decrease in beamwidth also plays a role in the selection of the optimal antenna for directional communications in CR. The opportunity was observed to decrease as the angular spread of the channel becomes lower than the beamwidth of the antenna array, for example, for scenario $A2$ in Fig. 6.13. Similarly for rural LOS scenario, a strong LOS component was observable, giving rise to an increased opportunity compared to the NLOS case. Based on this analysis, it may be concluded that a 6-element array with side-lobe suppression provides maximum directional opportunity in multipath scenarios for a reasonable threshold level. The influence of threshold level on a $6-$element array is shown in Fig. 6.14, where reasonable directional opportunity is observed at a threshold of 20 dB. Directional opportunity is shown with the help of a bar plot in Fig. 6.15 for the best case (when the patterns are pointing in opposite directions), and on average (when the patterns are rotated over azimuth). It can be seen here that for a threshold level 20 dB below the instantaneous maximum per snapshot, saturation is achieved for 9 elements. However, $9-$element-arrays may not be worth the incremental improvement given a significant increase of complexity compared with $6-$element array, especially if the average over the whole azimuth is considered.

From these simulations, it is concluded that the antenna for directional CR communications should have low side-lobe level and narrow beamwidth, where the effect of the side-lobe level is dominant. The optimum side-lobe level depends on the chosen threshold, while a side-lobe level of 20 dB is found to be reasonable. A $6-$element array is capable of providing desired side-lobe level and, hence, sufficient directional opportunity at an instantaneous threshold level of 20 dB. Furthermore, since the chosen spatial channel model provides power angular

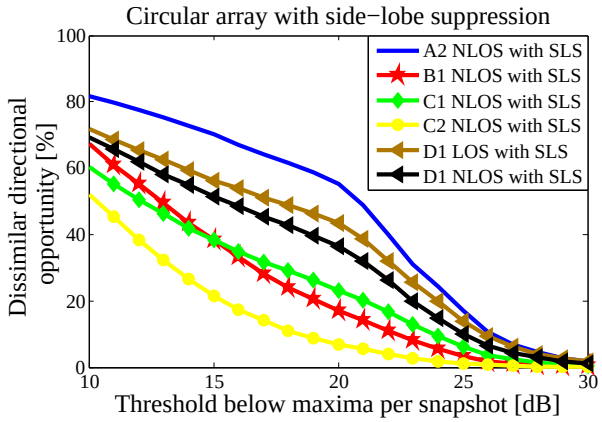

Figure 6.14: Dissimilar directional opportunity among patterns of a $6-$element array versus threshold below instantaneous maximum for side-lobe suppression.

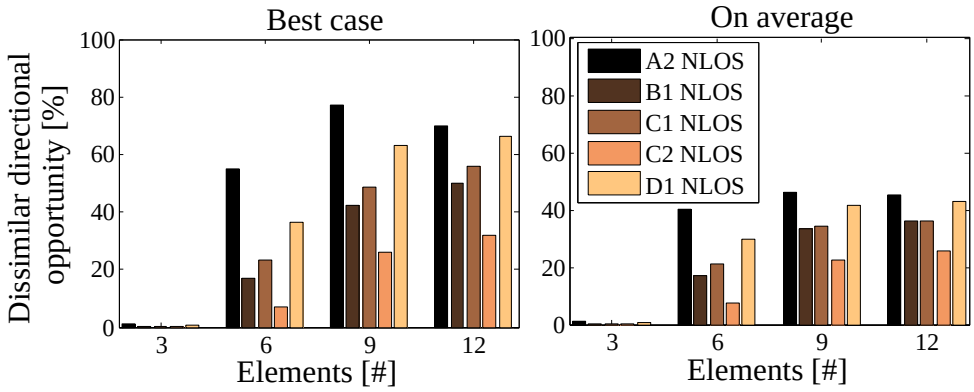

Figure 6.15: Dissimilar opportunity versus number of elements for a threshold that is 20 dB below instantaneous maximum per snapshot, for the patterns pointing at opposite directions (left-hand panel) and on average when the patterns were rotated over the whole azimuth (right-hand panel). The results are shown for the case of side-lobe suppression only.

profiles in a stochastic way, the conclusions from these simulations can be generalised for any spatial channel model.

6.2 Mobility Scenario

Simulations for a static scenario showed promising results, which motivated the exploration of directional antennas in the case of mobility. Since measurements of

a mobile CR node is time- and effort-consuming, mobility scenario was analysed by embedding directional patterns on channel sounding measurements. Channel parameters extracted from the channel sounding measurements, performed in Ilmenau [14], were used to analyse the performance of directional antennas in mobility scenarios. Since these simulations involved the measured channel parameters, they are referred to as *emulation*. Such a method, in addition, provides flexibility to test various antenna types using the same measurement data without conducting the real measurements every time [89].

The channel sounding measurements [14, 88] were performed with three base-stations at a height of 25 m. Dual polarised 8-element linear array was used at the base stations. A receive circular array of 12 dual polarised patches was moved

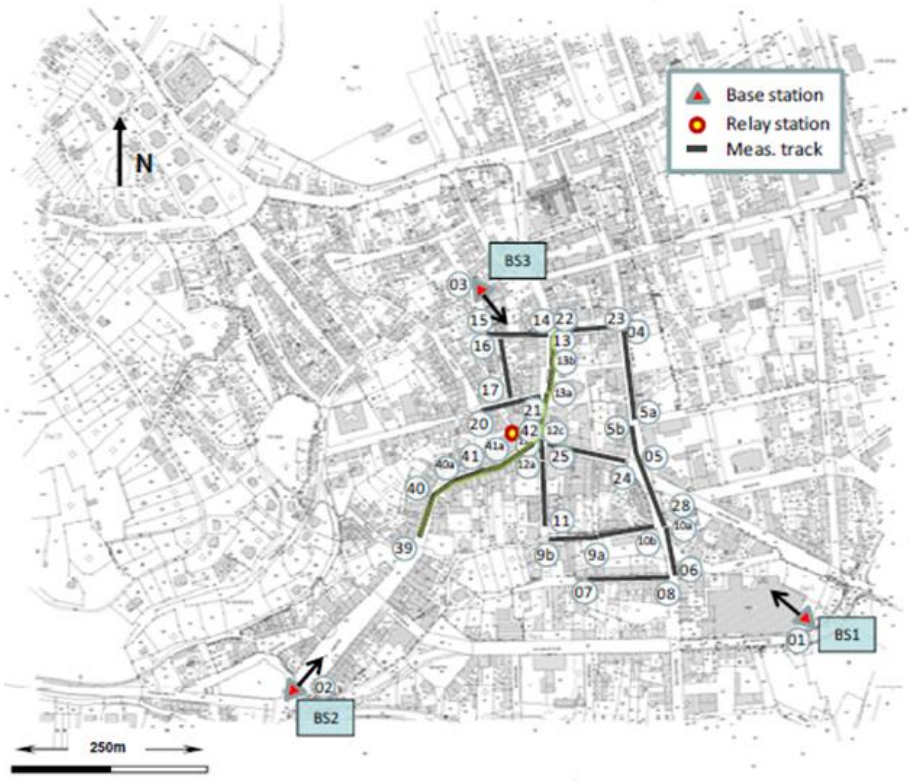

Figure 6.16: Sketch of Ilmenau Reference Scenario consisting of three base-stations (BS), and a relay node. Channel sounding measurements were performed using a receive node moved along the tracks indicated by black lines [88]. The measurements were performed with one base-station at a time. The tracks used for the evaluation of directional antennas are highlighted with green colour.

around in the city centre at a height of 2.5 m and with a speed of 3 - 5 m/s. The receive node was moved along 22 tracks. During the measurements, only one base-station was active at a time. Hence, three measurements were taken on each track. The channel parameters during the three measurements on the same track were not measured in exactly the same scenario, but this does not influence the analysis. Hence, in this analysis for directional opportunity, the channel occupancy for the CR node is compared for the three base-stations as if they were active simultaneously and occupied the same frequency band.

6.2.1 Emulation Framework

Out of the 22 tracks of the reference scenario, shown in Fig. 6.16, the directional sensing results for 8 tracks are shown in the following sub-sections. These eight tracks form two diverse tracks shown in Fig. 6.17(a) and 6.17(b). Track $39 - 42$ emulates a CR node moving towards a point where the power received from the three base-stations becomes comparable. On the other hand, track $12c - 13$ emulates a node approaching rapidly to $BS3$.

6.2.2 Directional Opportunity Analysis for the Reference Antenna System

The reference antenna system of Fig. 3.7 was embedded to the channel data for the tracks in Fig. 6.17. Three-dimensional patterns of the reference antenna system were embedded to the three-dimensional power angular profile of the tracks.

As the node moved on the track $39 - 42$, RSSI was calculated for every snapshot and for all three base-stations. From the 8 antennas on the base-stations, only one

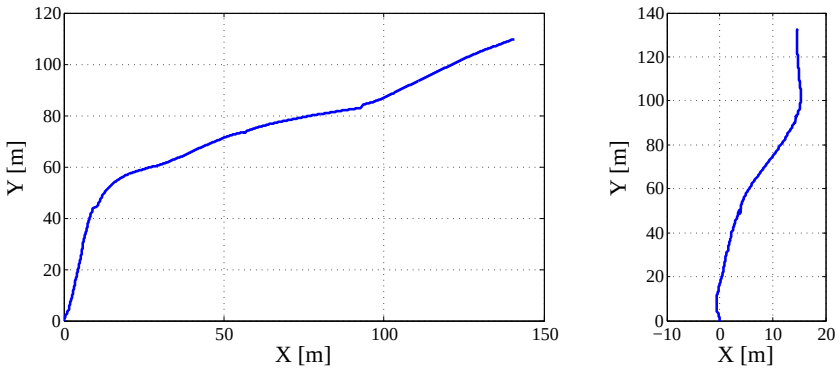

(a) Track 39 - 42 (b) Track $12c$ - 13

Figure 6.17: Mobility Scenario: Chosen tracks from the Ilmenau Reference Scenario.

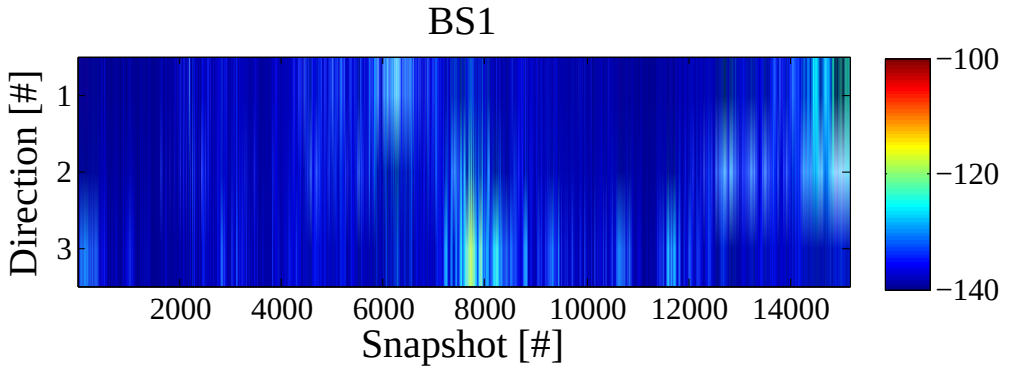

(a) RSSI - Base Station 1

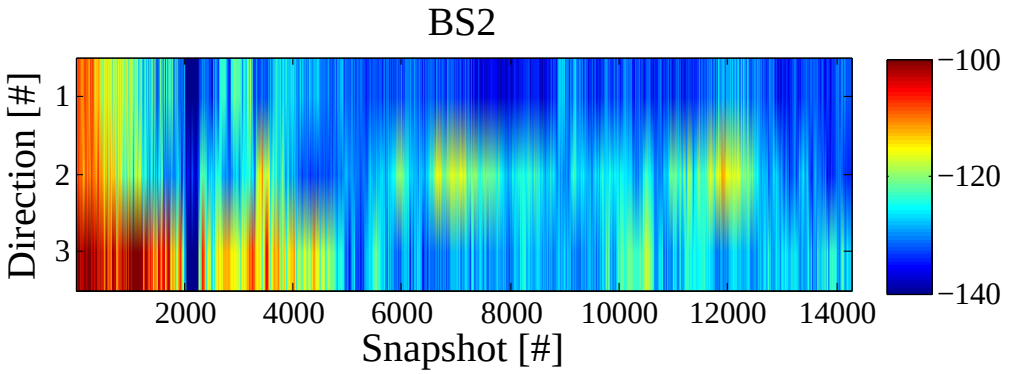

(b) RSSI - Base Station 2

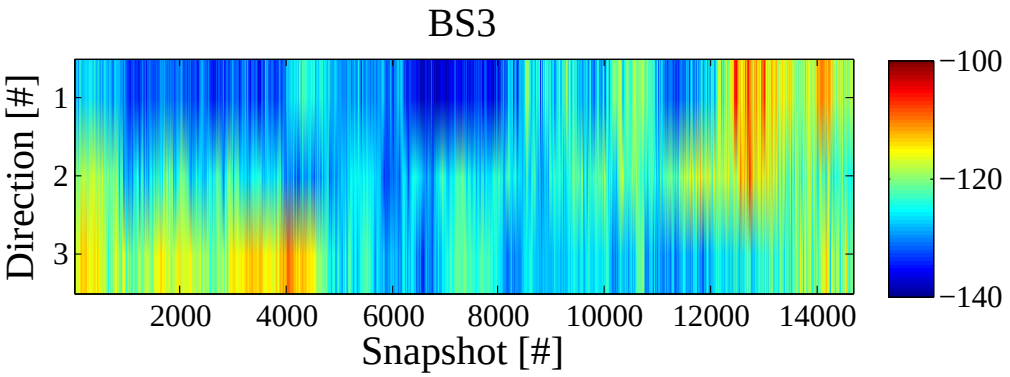

(c) RSSI - Base Station 3

Figure 6.18: Mobility track 39 - 42: RSSI for directional patterns of the reference antenna (Fig. 3.7). Colours indicate RSSI, where red indicates a high signal strength, and blue indicates a low signal strength.

transmit antenna was assumed to be active. The resultant RSSI over the track is shown in Fig. 6.18. It can be seen here that very low power, of the order of -140 dBm, was received on all three directions when $BS1$ was active. This is because $BS1$ was relatively far from the track. At the start of the track CR node was close to $BS2$, and at the end it was close to $BS3$. This effect can be seen in Fig. 6.18, where the RSSI levels from $BS2$ were higher at the start of the track. Similarly, power received from $BS3$ was higher at the end of the track $39 - 42$.

Nevertheless, on many points on the tracks, it can be observed that one direction received 20 dB or higher as compared to the other directions. This indicates an opportunity to use the directional resource for secondary transmission. The usability, however, depends on the desired transmission direction, distance from the licensed user, and secondary transmission power. Opportunity for directional communications in the mobility scenario, was calculated using fixed threshold

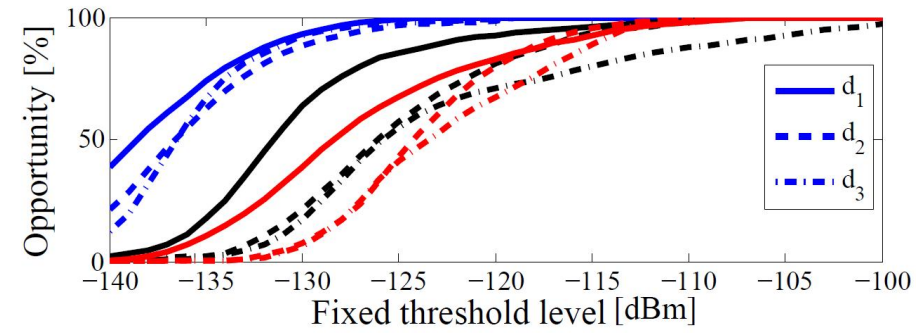

(a) Omnidirectional Opportunity

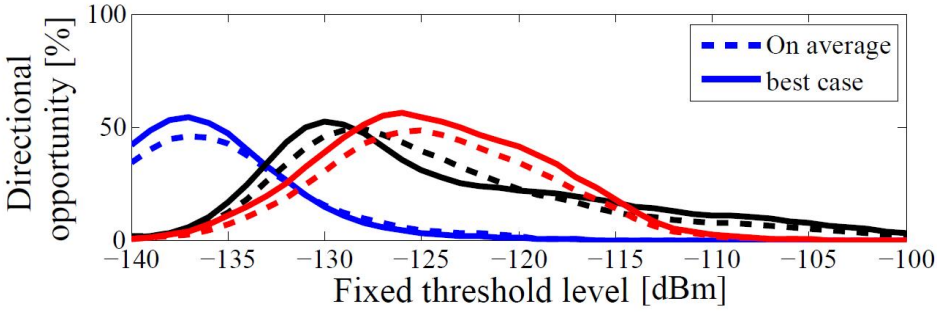

(b) Directional opportunity

Figure 6.19: Opportunity for the reference antenna (Fig. 3.7) embedded on to the scenario $39 - 42$. The opportunity for three base stations is shown with blue ($BS1$), black ($BS2$), and red ($BS3$). The opportunity observed by the three directions are represented by solid, dashed, and dash-dotted lines.

(i.e., case I). Fixed threshold was used to evaluate the emulation results, since the power levels (RSSI) received by the emulated CR node correspond to a real scenario. The opportunity, calculated individually for the three directional patterns is shown in Fig. 6.19(a). When power detection was applied to the data, opportunity was observed for the threshold values ranging from -140 to -100 dBm. These values correspond to the minimum and maximum received power levels, apparent from Fig. 6.18. When the threshold level was higher than the maximum received power, 100 % opportunity was available. And when it was lower than the minimum received power, the opportunity was 0 %. Furthermore, the opportunity available in the three directions (indicated by the line types in Fig. 6.19(a)) varied from each other. The directional opportunity for the three base stations, shown in Fig. 6.19(b) illustrate the optimum threshold level that provided maximum directional opportunities. At a threshold level of -137 dBm, 50 % of the track provides directional opportunities for $BS1$. The directional opportunity of 50 % is observed for $BS2$ and $BS3$ at a threshold level of -130 and -125 dBm, respectively. Fig. 6.19(b) shows the directional opportunity for the best case, and an average directional opportunity over all direction pairs. It can be seen that both the average and the best-case values approach almost the same level of directional resource availability.

Track $12c$ - 13 follows a completely different path profile compared to Track 39 - 42. It is a track approaching very close to $BS3$. RSSI for this track is shown in Fig. 6.20. At the start of the track, $BS2$ receives more power but as the CR node moves further, the power starts to decrease. Moreover, the power received by $BS3$ in the middle of the track is maximum because of the directional nature of the transmit antenna on the base-station.

The maximum and minimum threshold for the scenario is indicated by the ramp of omnidirectional opportunity from 0 to 100 % in Fig. 6.21(a). The directional opportunity in Fig. 6.21(b) indicates that the optimum level of the threshold in this case are -132, -130, and -122 dBm for $BS1$, $BS2$, and $BS3$ respectively.

For the two heterogeneous paths, directional opportunity of about 50 % was observed for threshold levels ranging from -135 to -120 dBm. These results can be considered representative for a suburban scenario. Hence, it can be concluded that for a suburban scenario, a well-designed 3-sector antenna can provide 50 % directional opportunity in the mobile scenario. Nevertheless, from the results of the static simulations with spatial channel model, it can be concluded that similar observations can be expected for urban scenarios.

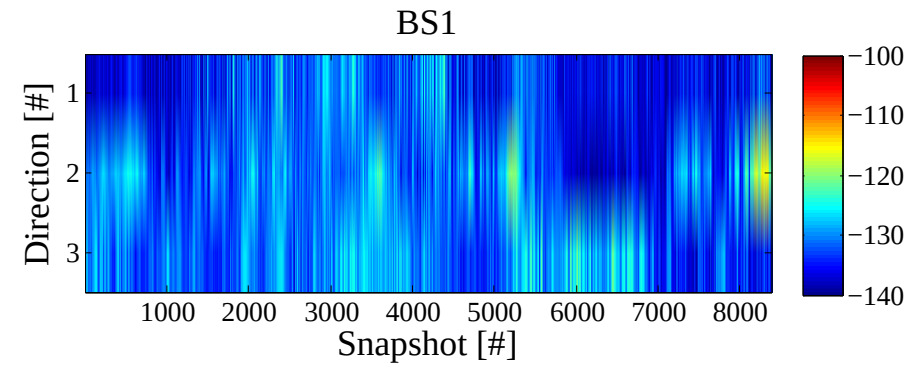

(a) RSSI - Base Station 1

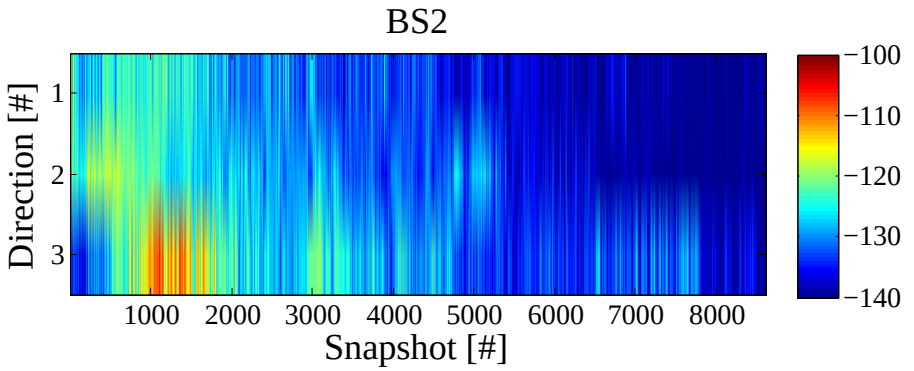

(b) RSSI - Base Station 2

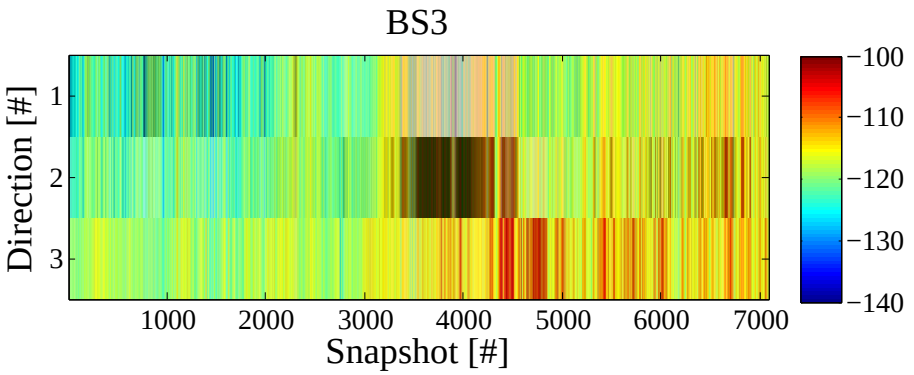

(c) RSSI - Base Station 3

Figure 6.20: Mobility track $12c$ - 13: RSSI for directional patterns of the reference antenna (Fig. 3.7). Colours indicate RSSI, where red indicates a high signal strength, and blue indicates a low signal strength.

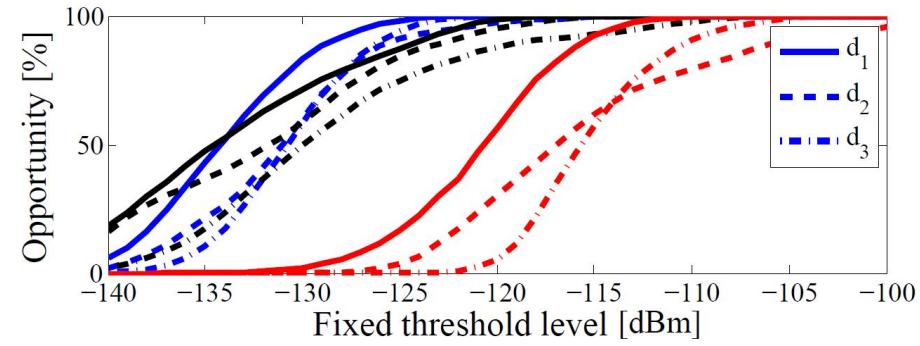

(a) Opportunity

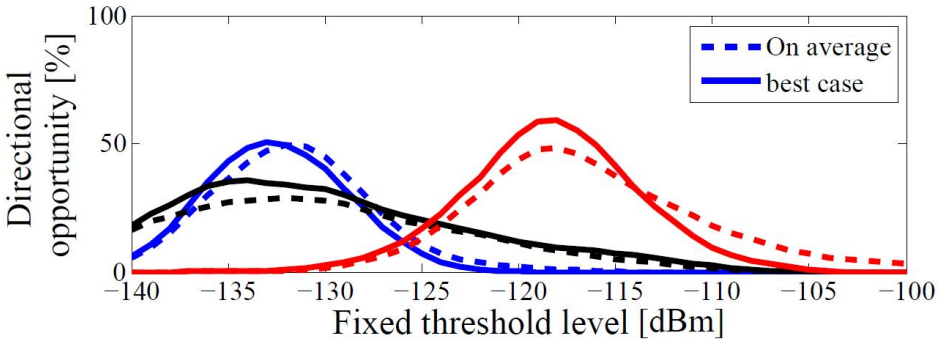

(b) Directional opportunity

Figure 6.21: Opportunity for the reference antenna (c.f. 3.7) embedded on to the scenario $12c - 13$. The opportunity for the three base stations is shown with blue ($BS1$), black ($BS2$), and red ($BS3$). The opportunity observed by the three directions is represented by solid, dashed, and dash-dotted lines.

6.2.3 Directional Opportunity Analysis for the Realised Antenna System

The measured beam patterns of the realised antenna system of Fig. 5.20 were embedded to the channel data for the track $39 - 42$ in Fig. 6.17. The resultant RSSI over the track is shown in Fig. 6.22. It can be observed that, as in the case of the reference antenna system (cf. Fig. 6.18), very low power was received on all three directions when $BS1$ was active. The opportunity available for the directional patterns of the realised antenna system is shown in Fig. 6.23(a). Although individual opportunity available in all three directions appears to be the same for all base-stations, the dissimilarity analysis helps in identifying the existence of directional opportunity. Compared to the directional opportunity for the

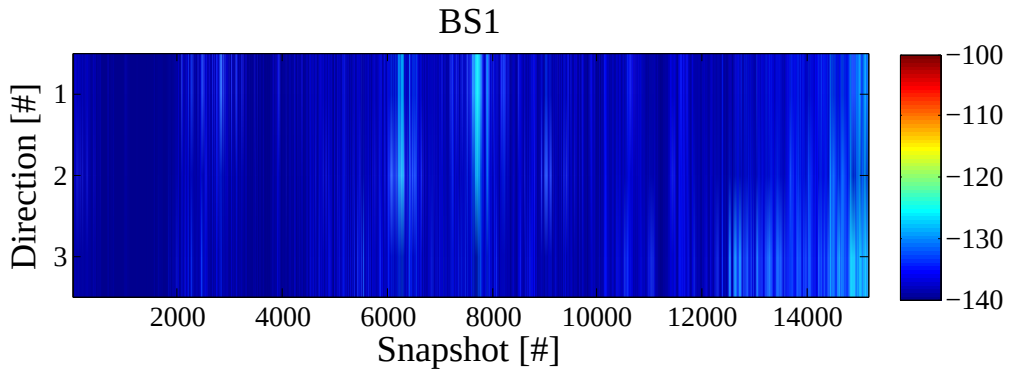

(a) RSSI - Base Station 1

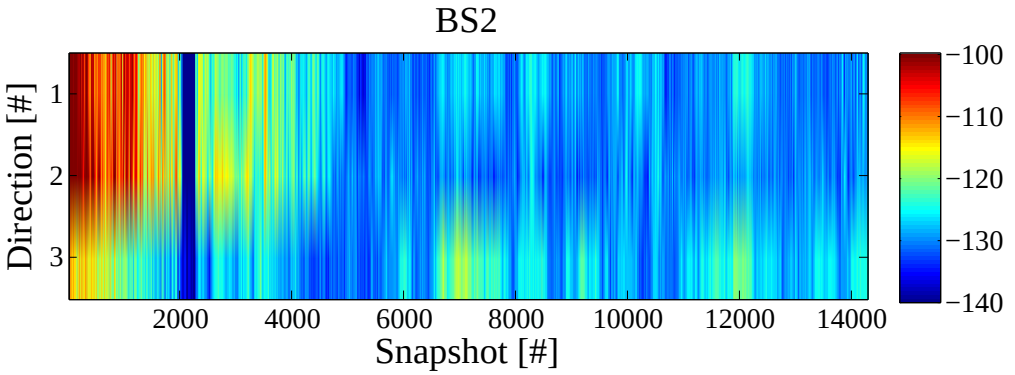

(b) RSSI - Base Station 2

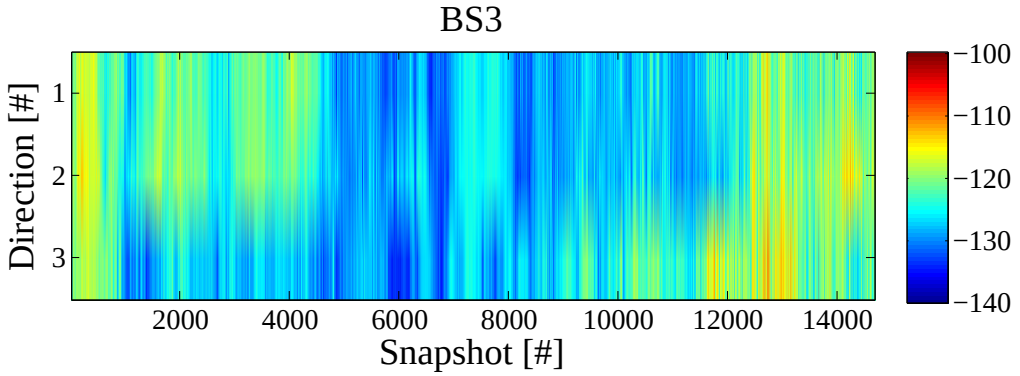

(c) RSSI - Base Station 3

Figure 6.22: Mobility track 39 - 42: RSSI for directional patterns of the measured antenna (Fig. 5.20). Colours indicate RSSI, where red indicates a high signal strength, and blue indicates a low signal strength.

reference antenna system (cf. Fig. 6.19(b)), the realised antenna system provides

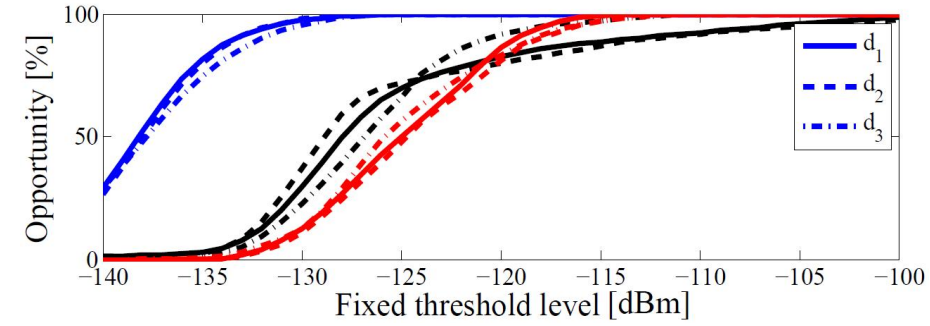

(a) Omnidirectional Opportunity

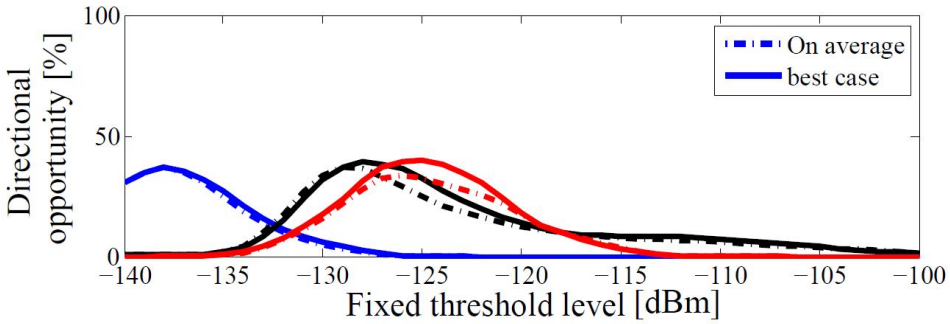

(b) Directional opportunity

Figure 6.23: Opportunity for the realised antenna system (Fig. 5.20) embedded on to the scenario $39-42$. The opportunity for three base stations is shown with blue ($BS1$), black ($BS2$), red ($BS3$). The opportunity observed by the three directions are represented by solid, dashed, and dash-dotted lines.

directional opportunity of approximately $40\ \%$ at the threshold levels comparable to that for the reference antenna.

Summary

This chapter presented analysis approaches to evaluate directional antennas for cognitive radio. A spatial channel model was used to analyse the performance of antenna arrays in heterogeneous propagation scenarios. The measured and analytical radiation patterns were embedded on to the power angular profile obtained from the channel model. These simulations were performed for various scenarios, ranging from rural to urban. The average power received by the reference antenna system was comparable for all scenarios. Directional opportunity of $50\ \%$ was obtained for the reference antenna system. The analytical patterns of uniform circular array were used to identify the nature of the radiation patterns required

for obtaining directional resources. The differences among the received signal strength among directions was found to be proportional to the side-lobe level of the directional patterns. A 6-element circular array was found to be optimum for directional resource identification. Such an array provided side-lobe level of 20 dB.

The channel model provided power angular profiles for random locations within a certain area. The resultant analysis was, therefore, attributed to belong static scenarios. In order to evaluate the performance of the measured directional patterns in mobility scenarios, channel sounder measurements were used. These measurements were performed with the help of channel sounder in the city centre of Ilmenau, Germany. The original purpose of these measurements was to extract channel parameters. Later on, methods to embed various antenna patterns on to the data from these measurement campaigns were devised. The analysis described here used the existing antenna embedding methods. The performance of the measured directional patterns of the reference, and the compact antenna system were analysed. Both these patterns provided directional communications opportunity for 50 $\%$ of the snapshots, indicating an opportunity to use this resource for cognitive radio communication on half of the track.

7. SUMMARY AND CONCLUSION

Specific approaches to design and analyse compact directional antennas for CR are explored in the thesis. Single-port multi-band and multi-port multi-band antennas were studied. Conformal and planar arrangement of these antennas provide access to spatial and frequency resources. Feed strategy for a conformal dipole arrangement was developed and a suitable feed network was fabricated.

A concentric arrangement of monopole antenna arrays was used as a reference antenna system, where directional patterns were obtained using metallic/absorber walls between antenna elements. This reference antenna system was used to perform proof-of-principle measurement campaigns. With an antenna array of nine elements, nine degrees-of-freedom (spectral-spatial resources) were obtained at the antenna ports. These consist of 3 selectable frequency bands, namely GSM 900 MHz, GSM 1800 MHz, and IEEE 802.11b/g, and 3 directions per frequency band. The reference antenna system was capable of separating frequency and directions with a signal-to-interference-ratio of 20 dB, inside an anechoic chamber. An outdoor measurement of such an antenna system was carried out for GSM 1800 MHz, at a location surrounded by four base-stations. Power detection was used as the spectrum sensing algorithm. Directional opportunity was observed for about 50 % of the sensing time for various GSM channels.

This concentric array arrangement was made compact by reducing the inter-element spacing. The reduction in inter-element spacing results in mutual coupling between antenna elements, which disturbs the current distribution and hence the beam patterns of the antenna arrays. To reduce this negative effect, a multi-band decoupling and matching network was designed to mitigate the element coupling and match the elements with mode-specific loads. Reconfigurability at each frequency band was achieved by capacitive tuning with a varactor diode. The multi-band decoupling and matching network, and the reconfigurable network for GSM 900 MHz were manufactured on a printed circuit board. These feed networks were tested in terms of decoupling, matching, and resulting port beam patterns. The 10 dB bandwidth for matching and decoupling by the fixed network, for compact antenna arrangement with an inter-element spacing of $\lambda/6$, was about 30 MHz. Reconfigurable network provided a bandwidth above 100 MHz, achievable with five reconfigurable states. The patterns were orthogonal in

different directions with correlation coefficients less than 30 % and self-similar at different frequency bands with a correlation better than 70 %. The directivity varied between 4 and 6 dBi for the three modes.

The design of a fractal antenna structure, known as Sierpinski gasket antenna, was undertaken as a multi-band antenna. Because of the log-periodic structure of this antenna, it provided self-similar radiation properties at the design frequency bands even after folding. The limitation of Sierpinski gasket, however, is that it can resonate only on multiples of the principle frequency band. Furthermore, all frequency degrees-of-freedom are accessible at a single port, and the spectral filtering among designed frequencies is not well-defined. Due to these limitations, multi-port multi-band inverted-F antenna was designed. This antenna provided access to frequency degrees-of-freedom at separate ports. Planar arrangement of these multi-band antennas can provide access to the directional resources at the design frequency bands. Feed networks for a conformal arrangement of dipole antennas was designed to provide isotropic spatial coverage.

The behaviour of directional antennas under heterogeneous propagation scenarios was studied using simulation and emulation. Simulations were performed with analytical patterns of uniform circular arrays and spatial channel models. These simulations helped in identification of the influence of side-lobe level and number of array elements on the availability of directional resources. The simulation results indicated that the side-lobe level of the antenna, dictated by the number and geometrical arrangement of elements in the array, affect the performance of directional sensing. Side- and back-lobes in the antenna radiation pattern should be minimised to increase the directional opportunity. Similar observations were made for all observed scenarios. A side-lobe level of 20 dB is suggested for antenna design for directional cognitive radio communications. Optimum directional opportunity was achieved at six elements for all heterogeneous propagation scenarios. The 6-element circular array of monopoles provides up to 60 % directional opportunity for heterogeneous propagation scenarios, at a threshold level of 20 dB. A further increase in number of elements does not provide considerably more directional opportunity. However, 6-element array turns out to be large for small platforms. Even if compact antenna arrays are considered, the design of feed network for such an array becomes complex. However, depending on the application scenario for cognitive radio, such an array may be considered.

The directional patterns of realised antenna systems were embedded on to the channel parameters from channel sounder measurements, to emulate mobility scenarios. Various tracks were chosen from this measurement campaign for the analysis of the designed antennas. Directional opportunity of about 50 % was obtained for a threshold level lower than -120 dBm for mobility scenarios. The results are representative of a suburban scenario. Nevertheless, combining the res-

ults of this emulation with the static simulations of spatial channel model, similar observations are expected for urban scenarios.

The thesis proposes approaches to design and evaluate directional antennas for cognitive radio. The focus was laid on the existence of directional resources for cognitive radio, design of multi-band directional antennas, and performance evaluation of the proposed antennas for directional sensing. It is concluded that well-designed directional antennas can identify the existence of directional resources for cognitive radio communications. Multi-port multi-band directional antennas can provide separate access to frequency and directional resources. Such antennas can filter frequency and directional resources at the antenna ports, and allow simultaneous sensing and communications. To assist the work of the proposed antenna system, each degree-of-freedom can be dealt with separately using the existing spectrum sensing algorithms, and the proposed directional opportunity analysis can be applied. Conventional spectrum sensing algorithms may also be extended to sophisticated directional spectrum sensing algorithms to deal with frequency and directional resources simultaneously.

Decoupling and matching networks for compact arrays can be fabricated with off-the-shelf lumped elements with tight tolerances. Reconfigurable decoupling and matching networks can be realised using varactor diodes. Such networks can reconfigure to widely separated frequency bands or within a specific frequency band. The number of the required reconfigurable elements depends on the size of the array, degree of compactness, and reconfigurability range.

Directional communications opportunity is available for static and mobile scenarios. A variety of multipath scenarios, ranging from rural to highly urban, hold directional opportunity for cognitive radio. The opportunity available for directional communications depends on the sensing threshold. Nevertheless, the difference in the received signal strength of an antenna array with three elements (three directions) is as high as 15 dB. Arrays with higher number of elements can ensure more opportunity for a lower threshold level, where an array with 6 elements is found to be optimum.

Secondary transmission using directional antennas is out of scope of this work. However, it is envisaged that a transmission opportunity depends on the location of secondary transmitter and secondary receiver, distance from the primary user, and power handling of the secondary system. The work presented in the thesis is expected to facilitate the design of future directional antennas for cognitive radios resulting in more efficient utilisation of the spectrum. It is expected to trigger more research into exploring the directional aspects in cognitive radio, especially antenna design for cognitive radio.

LIST OF ABBREVIATIONS/SYMBOLS

α	Sierpinski gasket flare angle
ϵ_r	Relative permittivity
η_{rad}	Radiation efficiency
Γ	Reflection coefficient
γ	Sensing threshold
λ_g	Guided wavelength
λ_n	n^{th}Eigen-value
ϕ	Azimuth angle
$\Re\{\cdot\}$	Real value
ρ	Correlation coefficient
σ_w	Noise variance
σ_x	Signal variance
σ_y	Signal variance
θ	Elevation angle
$\tilde{B_a}$	Antenna Susceptance matrix
$\tilde{G_a}$	Antenna conductance matrix
$\tilde{S_a}$	Antenna S-matrix
$\tilde{S_s}$	System S-matrix
$\tilde{T_a}$	Current transfer matrix

$\tilde{T_u}$ Voltage transfer matrix

$\tilde{Y_a}$ Antenna admittance matrix

$\tilde{Y_n}$ Network admittance matrix

$\tilde{Y_s}$ System admittance matrix

$\tilde{Z_a}$ Antenna Impedance matrix

$\tilde{Z_s}$ System Impedance matrix

$\vec{a}$ Incident power wave

$\vec{b}$ Incident power wave

$\vec{f}(\Theta, \phi)$ Far-field pattern

c Speed of light

d_k Direction k

$E(y)$ Received signal energy

f_r Resonance frequency

$f_{m,n,l}$ Resonance frequency of mode mnl of triangular patch

h Substrate height

i Current

N Number of samples

P_d Probability of detection

P_f Probability of false alarm

P_{acc} Accepted power

P_{in} Incident power

P_{rad} Radiated power

R_{rad} Radiation resistance

S_{nm} Transmission coefficient between port n and port m

S_{nn} Reflection coefficient at port n

SNR_{wall} Lowest SNR required for energy detection

u Voltage

$w[n]$ Noise samples

$x[n]$ Transmitted signal samples

$y[n]$ Received signal samples

Z_0 Characteristic impedance

Z_L Load impedance

$\{\cdot\}^H$ Hermitian transpose

AUT Antenna under test

Balun Balanced-unbalanced transformer

CPWG Coplanar waveguide with ground

CR Cognitive radio

DC Direct current

DMN Decoupling and matching network

DUT Device under test

FFT Fast Fourier transform

IC Integrated circuit

IFA Inverted-F antenna

LOS Line-of-sight

MMCX Micro-miniature coaxial

NLOS Non-line-of-sight

OTA Over-the-air

PA Power amplifier

PAP Power angular profile

PSD power spectral density

PU Primary user

RF Radio frequency

RSSI Received signal strength indicator

SCM Spatial channel model

SCME Spatial channel model extended

SINR Signal-to-interference-and-noise-ratio

SIR Signal-to-interference-ratio

SMD surface mounted device

SNR Signal-to-noise-ratio

SP3T Single-pole-triple-throw switch

SU Secondary user

BIBLIOGRAPHY

Books

[1] Linda E. Doyle. *Essentials of Cognitive Radio*. Cambridge University Press, 2009.

[2] Frank H. P. Fitzek and Marcos D. Katz. *Cognitive Wireless Networks*. Springer, 2007.

[3] C. A. Balanis. *Antenna Theory: Analysis and Design*. John Wiley & Sons, Inc., New York, second edition, 1997.

[4] John L. Volakis. *Antenna Engineering Handbook*. Mc Graw Hill, third edition, 2007.

[5] Randy L. Haupt. *Antenna Arrays: A Computational Approach*. John Wiley & Sons, Inc., third edition, 2010.

[6] T. S. Rappaport. *Wireless Communications Principles and Practice*. Pearson Education, second edition, 2002.

[7] Zhijun Zhang. *Wireless Communications Principles and Practice*. John Wiley &Sons (Asia) Pte Ltd, 2011.

[8] I. J. Bahl and P. Bhartia. *Microstrip Antennas*. Artech House, 1980.

Theses

[9] J. Mitola III. *Cognitive radio*. PhD thesis, KTH Royal Institute of Technolgy, Sweden, 1999.

[10] J. Weber. *Entwurf miniaturisierter Antennengruppen*. PhD thesis, Technische Universität Ilmenau, Germany, 2009.

[11] C. Volmer. *Compact antenna arrays in mobile communications : A quantitative analysis of radiator coupling*. PhD thesis, Technische Universität Ilmenau, Germany, 2010.

[12] Bilal H. Qureshi. Directional spectrum sensing and transmission using a sector antenna. Master's thesis, Mid Sweden University, 2011.

[13] A. Muhammad Shahbaz. Capacitive tuning to increase the operational bandwidth of a decoupling and matching network for a compact array. Master's thesis, Technische Universität Ilmenau, Germany, 2013.

[14] A. Richter. *On the Estimation of Radio Channel Parameters: Models and Algorithms (RIMAX)*. PhD thesis, Technische Universität Ilmenau, Germany, May 2005.

Articles

[15] J. Mitola III and G.Q. Maguire Jr. Cognitive radio: making software radios more personal. *Personal Communications, IEEE*, 6(4):13–18, 1999.

[16] S. Haykin. Cognitive radio: brain-empowered wireless communications. *Selected Areas in Communications, IEEE Journal on*, 23(2):201–220, 2005.

[17] H. Celebi, I. Guvenc, S. Gezici, and H. Arslan. Cognitive-radio systems for spectrum, location, and environmental awareness. *Antennas and Propagation Magazine, IEEE*, 52(4):41–61, 2010.

[18] G. Zhao, J. Ma, G.Y. Li, T. Wu, Y. Kwon, A. Soong, and C. Yang. Spatial spectrum holes for cognitive radio with relay-assisted directional transmission. *Wireless Communications, IEEE Transactions on*, 8(10):5270–5279, 2009.

[19] T. Yucek and H. Arslan. A survey of spectrum sensing algorithms for cognitive radio applications. *Communications Surveys Tutorials, IEEE*, 11(1):116–130, 2009.

[20] F. Ghanem, P.S. Hall, and J.R. Kelly. Two port frequency reconfigurable antenna for cognitive radios. *Electronics Letters*, 45(11):534–536, 2009.

[21] M.R. Hamid, P. Gardner, P.S. Hall, and F. Ghanem. Switched-band vivaldi antenna. *Antennas and Propagation, IEEE Transactions on*, 59(5):1472–1480, 2011.

[22] J.H. Reed, J.T. Bernhard, and Jung-Min Park. Spectrum access technologies: The past, the present, and the future. *Proceedings of the IEEE*, 100(Special Centennial Issue):1676–1684, 2012.

[23] Guodong Zhao, Jun Ma, G.Y. Li, Tao Wu, Young Kwon, A. Soong, and Chenyang Yang. Spatial spectrum holes for cognitive radio with relay-assisted directional transmission. *Wireless Communications, IEEE Transactions on*, 8(10):5270–5279, 2009.

[24] J.L. Freeman, B.J. Lamberty, and G.S. Andrews. Optoelectronically reconfigurable monopole antenna. *Electronics Letters*, 28(16):1502–1503, 1992.

[25] C. Volmer, J. Weber, R. Stephan, K. Blau, and M.A. Hein. An eigen-analysis of compact antenna arrays and its application to port decoupling. *Antennas and Propagation, IEEE Transactions on*, 56(2):360–370, 2008.

[26] Seymour Stein. On cross coupling in multiple-beam antennas. *Antennas and Propagation, IRE Transactions on*, 10(5):548–557, 1962.

[27] N. Amitay. Improvement of planar array match by compensation through contiguous element coupling. *Antennas and Propagation, IEEE Transactions on*, 14(5):580–586, 1966.

[28] J. Andersen and H. Rasmussen. Decoupling and descattering networks for antennas. *Antennas and Propagation, IEEE Transactions on*, 24(6):841–846, 1976.

[29] H. J. Chaloupka, X. Wang, and J. C. Coetzee. A superdirective 3-element array for adaptive beamforming. *Microw. Opt. Technol. Lett.*, 36(6):425–430, 2003.

[30] J. Weber, C. Volmer, K. Blau, R. Stephan, and M.A. Hein. Miniaturized antenna arrays using decoupling networks with realistic elements. *Microwave Theory and Techniques, IEEE Transactions on*, 54(6):2733–2740, 2006.

[31] D. Tandur, J. Duplicy, K. Arshad, D. Depierre, K. Moessner, J. Lehtomaki, K. Briggs, L. Goncalves, and A. Gameiro. Cognitive radio systems evaluation: Measurement, modeling, and emulation approach. *Vehicular Technology Magazine, IEEE*, 7(2):77–84, 2012.

[32] R.V. Hara Prasad, Y. Purushottam, V.C. Misra, and N. Ashok. Microstrip fractal patch antenna for multiband communication. *Electronics Letters*, 36(14):1179 –1180, jul 2000.

[33] C. Puente-Baliarda, J. Romeu, R. Pous, and A. Cardama. On the behavior of the sierpinski multiband fractal antenna. *Antennas and Propagation, IEEE Transactions on*, 46(4):517 –524, apr 1998.

[34] C. Puente, J. Romeu, R. Bartoleme, and R. Pous. Perturbation of the sierpinski antenna to allocate operating bands. *Electronics Letters*, 32(24):2186 –2188, nov 1996.

[35] Jr. Compton, R. The tripole antenna: An adaptive array with full polarization flexibility. *Antennas and Propagation, IEEE Transactions on*, 29(6):944–952, 1981.

[36] J. Helszajn and D.S. James. Planar triangular resonators with magnetic walls. *Microwave Theory and Techniques, IEEE Transactions on*, 26(2):95–100, 1978.

[37] Jong-Hyuk Lim, Gyu-Tae Back, Young-Il Ko, Chang-Wook Song, and Tae-Yeoul Yun. A reconfigurable pifa using a switchable pin-diode and a fine-tuning varactor for uspcs/wcdma/m-wimax/wlan. *Antennas and Propagation, IEEE Transactions on*, 58(7):2404–2411, 2010.

[38] Y. Tawk, J. Costantine, and C. G. Christodoulou. A varactor-based reconfigurable filtenna. *Antennas and Wireless Propagation Letters, IEEE*, 11:716–719, 2012.

[39] Yi-Ming Chen, Sheng-Fuh Chang, Cheng-Yu Chou, and Kun-Hsing Liu. A reconfigurable bandpass-bandstop filter based on varactor-loaded closed-ring resonators [technical committee]. *Microwave Magazine, IEEE*, 10(1):138–140, 2009.

[40] Hiroki Tanaka and T. Ohira. Beam-steerable planar array antennas using varactor diodes for 60-ghz-band applications. In *Microwave Conference, 2003. 33rd European*, pages 1067–1070, 2003.

[41] R.B. Ertel, P. Cardieri, K.W. Sowerby, T.S. Rappaport, and J.H. Reed. Overview of spatial channel models for antenna array communication systems. *Personal Communications, IEEE*, 5(1):10–22, 1998.

[42] A. R. Sebak M. Alsehaili, S. Noghanian and D. A. Buchanan. Angle and time of arrival statistics of a three dimensional geometrical scattering channel model for indoor and outdoor propagation environments. *Progress In Electromagnetics Research*, 109(doi:10.2528/PIER10081106):191–209, 2010.

Own Publications

[43] N. Murtaza and M.A. Hein. Folded sierpinski monopole antenna with self-similar radiation properties. In *Wireless Technology Conference (EuWIT), 2010 European*, pages 189–192, 2010.

[44] N. Murtaza, M.A. Hein, and E. Zameshaeva. Reconfigurable decoupling and matching network for a cognitive antenna. In *Microwave Conference (EuMC), 2011 41st European*, pages 874–877, 2011.

[45] N. Murtaza, A. Krah, M. Grimm, A. Heuberger, R. Thoma, and M. Hein. Multi-band direction-sensitive cognitive radio node. In *Antennas and Propagation in Wireless Communications (APWC), 2011 IEEE-APS Topical Conference on*, pages 251–254. IEEE, 2011.

[46] A. Krah, M. Grimm, N. Murtaza, W. Kotterman, M. Landmann, A. Heuberger, R. Thoma, and M. Hein. Over-the-air test strategy and testbed for cognitive radio nodes. In *General Assembly and Scientific Symposium, 2011 XXXth URSI*, pages 1–4, 2011.

[47] N. Murtaza M. Grimm A. Krah M.A. Hein A. Heuberger R.S. Thoma B.H. Qureshi, R.K. Sharma. Exploiting spatial dimension in spectrum sensing using a sector antenna: A ray tracer based analysis. In *IEEE 77th Vehicular Technology Conference*. IEEE, 2013.

[48] R.S. Thoma M.A. Hein N. Murtaza, R.K. Sharma. Directional antennas for cognitive radio: Analysis and design recommendations. *Progress In Electromagnetics Research*, 140:1–30, 2013.

[49] S. Irteza, N. Murtaza, S. Caizzone, R. Stephan, and M.A. Hein. Compact planar l-band antenna arrays with optimal diversity performance. In *Antennas and Propagation in Wireless Communications (APWC), 2011 IEEE-APS Topical Conference on*, pages 512–515, 2011.

Miscellaneous

[50] Spectrum policy task force report (et docket no. 02-135). Technical report, Federal Communications Commission, 2002.

[51] M. Wellens, J. Wu, and P. Mahonen. Evaluation of spectrum occupancy in indoor and outdoor scenario in the context of cognitive radio. In *Cognitive Radio Oriented Wireless Networks and Communications, 2007. CrownCom 2007. 2nd International Conference on*, pages 420–427. IEEE, 2007.

[52] K. Nishimori, R. Di Taranto, H. Yomo, P. Popovski, Y. Takatori, R. Prasad, and S. Kubota. Spatial opportunity for cognitive radio systems with heterogeneous path loss conditions. In *Vehicular Technology Conference, 2007. VTC2007-Spring. IEEE 65th*, pages 2631–2635. IEEE, 2007.

[53] R. Di Taranto, K. Nishimori, P. Popovski, H. Yomo, Y. Takatori, R. Prasad, and S. Kubota. Simple antenna pattern switching and interference-induced multi-hop transmissions for cognitive radio networks. In *New Frontiers in Dynamic Spectrum Access Networks, 2007. DySPAN 2007. 2nd IEEE International Symposium on*, pages 543–546. IEEE, 2007.

[54] M. Barrie, S. Delaere, G. Sukareviciene, J. Gesquiere, and I. Moerman. Geolocation database beyond tv white spaces: Matching applications with database requirements. In *Dynamic Spectrum Access Networks (DYSPAN), 2012 IEEE International Symposium on*, pages 467–478, 2012.

[55] Ha Nguyen Tran, Y.D. Alemseged, Chen Sun, and H. Harada. On the effect of local sensing database to cognitive radio systems. In *Wireless Personal Multimedia Communications (WPMC), 2011 14th International Symposium on*, pages 1–5, 2011.

[56] Zhi Yan, Zhangchao Ma, Hanwen Cao, Gang Li, and Wenbo Wang. Spectrum sensing, access and coexistence testbed for cognitive radio using usrp. In *Circuits and Systems for Communications, 2008. ICCSC 2008. 4th IEEE International Conference on*, pages 270–274, 2008.

[57] Qiwei Zhang, A. B J Kokkeler, and G. J M Smit. An efficient multi-resolution spectrum sensing method for cognitive radio. In *Communications and Networking in China, 2008. ChinaCom 2008. Third International Conference on*, pages 1226–1229, 2008.

[58] R. Tandra and A. Sahai. Fundamental limits on detection in low snr under noise uncertainty. In *Wireless Networks, Communications and Mobile Computing, 2005 International Conference on*, volume 1, pages 464–469 vol.1, 2005.

[59] C.T.P. Song, P.S. Hall, H. Ghafouri-Shiraz, and I. Henning. Fractal antenna research at university of birmingham. In *Antennas and Propagation, 2001. Eleventh International Conference on (IEE Conf. Publ. No. 480)*, volume 2, pages 724 –727 vol.2, 2001.

[60] M. Al-Husseini, A. El-Hajj, Y. Tawk, K.Y. Kabalan, and C.G. Christodoulou. A simple dual-port antenna system for cognitive radio applications. In *High Performance Computing and Simulation (HPCS), 2010 International Conference on*, pages 549–552, 2010.

[61] Y. Tawk, J. Costantine, and C.G. Christodoulou. A rotatable reconfigurable antenna for cognitive radio applications. In *Radio and Wireless Symposium (RWS), 2011 IEEE*, pages 158–161, 2011.

[62] M. E. Zamudio, Y. Tawk, J. Costantine, S.E. Barbin, and C.G. Christodoulou. Reconfigurable filter embedded into an antenna for uwb cognitive radio environment. In *Antennas and Propagation in Wireless Communications (APWC), 2011 IEEE-APS Topical Conference on*, pages 714–717, 2011.

[63] K. Nishimori, R. Di Taranto, H. Yomo, P. Popovski, Y. Takatori, R. Prasad, and S. Kubota. Spatial opportunity for cognitive radio systems with heterogeneous path loss conditions. In *Vehicular Technology Conference, 2007. VTC2007-Spring. IEEE 65th*, pages 2631–2635, 2007.

[64] R. Di Taranto, K. Nishimori, P. Popovski, H. Yomo, Y. Takatori, R. Prasad, and S. Kubota. Simple antenna pattern switching and interference-induced multi-hop transmissions for cognitive radio networks. In *New Frontiers in Dynamic Spectrum Access Networks, 2007. DySPAN 2007. 2nd IEEE International Symposium on*, pages 543–546, 2007.

[65] A. Mirkamali and P.S. Hall. Log periodic printed dipole array for wideband frequency reconfiguration. In *Wideband, Multiband Antennas and Arrays for Defence or Civil Applications, 2008 Institution of Engineering and Technology Seminar on*, pages 95–110, 2008.

[66] S. Nikolaou, R. Bairavasubramanian, Cesar Lugo, I. Carrasquillo, D. Thompson, G.E. Ponchak, J. Papapolymerou, and M.M. Tentzeris. Pat-

tern and frequency reconfigurable annular slot antenna using pin diodes. *Antennas and Propagation, IEEE Transactions on*, 54(2):439–448, 2006.

[67] H.J. Chaloupka and X. Wang. Novel approach for diversity and mimo antennas at small mobile platforms. In *Personal, Indoor and Mobile Radio Communications, 2004. PIMRC 2004. 15th IEEE International Symposium on*, volume 1, pages 637–642 Vol.1, 2004.

[68] P. Kyösti, J. Meinilä, L. Hentilä, X. Zhao, T. Jämsä, C. Schneider, M. Narandzic, M. Milojevic, A. Hong, and V. Holappa J. Ylitalo, M. Alatossava, R. Bultitude, Y. de Jong, and T. Rautiainen. Ist-4-027756 winner ii deliverable 1.1.2. v.1.2 winner ii channel models. Technical report, IST-WINNER2, 2007.

[69] Winner II Spatial Channel Model. *http://www.ist-winner.org/phase-2-model.html*. 2010.

[70] M. LoÌĄpez-Benitez, F. Casadevall, and C. Martella. Performance of spectrum sensing for cognitive radio based on field measurements of various radio technologies. In *Wireless Conference (EW), 2010 European*, pages 969–977, 2010.

[71] K. Patil, R. Prasad, and K. Skouby. A survey of worldwide spectrum occupancy measurement campaigns for cognitive radio. In *Devices and Communications (ICDeCom), 2011 International Conference on*, pages 1–5, 2011.

[72] W. A T Kotterman, M. Landmann, A. Heuberger, and R.S. Thoma. New laboratory for over-the-air testing and wave field synthesis. In *General Assembly and Scientific Symposium, 2011 XXXth URSI*, pages 1–4, 2011.

[73] D.H. Werner and S. Ganguly. An overview of fractal antenna engineering research. *Antennas and Propagation Magazine, IEEE*, 45(1):38–57, 2003.

[74] J.P. Gianvittorio and Y. Rahmat-Samii. Fractal element antennas: a compilation of configurations with novel characteristics. In *Antennas and Propagation Society International Symposium, 2000. IEEE*, volume 3, pages 1688 –1691 vol.3, 2000.

[75] C.T.P. Song, P.S. Hall, H. Ghafouri-Shiraz, and I. Henning. Shorted fractal sierpinski monopole antenna. In *Antennas and Propagation Society International Symposium, 2001. IEEE*, volume 3, pages 138 –141 vol.3, 2001.

[76] W.J. Krzysztofik. Fractal antenna for wlan/bluetooth multiple-bands applications. In *Antennas and Propagation, 2009. EuCAP 2009. 3rd European Conference on*, pages 2407 –2410, march 2009.

[77] P. Salonen, L. Sydanheimo, M. Keskilammi, and M. Kivikoski. A small planar inverted-f antenna for wearable applications. In *Wearable Computers, 1999. Digest of Papers. The Third International Symposium on*, pages 95–100, 1999.

[78] D. Psychogiou and J. Hesselbarth. Diversity antennas for isotropic coverage. In *Wireless Technology Conference (EuWIT), 2010 European*, pages 101–104, 2010.

[79] Yong Cai and Y.J. Guo. A reconfigurable decoupling and matching network for a frequency agile compact array. In *Antennas and Propagation (EUCAP), Proceedings of the 5th European Conference on*, pages 896–899, 2011.

[80] Yong Cai and Y.J. Guo. A frequency-agile compact array with a reconfigurable decoupling and matching network. *Antennas and Wireless Propagation Letters, IEEE*, 10:1031–1034, 2011.

[81] 3GPP TR 25.996 V6.1.0. Spatial channel model for mimo simulations. Technical report, 2003.

[82] D.S. Baum, J. Hansen, and J. Salo. An interim channel model for beyond-3g systems: extending the 3gpp spatial channel model (scm). In *Vehicular Technology Conference, 2005. VTC 2005-Spring. 2005 IEEE 61st*, volume 5, pages 3132–3136 Vol. 5, 2005.

[83] International Telecommunication Union. Guidelines for evaluation of radio transmission technologies for imt- 2000. Technical report, International Telecommunication Union, 1997.

[84] Winner + Spatial Channel Model. *http://projects.celtic-initiative.org/winner+/.*

[85] Zhong Zhimeng, Yin Xuefeng, Li Xin, and Li Xue. Extension of itu imt-advanced channel models for elevation domains and line-of-sight scenario, Jan. 2013.

[86] L. Vuokko, V. M Kolmonen, J. Salo, and P. Vainikainen. Measurement of large-scale cluster power characteristics for geometric channel models. *Antennas and Propagation, IEEE Transactions on*, 55(11):3361–3365, 2007.

[87] N. Czink, E. Bonek, L. Hentila, J. P Nuutinen, and J. Ylitalo. A measurement-based random-cluster mimo channel model. In *Antennas and Propagation Society International Symposium, 2007 IEEE*, pages 5363–5366, 2007.

[88] C. Schneider, G. Sommerkorn, M. Narand, M. Kaske, V. Algeier A. Hong, W.A.Th. Kotterman, R.S. Thoma, and C. Jandura. Multi-user mimo channel reference data for channel modelling and system evaluation from measurements. In *International ITG Workshop on Smart Antennas*. WSA, 2009.

[89] M. Kaske, C. Schneider, W. Kotterman, and R. Thoma. Solving the problem of choosing the right mimo measurement antenna: Embedding/de-embedding. In *Antennas and Propagation (EUCAP), Proceedings of the 5th European Conference on*, pages 2551–2555, 2011.

[90] M. Kaske, C. Schneider, R. Thoma, and J. Pamp. Application of the channel synthesis approach to evaluate the performance of an experimental 4-port application antenna. In *Antennas and Propagation (EUCAP), 2012 6th European Conference on*, pages 11–15, 2012.

[91] R.S. Thomaa, M. Landmann, G. Sommerkorn, and A. Richter. Multidimensional high-resolution channel sounding in mobile radio. In *Instrumentation and Measurement Technology Conference, 2004. IMTC 04. Proceedings of the 21st IEEE*, volume 1, pages 257–262 Vol.1, 2004.

[92] F. Belfiori, S. Monni, W. Van Rossum, and P. Hoogeboom. Side-lobe suppression techniques for a uniform circular array. In *Radar Conference (EuRAD), 2010 European*, pages 113–116, 2010.